# 逆デルタ噴射率がディーゼル火炎及び燃焼に与える影響に関する研究

明治大学大学院理工学研究科

2019年度

博士学位請求論文

# A Study on Effects of Inversed-delta Injection Rate Shaping on Diesel Spray Flame and Combustion

（逆デルタ噴射率がディーゼル火炎及び燃焼に与える影響に関する研究）

学位請求者　機械工学専攻

MOHD FAREEZ EDZUAN BIN ABDULLAH

# ACKNOWLEDGEMENTS

Alhamdulillah. Lucky that I did not know that the Doctoral Degree is not just an extension of the Master Degree. It takes me a couple of year to realize that, it is much more than just conducting experiments, collecting data, writing journal articles, delivering presentation at conferences and summarizing the works in a dissertation. In reality, it requires pure hard work, laser sharp focus, shear perseverance, tough yet flexible mindset to skip through failures, rejections and critics, on top of ever-growing self-doubt. Honestly, it will be impossible to complete this dissertation without support pouring from every corner and for that, I would like to dedicate this section to express my deep gratitude.

To my advisor Dr Aizawa Tetsuya, I am really proud of the fact that you have been accepting and educating me as your student for a total of seven years. Despite of heavy research and teaching loads while maintaining your hectic work-life balance, you always prioritize your students' needs, no matter how small and trivial it seems. Thank you very much, you will always be my role model, mentor and sensei.

To my amazing wife Noor Aliah, thank you for bringing the joy in every imaginable way and supporting our family for a decade, you are our brightest sunshine. Quitting career, moving to a foreign land with two children while also pursuing your own PhD Degree is absolutely crazy! But I am very grateful that we are always together during those hardships, may a great future await us. To my son Arfan and daughter Aimee, you guys have been the bubble and glue for our family, unpredictable yet necessary in keeping us together firmly. To my parents Abah and Ma, thank you for showing me the value of education and respecting others. Many of my decisions surely made you worry, but you still accepted it unconditionally. For my brothers Ngah, Chik and Ayah Su, we are different in every level yet you guys are the most amazing bros that I could ever wish. For my in-laws, thank you for your frequent kind wishes in every moment, a rare thing within my all-boys-family.

For folks in Optical Diagnostics Laboratory especially Shimada Sensei, Toyama, Kuno, Tanaka, Matsudaira, Saruwatari, Nishikawa, Akiyama, Takahara, Kusakari, Kinoshita and Maruyama, thank you very much for the technical supports.

I would like to express my gratitude to Meiji University and MEXT for providing a full scholarship for my study, JST for providing a massive funding for the interesting SIP program as well as Kawasaki City for the awesome resident support. With all the support and blessing, finishing this journey is finally possible.

# LIST OF FIGURES

# LIST OF TABLES

# NOMENCLATURE

| | |
|---|---|
| IC | Internal Combustion |
| CVCC | Constant Volume Combustion Chamber |
| ASI | After Start of Injection |
| EOI | After End of Injection |
| TAIZAC | TAndem Injectors Zapping ACtivation Injector |
| G3P | DENSO 3rd Generation Piezo Element Injector |
| G4P | DENSO 4th Generation Piezo Element Injector |
| G3S | DENSO 3rd Generation Solenoid Element Injector |
| G4S | DENSO 4th Generation Solenoid Element Injector |
| GHC | Green House Gases |
| 1D | One Dimensional |
| UV | Ultraviolet |
| IR | Infrared |
| AHRR | Apparent Heat Release Rate |
| ZEV | Zero Emissions Vehicle |
| CI | Compression Ignition |
| SI | Spark Ignition |
| LTC | Low Temperature Combustion |
| HCCI | Homogeneous Charged Compression Ignition |
| PCCI | Partially Charged Compression Ignition |
| NOx | Nitrogen Oxides |
| UHC | Unburned Hydrocarbon |
| OH* | Hydroxyl Radical Chemiluminescence |
| LES | Large Eddy Simulation |
| RANS | Reynolds-averaged Navier-Stokes |
| EGR | Exhaust Gases Recirculation |
| DBI | Diffused Back Illumination |
| PIV | Particle Image Velocimetry |
| LII | Laser Induced Incandescence |
| LIF | Laser Induced Fluorescence |
| CAD | Crank Angle Degree |
| Fps | Frame Per Second |

# GLOSSARY

| | |
|---|---|
| Liquid Length | Axial spray location of complete liquid fuel vaporization |
| Lift-off Length | Shortest axial spray location of high temperature reaction |
| Soot Onset | Shortest axial spray location of soot particle appearance |
| Entrainment Wave | Increase of air entrainment phenomenon during transient spray deceleration |
| Rectangle | Conventional method of constant injection pressure/rate during entire injection period |
| Rate shaping | Modification of injection rate during injection period |
| Inversed-delta | Progressive injection pressure/rate ramp-down during injection period |
| Heat Release Rate | Rate of heat generation by fuel burning process |
| OH* | Local heat release |
| UV Shadow | Local fuel-air mixture concentrations |

# SUMMARY

The main objective of this research is to improve passenger vehicle Diesel engine thermal efficiency with inversed-delta injection rate shaping strategy. Impacts of the inversed-delta injection on the spray tip rich mixture suppression, reduction of combustion duration as well as wall cooling loss are examined by using an optically accessible constant volume combustion chamber (CVCC) and a single cylinder Diesel engine.

Inversed-delta injection rate shaping is realized with a novel in-house-developed injection rate shaping injector named as TAndem Injectors Zapping ACtivation TAIZAC injector that is simply constructed with two directly-connected commercial injectors. Mixture concentration distribution and air entrainment of the inversed-delta and rectangle injection are examined based on one-dimensional 1D model.

From high-speed simultaneous imaging of direct soot luminosity, UV emissions at 310 nm and UV absorption at 266 nm, it is noted that the inversed-delta injection exhibit spray tip rich mixture suppression, more even flame distribution and shorter spray tip penetration compare to those of the rectangle injection. However, from the apparent heat release rate analysis (AHRR), influence of the inversed-delta injection on the combustion duration reduction is limited. The liquid length and lift-off length are similar in both injection profiles but the soot onset (i.e. first axial location of soot particle observation) is progressively shortened during the injection period for the inversed-delta injection. It can be suggested that air entrainment relative to the injected fuel might be enhanced in the inversed-delta injection beyond the spray midstream region, likely due to large structure growth.

Engine performance test confirmed that inversed-delta injection successfully improved Diesel engine thermal efficiency by 1.0% compared to that of rectangle injection, largely due to significant reduction of cooling loss at 1.3%, while its effect on combustion duration reduction is also marginal.

In the present study, inversed-delta injection by TAIZAC injector successfully exhibit the spray tip rich mixture suppression, cooling loss reduction and engine thermal efficiency improvement but its impact on combustion duration reduction is marginal and need to be addressed in near future.

# TABLE OF CONTENTS

# 1 INTRODUCTION

This chapter will discuss the trends of greenhouse gases and other emissions regulations demand that need to be addressed. Then discussions on whether is the tremendous effort for the internal combustion engine technology particularly the diesel engine is really necessary despite of all of the regulations hurdle and emergence of alternative powertrains. Later, fundamental of Diesel engine combustion and Diesel spray flame will be elaborated prior to the introduction of advanced Diesel combustion strategy. Proposal of inversed-delta injection rate-shaping approach towards improving Diesel engine thermal efficiency will be explained followed by the objectives of this study.

## 1.1 Motivation

### 1.1.1 Global Commitment to Battle Climate Change

Global warming problem has been constantly be one of the hottest issues where the transportation sector emits roughly 30% of the total $CO_2$, the major greenhouse gas GHG. Effort to reduce global GHG emissions through international agreement as such of the 1997 Kyoto Protocol is half-effective, partly due to the withdrawal of the United States and exemption of developing nations at the point of agreement, including China and India. Following the Kyoto Protocol, the first universally binding agreement joined by major GHG-emitting nation to combat the climate change and accelerate the low carbon society is established in year 2015 as the so-called 2015 Paris Agreement. The main target of the Paris Agreement is to keep the rise of global temperature generally lower than 2°C by year 2100. To achieve such ambitious global scale goal, whole fleet in the transportation sector needs to be run fully by Zero Emissions Vehicle ZEV by year 2050.

Alternative powertrain such as electric vehicle may provide the zero emissions criteria but it is important to account for total emissions life cycle including the process of the resource mining and electric power generation. It is estimated that the current electrical power generation is mainly from coal: powering the electric vehicles with coal-generated electric power may worsen the global GHG emissions. Furthermore, sudden large-scale implementation of the electric vehicle will result in electrical power usage surge especially during the expected charging scenario at midnight. Thus, it is much more practical to gradually phasing the GHG emissions reduction level, practically through highly efficient internal combustion engine powertrain and hybrid system combination methods, concurrently with progressive

shifting towards low carbon alternative powertrains and power generation sector. In fact, it is estimated that even by year 2040, approximately 70% of the total vehicle fleet will be fitted at least partially with the internal combustion engine. European Union EU is committed to achieve the Agreement target by setting a major milestone to reduce the GHG emissions by 40% by year 2030 compared to the base year of 1990 prior to full ZEV adaptation by year 2050, refer to Figure 1. Such high GHG emissions reduction requires vast investment and cross-entity collaboration to improve of the current internal combustion engine technology.

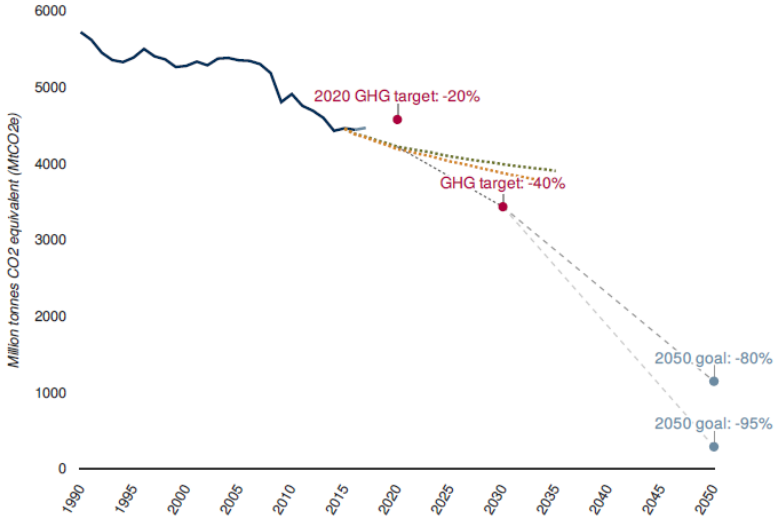


**Figure 1 Greenhouse gas emissions, projections and targets for the European Union EU (in million tons of $CO_2$ equivalents)**[1].

Figure 2 shows a chart of recent emissions standards in Europe, United States, China and Japan for the regulated pollutants. Noted that this chart is accounted only for the passenger or light duty class Diesel engine vehicles, align with the scope of this work. In early introduction of emissions regulation, each country and even each region apply a different set of standards, making it difficult to achieve long-term target of global scale GHG reduction. Thus, proactive attempts have been made to harmonize the recent and future emissions standard and testing procedures worldwide. Historically, the regulations for all emissions are progressive tightened in each policy renewal, occasionally at an order of magnitude difference.

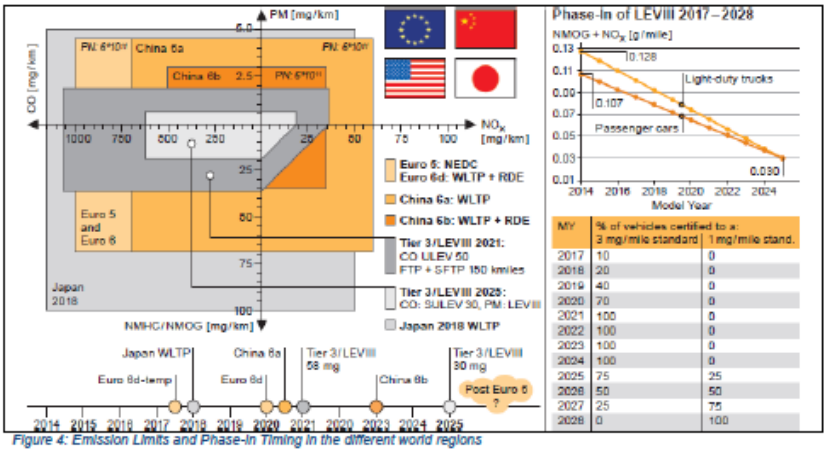

Figure 4: Emission Limits and Phase-In Timing in the different world regions

**Figure 2 Recent emissions standards in the EU, US, China and Japan**[2].

Developments of the modern Diesel engine fuel injection system such as the common-rail and precise injection control system have elevated Diesel engine status as an efficient yet clean powertrain. To comply with strict legislations particularly on the PM and NOx emissions while maintaining its high thermal efficiency, most modern Diesel vehicles are equipped with various after-treatment devices. For example, NOx trap and selective catalytic reduction are able to reduce the NOx emissions by 90% while application of particulate filter reduce near 99% proportion of particulates. However, such sophisticated systems tend to reduce the Diesel engine thermal efficiency and adding roughly 10% of the total vehicle cost, as well as necessity for regular periodic maintenance[3].

With the progressive development of Diesel powertrain technology and ever-increasing global demand of energy for mobility, the future emissions regulations are expected to be exponentially tighter, demanding the engineer and researcher alike to squeeze the highest possible potential of the internal combustion engine technology at least for several decades ahead.

### 1.1.2 Cross-ministerial Strategic Innovation Promotion Program SIP

Together with the United States and Germany, Japan has been consistently spearheaded the automotive industry sector. However, due to the rapid emergence of new technology, fierce competition, ever strict emissions standards and changes of the society demand, innovative measures are imperative for Japan to stay at the top. To maintain the competitive edge in the automotive sector, Japan Cross-ministerial Strategic Innovation Promotion SIP Program was established in year 2014, with the clear target of achieve 50% thermal efficiency for both Diesel and gasoline engines[4].

This program emphasized intense collaboration between the Japanese automakers and top engine researchers in research institutions with a substantial budget totaling at 100 billion yen in 5-year period from the Japanese Government towards accelerating the combustion technology development. Figure 3 shows the SIP project summary for the Diesel Combustion Team. As shown at the top left chart, highest brake thermal efficiency BTE for passenger vehicle Diesel engine by year 2014 was at 43%, indicating that significant reduction in exhaust, cooling and friction loss is necessary to achieve the targeted efficiency.

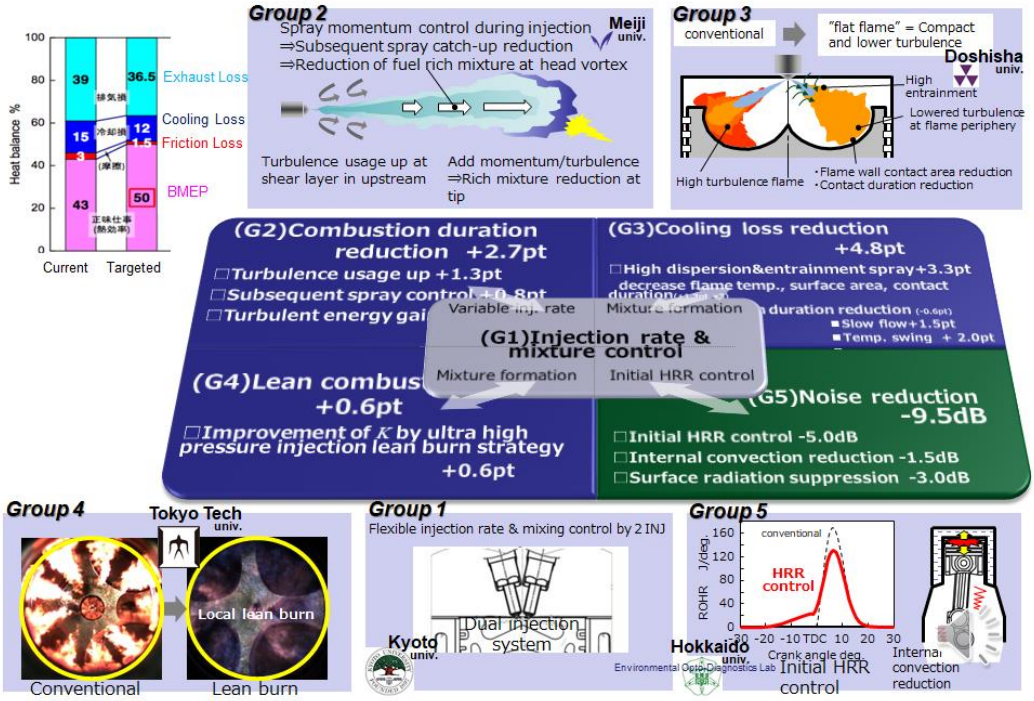


**Figure 3 Summary of the Diesel group framework towards achieving 50% Diesel engine thermal efficiency.**

This study was conducted under Group 2 of the Diesel Combustion Team, aiming to reduce the combustion duration by 40% that estimates 2.7% increment of the thermal efficiency owing to the reduction of the exhaust loss. Towards combustion duration reduction aim, Meiji University had been accounted in conducting fundamental study, formulating a novel strategy, developing technology hardware necessary and demonstrating the effectiveness on actual engine test. Other universities had been given the responsibility for cooling loss reduction, mixture control and so on. If all of the novel technologies proposed could be integrated, it is possible to achieve the thermal efficiency targeted.

## 1.2 Background and Literature Review

### 1.2.1 Fundamental of Diesel Combustion

Diesel engine is invented by Rudolf Diesel in 1880, using a reciprocating engine fueled originally with vegetable oil. Diesel cycle utilizing fuel compression ignition CI property instead of spark plug-assisted ignition SI as in comparable Otto cycle in gasoline engine. Due to its higher compression ratio, Diesel engine exhibits the advantages of higher thermal efficiency, torque and longevity (due to its tough-built to withstand rougher combustion). Although Diesel engine has been viewed as a rough-industrial powertrain, technological advancement in recent decades has significantly improved the emissions and noise during the combustion process.

Figure 4 shows the conventional Diesel combustion heat release rate, typically derived from the pressure histories. The combustion chronology of the Diesel fuel can be summarized as follows. (1) Liquid fuel is injected under high pressure up to approximately 200 MPa into a high-pressure and high-temperature cylinder. Injected liquid fuel will exchange momentum with the surrounding hot air and undergo vaporization. (2) Continuous fuel-air mixing process occurs, preparing a portion of mixture suitable for auto-ignition. Period between the start of injection and ignition timing is known as ignition delay. (3) Sharp increase of pressure shown by high rate of heat release of well-mixed mixture occur during the premixed combustion phase. (4) After the end of the premixed combustion phase, relatively slower rate of heat release can be observed in the diffusion combustion phase. During this phase, mixing and combustion processes take place simultaneously, thus it is also known as the rate-controlled combustion. (5) Combustion process is still ongoing although the injection event was long ended: this phase is known as the late combustion phase, usually observed during the expansion stroke.

Excessively long combustion duration caused by the late combustion reduces the constant volume degree (i.e. combustion duration relative to comparable Otto cycle), leads to higher exhaust loss and deterioration of engine thermal efficiency. However, research conducted on the late combustion mechanism is scarce and mostly limited to the late soot oxidation rather than the heat liberating process itself[5], [6]. This study aims to investigate the fundamental cause behind the late combustion and strategize a potential mitigation method.

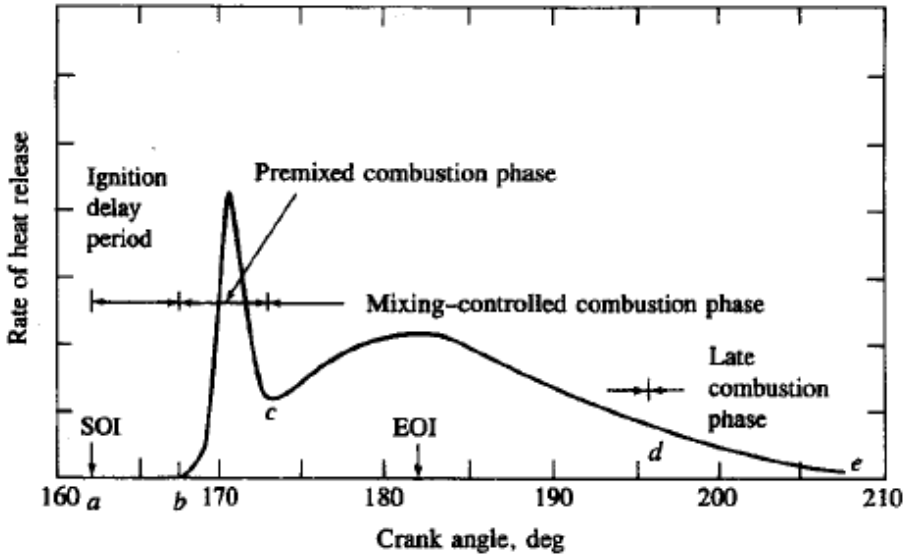


**Figure 4 Example of heat release rate in conventional Diesel combustion**[7].

### 1.2.2 Diesel Spray in Quasi-steady Injection

With the advancement of optical diagnostics development such as high-power high-speed pulse laser and highly tunable wavelength light source, better understanding of the complex Diesel combustion process from fundamental Diesel spray flame study has been accelerated in the past decades. The optical diagnostics method could be applied to visualize the Diesel spray flame directly in the engine test rig and in relatively simple but easier to understand non-impinging Diesel spray inside a combustion chamber.

For example, Dec and co-worker has established a popular Diesel spray flame conceptual model based on laser diagnostics method[8]. It is observed that the Diesel spray flame is surrounded by the thin layer of highly reactive OH radical and soot oxidation process at the spray inner core will not occur due to the absent of the OH radical. Based on simultaneous LII and LIF imaging of the Diesel spray flame, Kosaka et al. added an argument regarding the role of rigorous vortex structure prevalent in highly turbulent Diesel spray should possibly oxidized the soot even at the inner core to a certain extent[9].

Since the Diesel combustion is a rate-controlled process, fuel-air mixing process highly governs the combustion event. With the current optical diagnostics technology, it is possible to quantitatively measure the microscopic air entrainment amount in the Diesel spray via the particle image velocimetry PIV method of trace particles doping and via ultraviolet UV absorption based approach as in the laser absorption scattering LAS method[10]–[13].

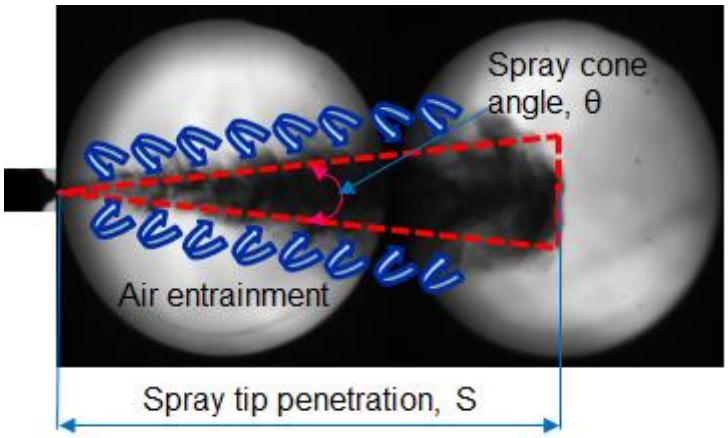


**Figure 5 Schematic diagram of the Diesel spray tip penetration and cone angle in non-vaporizing conditions.**

Despite of those detail optical diagnostic methods, it is greatly convenient to investigate the air entrainment amount from the Diesel spray macroscopic observation of the tip penetration and the cone angle, which consist of relatively simple optical setup. Figure 5 shows the schematic diagram of a Diesel spray macroscopic property such as the tip penetration, cone angle and air entrainment along the spray surface marks by the curly arrows. Most well-known spray tip penetration model as proposed by Wakuri et. al. is based on the spray momentum conservation point of view[14]. Wakuri mentions that the Diesel spray should be viewed as the gas jet as the liquid fuel reach instant atomization since it is injected with high pressure into a very dense surrounding. Recent study using advance optical diagnostics method indeed reveal that the air entrainment amount surpass the injection fuel amount at a distance very near to the nozzle orifice, emphasizing that the Diesel spray can be viewed as the gas jet[15], [16].

Equation (1) shows the tip penetration model of the Diesel spray derived by Wakuri in non-vaporizing conditions. However, this model can also be extended to the modern injector and in reacting conditions with a little modification[17], [18]. From the equation, the Diesel spray traveling downstream at a rate proportional to the $t^{0.5}$ due to the gradual fuel-air mixture mass increment according to the principle of momentum conservation. From this spray tip penetration model, one could be able to estimate the amount of entrained air as well. Hiroyasu and Arai extended this observation by including the tip penetration prior to the liquid fuel break-up and atomization process immediate to nozzle orifice as shown in Equation (2) and (3).

$$S = \left(\frac{2c\Delta P}{\rho_a}\right)^{0.25}\left(\frac{td}{tan\theta}\right)^{0.5} \quad (1)$$

$$S = 0.39\sqrt{\frac{2\Delta P}{\rho_f}.t} \quad (0 < t < t_b) \quad (2)$$

$$S = 2.95\left(\frac{\Delta P}{\rho_a}\right)^{1/4}\sqrt{D_n}\sqrt{t} \quad (t_b < t) \quad (3)$$

Where $S$, $c$, $\Delta P$, $\rho_a$, $\rho_f$, $t$, $t_b$, $d$ and $\theta$ represents spray tip penetration, discharge coefficient, injection pressure, ambient air density, fuel density, time, liquid fuel break-up time, nozzle orifice diameter and spray cone angle, respectively.

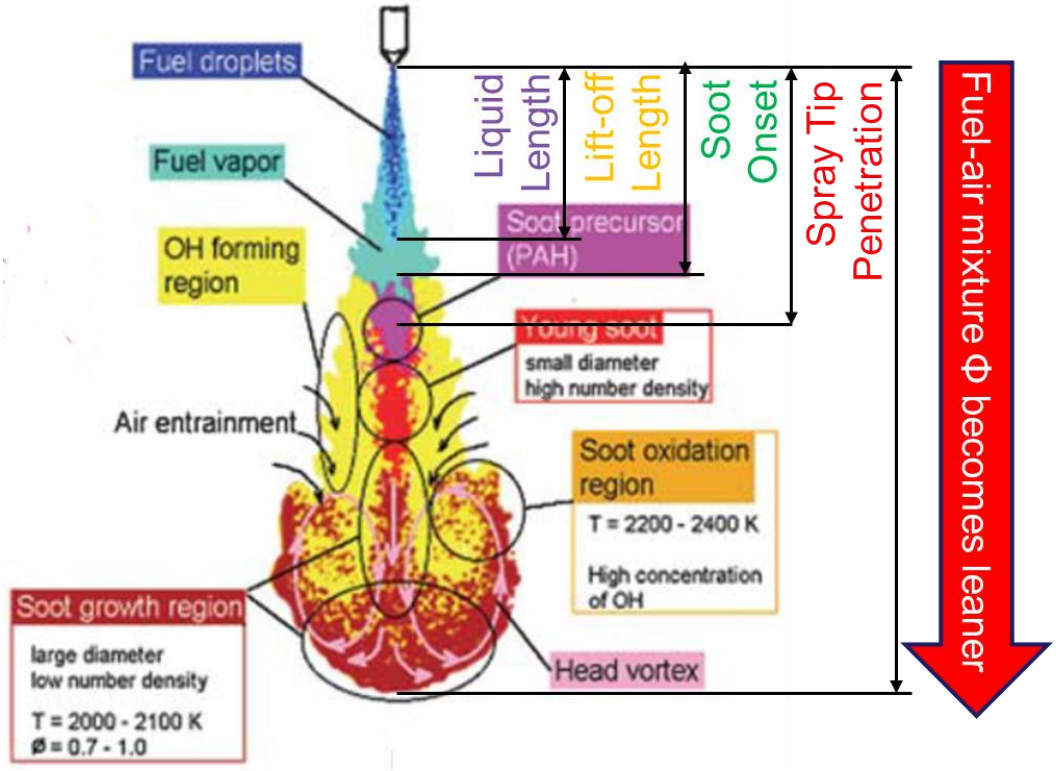


**Figure 6 Conceptual model of soot formation and oxidation process in Diesel spray flame with additional annotations**[9].

To discuss in further details regarding the fuel-air mixing process in the Diesel spray flame, the soot oxidation model from the Kosaka et. al. is adapted as shown in Figure 6[9]. It is widely accepted that the Diesel combustion and soot emissions behavior are highly dependent on the events occurring at near injector tip or the Diesel spray flame upstream region where high number of strong shear vortices present: so-called liquid length and lift-off length typically serve as an indirect

indicator for fuel-air mixing and auto-ignition process, respectively[19]–[25].

Study of fuel liquid phase penetration is of interest in the Diesel spray and combustion community. The injected Diesel fuel will be atomized and mixed with hot ambient gases before completely vaporize at a quasi-steady axial location known as the liquid length. Extensive liquid penetration study conducted by Naber and Siebers concluded that the liquid length is a mixing-limited vaporization process or in other words, the amount of time needed for fuel to vaporize can be neglected and the amount of entrained air relative to that of the injected fuel (i.e. mixture fraction property) governs the location of complete vaporization[21], [22]. Equation (4) and (5) show the respective ambient air entrainment mass flow rate $\dot{m}_a$ and injected fuel mass flow rate $\dot{m}_f$ and Equation (6) express the liquid length, $L$ with the vaporization enthalpy consideration $B(T_a, P_a, T_f)$[20], [26]. Where $a$ and $b$ are a constant value respectively at 0.66 and 0.005, while $c_a$, $d$, $U_f$ and $\theta$ is area-contraction coefficient, orifice diameter, injection velocity/pressure and spray cone angle, respectively.

$$\dot{m}_a \propto \sqrt{\rho_a \rho_f} d U_f \tan\left(\frac{\theta}{2}\right) \tag{4}$$

$$\dot{m}_f \propto \rho_f d^2 U_f \tag{5}$$

$$\mathrm{L} = \frac{b}{a} \frac{\sqrt{c_a} d}{\tan(\theta/2)} \sqrt{\left(\frac{2}{B(T_a, P_a, T_f)} + 1\right)^2 - 1} \tag{6}$$

Lift-off length is defined as the stabilized onset location of quasi-steady hydroxyl chemiluminescence OH* that indicates a high-temperature reaction. The location of the lift-off length is usually observed slightly downstream to the liquid length, depending on the injection parameters and ambient conditions; some researchers reported that it might be overlapped or appear shorter than the liquid length due to its line-of-sight nature of measurement [12, 16, 19, 35, 36]. The location of the lift-off length profoundly impacted the subsequent soot formation that take places further downstream [4, 37, 38].

Peters concluded that the flame stabilization $H$ in a gas-jet occurs at a location where the convective flow in downstream direction is balanced by the flame propagation in upstream direction along the stoichiometric layer, described by Equation (7) [15, 39, 40]. From the diesel spray flame OH* high-speed imaging, Pickett et al. noticed that several auto-ignition kernels appear separately from the quasi-steady lifted flame downstream, suggesting that the auto ignition could govern

the lift-off length in some cases, as express by Arrhenius-like relation in Equation (8)[18]. $U$, $Z_{st}$, $a_t$, $\rho_a$, $T_a$ and $S_L(Z_{st})$ refers to jet velocity, stoichiometric mixture fraction, thermal diffusivity, ambient density, ambient temperature and laminar flame speed of a stoichiometric mixture, respectively.

$$H \propto \frac{UZ_{st}\alpha_t}{[S_L(Z_{st})]^2} \tag{7}$$

$$\tau_H \propto 9.19 \times 10^{-6} \exp\left(\frac{6534}{T_a}\right) {\rho_a}^{-0.96} {Z_{st}}^{-1.89} \tag{8}$$

### 1.2.3 Diesel Spray in Transient Injection

Note that the Diesel spray characteristics in the above-mentioned subsection are referring to the study under quasi-steady injection condition. Recently, advanced transient spray injection strategies are applied, including multiple injections, low temperature combustions LTC and injection rate-shaping.

Multiple or split injection scheme usually consists of pilot, main and post injection: each injection could be further divided into several smaller amount of injections. Multiple injection has been proven to be able to reduce the harsh engine noise originated from higher premixed-mixing heat release peak and accelerate soot oxidation process by providing additional mixing during the late combustion phase. Recently commercialized DENSO 4$^{th}$ generation piezo element G4P injector is able to realize ultra-high injection pressure up to 270 MPa with the capability to precisely control the actuation timing even to zero-dwell injections. Utilizing this state-of-the art injector functions, Horibe et. al has successfully increased Diesel engine thermal efficiency by 1.2% without significant trade-off with the regulated emissions[27]. Study of the split injection effects on the macroscopic spray structure of split injection, the air entrainment associated and transient flame development are reported by Desantes and Noud et. al[28], [29]. Meanwhile Moiz et. al investigated the effects and mechanism of multiple injection from the simulation approach[30].

In recent decade, LTC strategies such as in homogeneous-charged compression ignition HCCI and partial-charged compression ignition PCCI case are gaining considerable attraction since it might potentially able to simultaneous reduce NOx and soot emissions while maintaining the high thermal efficiency benefit of conventional CI engine. However, its high unburned hydrocarbon UHC and engine knocking problems hinder the implementation of these combustion strategy for production Diesel engine.

From the optical diagnostics of the Diesel spray flame under LTC conditions, Musculus et. al revealed that the spray tail region mixtures become too lean, leads to unfavorable UHC formation as illustrated in Figure 7[5], [31]. It can be observed that the upstream region consists of over-lean mixture compared to the downstream region, contrary to the conventional Diesel spray flame where the mixture becomes leaner as it travels downstream due to the progressive mixing event[32].

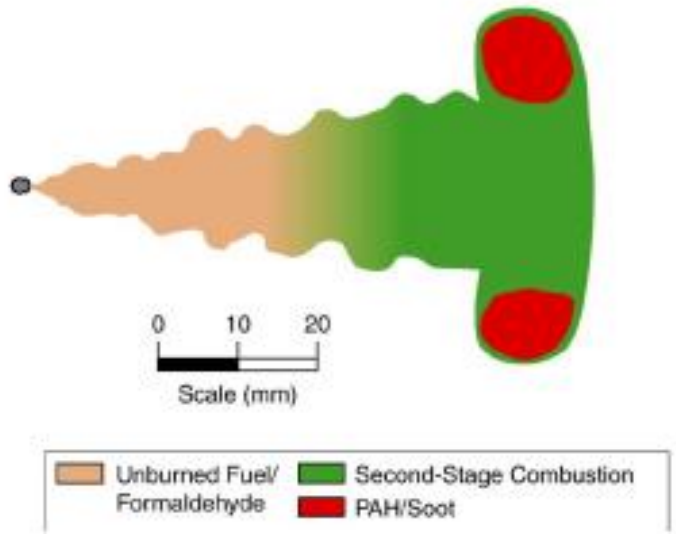


**Figure 7 Diesel Partially-Premixed Compression-Ignition (PPCI) conceptual model from Musculus et al.**[32]

From this observation, Musculus et al. introduce the concept of end-of-injection EOI entrainment wave, i.e. the air entrainment is enhanced starting from the upstream region as the injection event was ended[33], [34]. It is argued that just after the injection event was ended, intense ambient air entrained into the spray to compensate the space vacated by the sudden fuel supply disruption in order to temporarily conserve the spray momentum. Schematic diagram of the entrainment wave can be referred to one-dimensional 1D simulation results as shown in Figure 8. The horizontal axis indicates the value of air entrainment amount throughout the spray at any particular axial location compared to that of a steady Diesel spray (i.e. value higher than unity means that the air entrainment rate is higher compared to that of steady spray and vice-versa). Several bumps appear after the EOI emphasized that the air entrainment is promoted after the EOI compared to that of the steady jet. It is interesting to note that that the air entrainment enhancement begins at the upstream region and growing bigger as it travels downstream, with a shape resemble the wave of air entrainment. Eagle et. al has conducted double-pulse

PIV experiment to validate the air entrainment promotion in the Diesel spray during transient EOI. From the experiment results, it is confirmed that the entrainment wave does present but the peak of each wave is broader and smaller than the simulation[35].

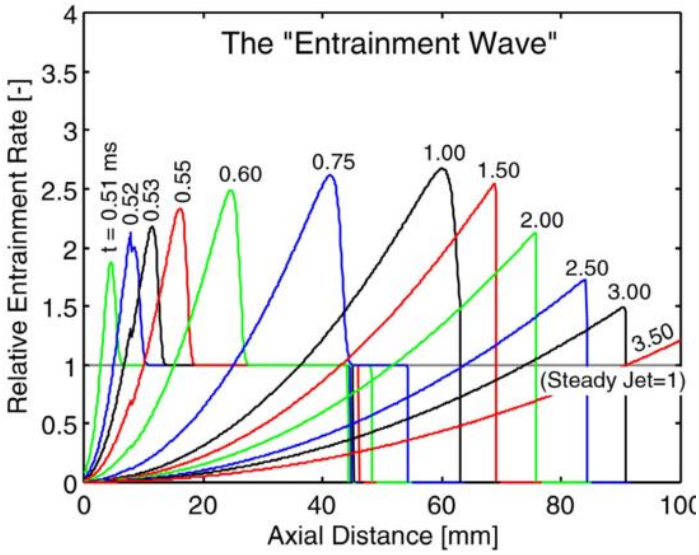


**Figure 8 Illustration of air entrainment promotion after the end of injection resembling the "Entrainment Wave" proposed by Musculus et. al**[33].

Kook et. al investigate the impact of transient EOI on the liquid length. It is observed that during the EOI transient, the steady liquid length recedes towards the nozzle tip depending on several parameters such as the injection pressure, orifice diameter and EOI ramp-down rate[26], [36]. The liquid length recession does not seem to occur if the injection pressure or the EOI ramp-down rate are too small. Utilizing similar model used by Musculus et. al[33], it was concluded that faster needle closing at higher injection pressure and larger orifice induced stronger and faster entrainment wave due to the significant air entrainment to fill the spray volume vacated by the fuel supply disruption. In conclusion, if the entrainment wave head is faster than the liquid vaporization rate, the liquid length recession will occur.

With the same argument, Knox et. al study the effect of the EOI transient on the lift-off length[37]–[40]. Similar to the Kook et al. findings, it is observed that the quasi-steady lift-off recedes towards the nozzle tip during the EOI transient. Termed as combustion recession. The combustion recession is caused by the local auto-ignition event instead of the mismatch between the mixture momentum and flame propagation speed typically observed in the gas furnace study. It is interesting to note that the combustion recession tends to occur with lower injection pressure,

smaller orifice and slower EOI ramp-down rate, contrary to that of liquid length recession but the underlying mechanism is exactly similar: stronger entrainment wave leads faster liquid length recession but results in over-lean mixture at the spray upstream region, which suppress the combustion recession event.

A relatively new approach for transient Diesel spray can be referred to the control of the fuel supply rate itself during the injection period as termed as injection rate-shaping. Juneja et al. study the optimization of injection rate shaping tbased on the simulation approach[41]. It is concluded that the injection rate- shaping affects the ignition characteristics and temporal histories of soot and NOx productions, suggesting the potential of the injection rate-shaping in controlling the combustion and emissions characteristics.

Wakisaka and Azetsu develop a highly flexible injection rate-shaping injector based on direct control of needle lift using piezo element stack[42], [43]. It is observed that the injection rate-shaping influences the spray tip penetration and spatial distributions of the flame temperature. Using comparable device, Macian et al. reported that boots or ramp-up shape injection rate-shaping is able to reduce the combustion noise, reducing spray tip penetration and liquid length as well as affecting the combustion products spatial distributions compare to that of conventional injection[17], [44]–[48], suggesting that the injection rate-shaping approach could widen the mixture formation control flexibility, potentially able to improve the Diesel engine thermal efficiency and emissions level. To date, robust injection rate-shaping system at reasonable price is unavailable, hindering the progress of injection rate shaping examination and application on the Diesel engine.

### 1.2.4 Proposal of the Late Combustion Reduction

Modern diesel engine tends to employ small orifice injector nozzle due to the benefit of better mixing and lower smoke emissions[49]–[51]. However, this strategy elongates the injection period, results in longer combustion duration, lower constant degree volume and consequently thermal efficiency deterioration. Effort to shorten the injection duration with ultra-high injection pressure is hampered by harsh engine noise, higher NOx emissions and significant cooling loss trade-off[52], [53].

Aligned with the SIP program framework mentioned in Figure 3, the scope of this study is to investigate the potential of the injection rate-shaping strategy in reducing the late combustion towards Diesel engine thermal efficiency improvement. However, literature on the late combustion mechanism is scarce, even the terms of the late combustion itself is rather vague.

In attempt to gain insight of the late combustion mechanism, time-sequence images of Diesel spray flame under modern Diesel engine-like conditions are acquired from simultaneous imaging of UV emissions at 310 nm, UV laser absorption at 266 nm and direct flame photograph for visualization of local heat release, mixture concentration and to exclude the soot UV radiation and UV absorption influence, respectively. Figure 9 shows the optical setup (left) and an image example during late combustion period (right)[54] while adequacy of the OH chemiluminescence at 310 nm wavelength as the local heat release marker can be referred elsewhere[55]. During this period, it can be observed that considerable amount of heat release (see orange line at the left side in Figure 9) and notable OH chemiluminescence as well as thick fuel mixture concentration appears at the spray head. Thus, it can be concluded that the late combustion heat release could be originated by the rich mixture stagnating at the spray tip, called as the spray tip rich mixture.

Since the experiment is conducted in a free spray conditions, one might argue that this phenomenon might be oversimplified and might differ in the actual Diesel engine combustion mechanism. To confirm the spray tip rich mixture formation in the production Diesel engine during the late combustion, Hasegawa et. al plugged an UV endoscope at one of the engine cylinder exhaust valve: schematic diagram of optical setup and result is depicted at the left side of Figure 10[56], [57]. It is noted that the appearance of OH* signal at the spray tip during the late combustion is also valid for the Diesel engine combustion. Details on cross-sectional local mixture concentrations and heat release of Diesel spray inside the engine during the late combustion is examined by Reynolds Average Navier-Stokes RANS simulation by Adachi et. al as shown at the right side of Figure 10[55].

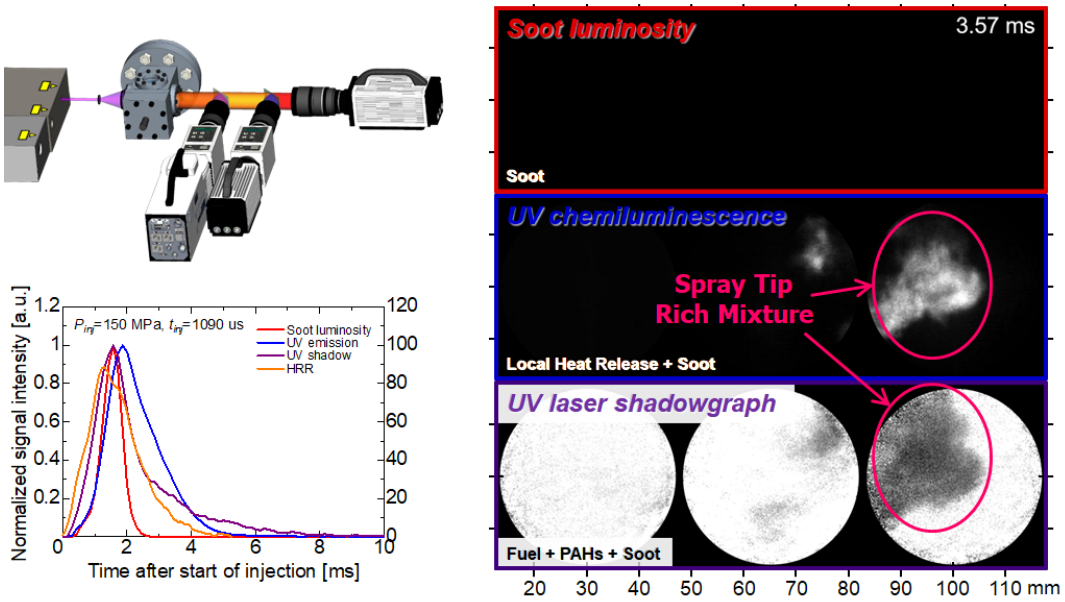


**Figure 9 Visualization of the spray tip rich mixture during late combustion phase via simultaneous high-speed UV imaging technique**[54].

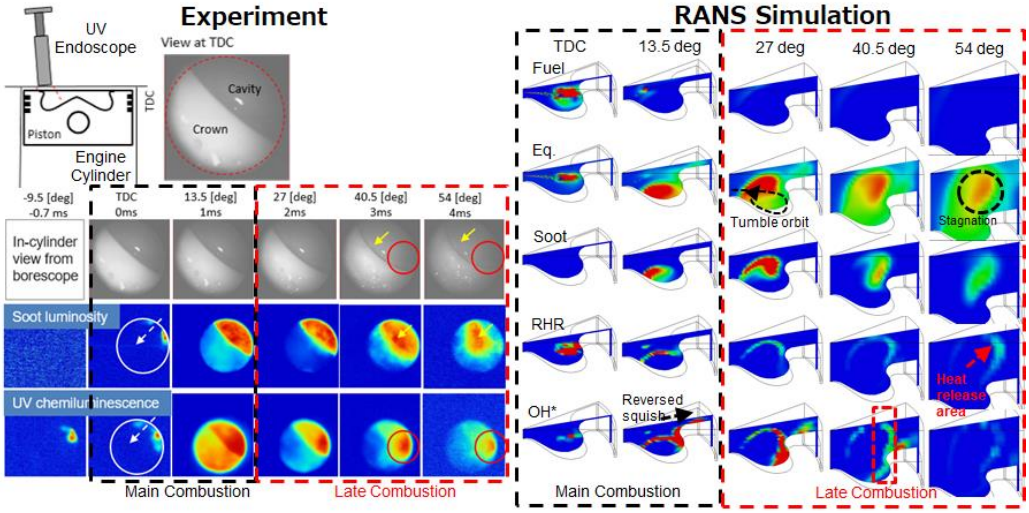


**Figure 10 Investigation of late combustion phase in the production Diesel engine (left) and RANS simulation result (right)**[56], [57].

In conventional injection, except from a very short period of transient needle opening and closing, fuel is injected at a relatively steady rate as in square, rectangle or "top-hat"-like shape. Fuel parcel injected initially experience rapid momentum exchange with still and dense surrounding air, reducing its velocity and results in easier catchup for the following spray. Then, the spray head will either clumping

together with the catchup fuel and continue travelling downstream or being push away in spray lateral direction as can be observed as the head vortex[58]–[60]. Furthermore, if the spray mixture undergo combustion, following spray is expected to travel much faster due to the low local density induce by the high temperature reaction at the downstream region[28], [61]. All of the scenarios mentioned favor the formation of the spray tip rich mixture, possibly leads to higher late combustion phase as illustrated at the left side in Figure 11.

In this study, high initial injection pressure followed by continuous progressive ramp-down rate shaping as in inversed-delta shape is proposed for the late combustion suppression strategy as illustrated at the right side in Figure 11, and the arguments of this rate shaping selection are as follows. Firstly, by slowing down the following spray velocity, catchup motion with the previous spray and the accumulation of the spray tip rich mixture could be suppressed. Secondly, analogous to the entrainment wave phenomenon during transient end-of-injection EOI period, local air entrainment might be promoted during the ramp-down deceleration period thus might results in faster combustion duration[33], [34]. Furthermore, by reducing the following spray velocity the spray head momentum should be smaller compared to that of rectangle injection, leading to shorter penetration[62], [63]. The inversed-delta injection could potentially reduce exhaust loss and cooling loss due to shorter combustion duration and smaller spray flame wall impingement momentum, respectively[64].

To gain some insight on the inversed-delta injection effects on combustion duration, a comprehensive large eddy simulation LES study couple with detail kinetic scheme was conducted by Adachi et. al as a part of the SIP project scope[55]. From the LES results, it is predicted that the inversed-delta injection is able to reduce the spray tip rich mixture and significantly shorten the combustion duration compared to that of rectangle injection. However, it should be noted that such an impactful simulation data especially the inversed-delta injection spray and combustion mechanism needs to be validated.

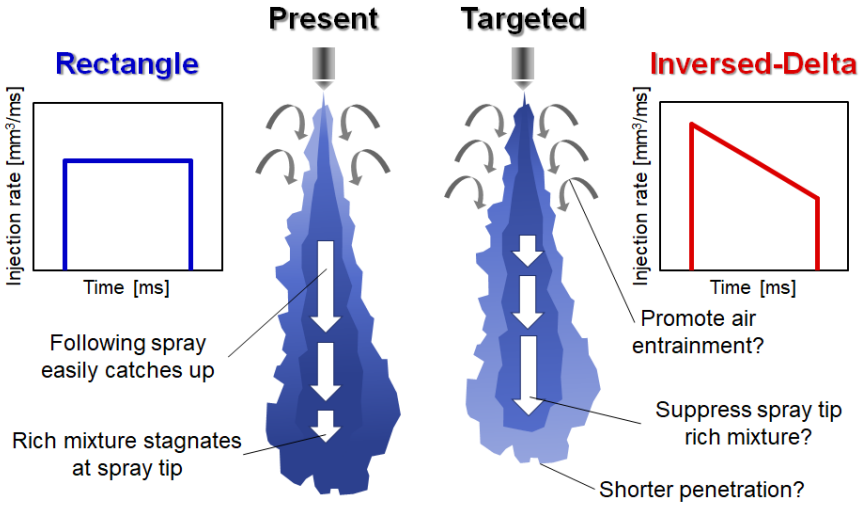


**Figure 11 Illustration of proposal of inversed-delta injection rate-shaping for the reduction of late combustion**[65].

### 1.3 Objectives

From the previous discussions, it is evident that the knowledge regarding on the late combustion is limited and no attempt was made to directly address this problem. Additionally, only a few studies reported on the effects of injection rate shaping on Diesel spray flame behavior but most work focus only on the ramp-up injection rate shaping, highlighting the importance of this study from the fundamental and engineering perspective. To summarize this chapter, the objectives of this dissertation are as follows:

1. Design and construct an inversed-delta rate-shaping injection system for constant volume combustion chamber CVCC and Diesel engine test.
2. Reduce the Diesel late combustion through the spray tip rich mixture formation suppression and combustion duration reduction. Various high-speed imaging diagnostics are conducted to evaluate the effectiveness of inversed-delta injection and to provide useful insight for injection rate shaping impacts on Diesel spray flame and combustion characteristics.
3. Reduce the Diesel engine cooling loss. Novel optical diagnostic techniques to investigate its mechanism through high-speed IR radiation of wall-impinging Diesel spray flame is developed and conducted.
4. Improve thermal efficiency of passenger vehicle Diesel engine while keeping the emissions level at manageable level. Further investigation is conducted in the CVCC for better understanding on the soot production mechanism.

# 2 APPARATUS AND METHODOLOGY

This chapter will discuss experimental setup and conditions for the constant volume combustion chamber CVCC utilized throughout this study. Brief explanation regarding in-house developed TAndem Injectors Zapping ACtivation TAIZAC injection rate shaping injector principle and assembly followed by its axial spray extraction and injection rate examination. Then various high-speed optical diagnostics setup and its image processing method will be discussed. Later, one-dimensional 1D simulation principle and validation is elaborated. Finally, single cylinder engine test setup, condition and heat balance key calculation will be explained.

## 2.1 Constant Volume Combustion Chamber

### 2.1.1 Experimental System

CVCC is one of the most widely use type of device that can flexibly simulate high temperature, pressure, density ambient conditions and gas composition comparable to that of modern Diesel engine and beyond. Furthermore, absence of impingement wall and easy optical window installation permits fundamental observation of complex Diesel spray flame structure in the actual Diesel engine condition. In fact, most of recent understanding on Diesel spray, chemical reaction and emissions process are mainly derived from the non-impinging Diesel spray flame investigation using CVCC approach[12], [13], [22], [49], [66]–[70].

The CVCC can be further categorized into two types, namely premixed gases combustion and continuous flow: both methods yield comparable result that can be referred seamlessly. However, since the research work are carried out independently in various research institute worldwide with loose setup and conditions definition, the experimental results obtained might contradict with each other, hindering and diluting the Diesel spray combustion understanding effort. Hence, international collaboration within engine researcher communities called Engine Combustion Network ECN framework is initiated to promote standardization of experimental conditions, reliability of data and so on [50], [63], [71], [72].

In this study, Diesel spray and combustion experiment were conducted in a premixed gases type of CVCC equipped with three 35-mm-diameter quartz windows with a TAIZAC injector mounted at its head, and a magnetic stirrer at the opposite side as illustrated in Figure 12. Common-rail pump system use was capable to supply up to 200 MPa fuel pressure, while the chamber is heated continuously at 100°C to

avoid water condensation. Premixed gases of acetylene, argon, carbon dioxide and oxygen were charged and continuously stirred even during the diesel combustion event to promote more homogenous gases mixture. A combination of argon and carbon dioxide gas was selected over natural pure nitrogen gas charge since it provides comparable specific heat ratio product and ambient density but with much lower peak pressure. As the premixed gases combustion was ignited with a spark plug, the pressure of the premixed gases will rise up to 10 MPa peak and decrease afterward due to wall heat loss. The fuel was then injected at the ambient pressure desired for the Diesel combustion, note that the ambient temperature is resultant from the bulk pressure and the ambient density depends on the premixed gases composition. Injected Diesel spray images were acquired with high-speed camera with preferential optical setup. Finally, the combustion products were purged out in each run where a full cycle of test takes approximately 10 minutes, relatively longer than the continuous flow CVCC type but it is safer due to its transient nature[20], [72].

Since the effective viewing field was relatively small compared to the spray length, distance from the injector nozzle tip to the view field were varied by inserting a combination of spacers to visualize the upstream, midstream and downstream region. Separated spray images from these regions were combined or stitched together to mimic a whole image of the Diesel spray flame.

Pressure histories acquired with a high-response Kistler 6125C11 Pressure Transducer attached at the magnetic stirrer side was used for apparent heat release rate AHRR derivation. Equation (9) shows the calculation of AHRR from the combustion chamber pressure trace obtained. Here dV/dt and dk/dt were treated as zero since constant and large chamber volume compared to the injected fuel amount.

$$\frac{dQ}{dt} = \frac{1}{k-1} V \frac{dP}{dt} + \frac{k}{k-1} P \frac{dV}{dt} - \frac{PV}{(k-1)^2} \frac{dk}{dt} \tag{9}$$

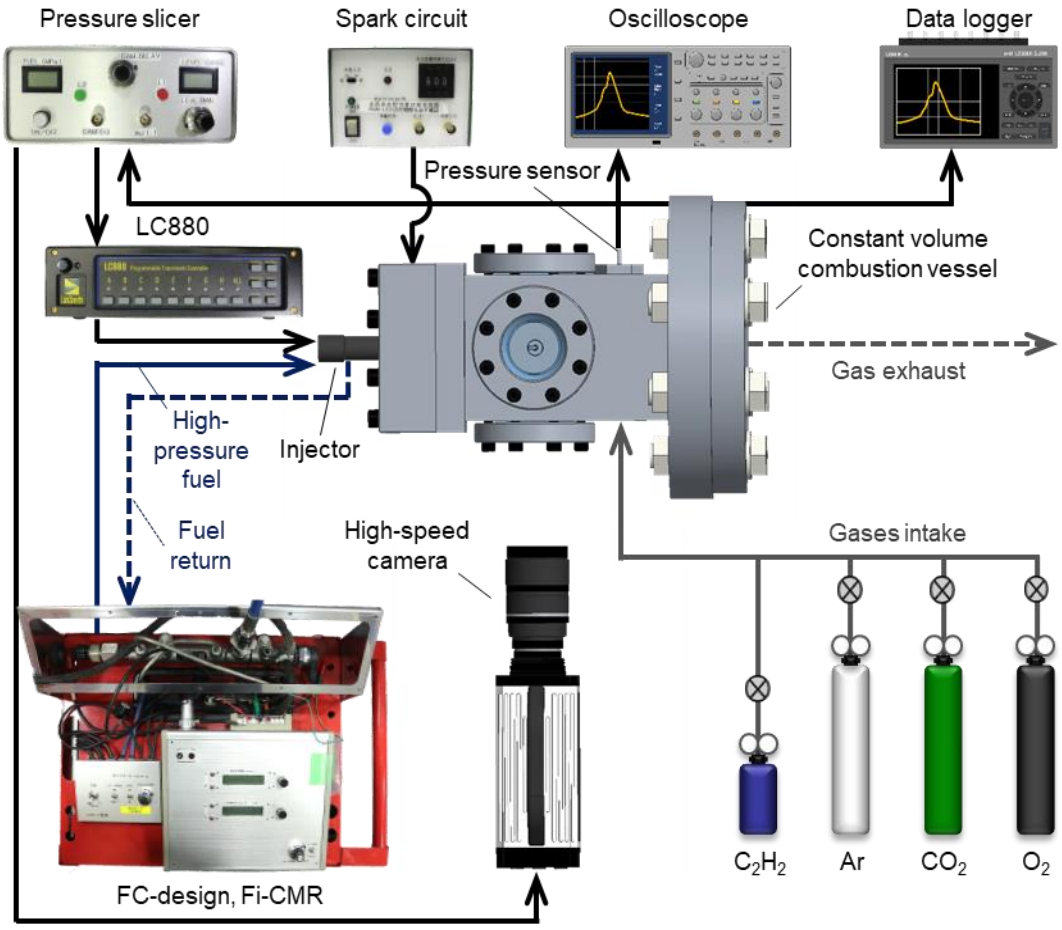


**Figure 12 Schematic diagram of constant volume combustion chamber system.**

### 2.1.2 Experimental Conditions

Table 1 shows the experimental conditions including reacting (17% oxygen), non-reacting (0% oxygen) and non-vaporizing (100% $CO_2$) conditions. Since modern Diesel engine is highly boosted and applied with exhaust gases recirculation EGR system, high ambient gas density at 23.8 kg/m$^3$ and oxygen concentration at 17% was simulated, respectively. Temperature of 1050 K was a bulk temperature estimated based on the CVCC pressure, and had been validated using a thin type-K thermocouple at approximately 15 mm from the nozzle tip (i.e. the expected location of auto-ignition event)[73]. For non-vaporizing condition, 100% of $CO_2$ at 1.6 MPa was charged into 373 K heated CVCC to produce similar ambient gas density as in reacting and non-reacting conditions. A TAIZAC injector with 8+1 φ0.12 mm orifices, yielding total of 45 mg of injection mass was installed: details on TAIZAC injector and nozzle orifice arrangement will be discussed in the next section.

Table 1 Experimental setup and ambient conditions in reacting, non-reacting and non-vaporizing cases

| | Unit | Value, Notes |
|---|---|---|
| **Ambient gas density, $\rho_a$** | $kg/m^3$ | 23.8 |
| **Ambient temperature, $T_a$** | K | 1050 (Reacting, Non-reacting)<br>373 (Non-vaporizing) |
| **Ambient pressure, $P_a$** | MPa | 5.4 (Reacting, Non-vaporizing)<br>1.6 (Non-vaporizing) |
| **Ambient $O_2$ concentration** | vol % | 17 (Reacting)<br>0 (Non-reacting) |
| **Ambient $CO_2$ concentration** | vol % | 100 (Non-vaporizing) |
| **Injector** | | TAIZAC |
| **Nozzle** | | φ0.12 mm x 8 + 1 |
| **Fuel** | | JIS2 |
| **Total mass, $m_f$** | mg | 45 |

## 2.2 TAIZAC: A Novel Rate Shaping Injector

### 2.2.1 Operating Principle

To realize the inversed-delta injection rate shaping in this study, a novel injector called TAIZAC (TAndem Injectors Zapping Activation) is designed and constructed in-house by mainly utilizing and modifying commercial injectors. Thus, TAIZAC is relatively a low-cost rate-shaping injector compared to piezo-stack injector and can be mounted directly onto the engine head as any common commercial injector with comparable robustness.

Figure 13 shows the TAIZAC injector schematic diagram (left side) and its operating principles (right side), and details were discussed in another publication [74]–[76]. TAIZAC injector consists of two commercial injectors, namely an upper and a lower injector, directly connected with an in-house fastening part. TAIZAC injector can operate at 270 MPa common rail pressure without any leakage.

By controlling the actuation timing for both injectors, injection rate shaping desired can be performed. For example, as shown on the right side of Figure 13, progressive injection ramp-down rate as in inversed-delta injection rate shaping can be achieved by supplying the fuel to the lower injector firstly through upper injector needle actuation while keeping the lower injector needle close. Then by closing the upper injector needle, the lower injector will be charged with fuel hydraulic pressure while being isolated from the common rail supply line. Finally, once only the lower

injector needle actuates, fuel will be injected initially at high pressure then gradually decreases as the accumulated hydraulic pressure is being release. On the other hand, by actuating both injectors at approximately the same time, conventional rectangle injection can also be achieved.

The inner volume of the lower injector is essential in determining the ramp-down rate of inversed-delta injection. Therefore, the DENSO fourth generation solenoid G4S injector was selected for the lower injector due to its compact solenoid element construction near the needle, permitting body cut which results in smaller lower injector inner volume and faster inversed-delta injection ramp-down rate. Meanwhile, the DENSO third generation piezo G3P injector was selected for the upper injector due to its superior response.

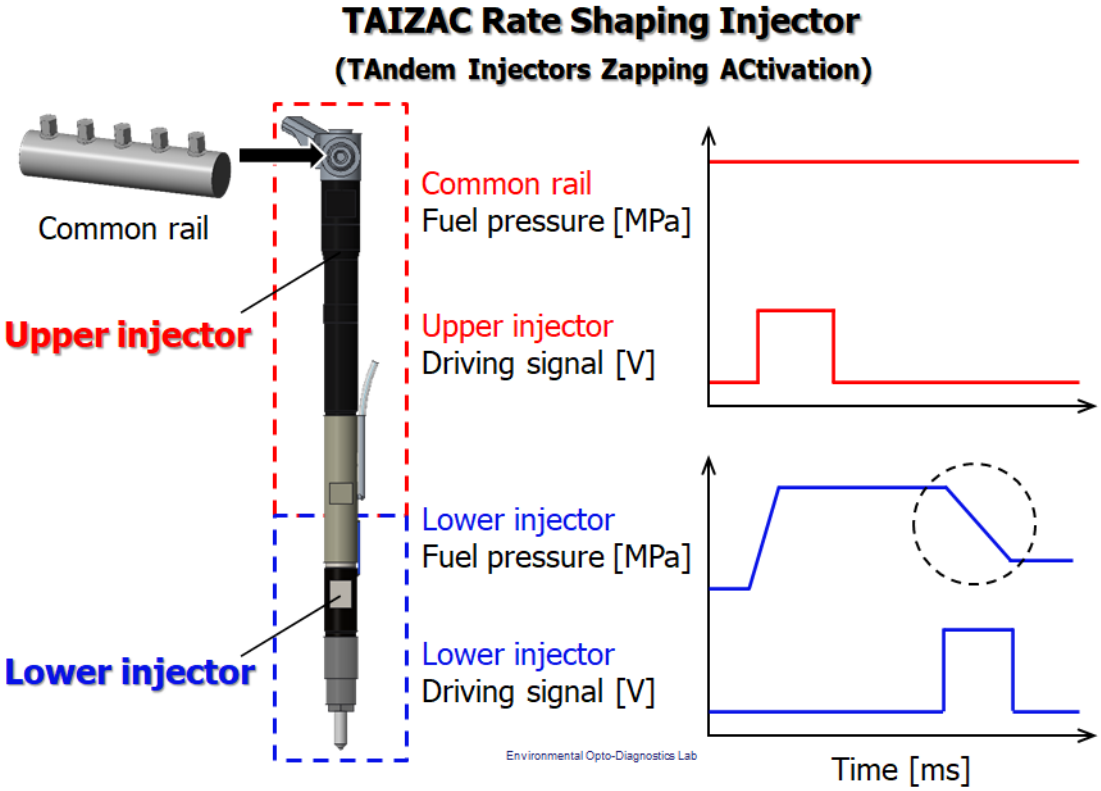


**Figure 13 TAndem Injector Zapping ACtivation TAIZAC (left) injector schematic diagram and (right) operating principles**[74].

Figure 14 shows the example of the pressure inside the TAIZAC injector (red line) and G4S injector (blue line) measured with a strain gauge attached directly at the lower part of injector body, actuation signal timing and injection rate from 10 shots ensemble average obtained with a Bosch-type long tube method injection rate meter at the top, middle and bottom chart, respectively. Note that this data was obtained

from commercial nozzle tip at φ0.12 mm × 8 orifices at 40 mg injection mass in total. It can be observed that the inversed-delta injection rate shaping was successfully achieved within a relatively short 1.7 ms injection period (i.e. comparable with injection period in actual Diesel engine), demonstrate the TAIZAC injector potential for this study main target of the late combustion suppression and combustion duration reduction.

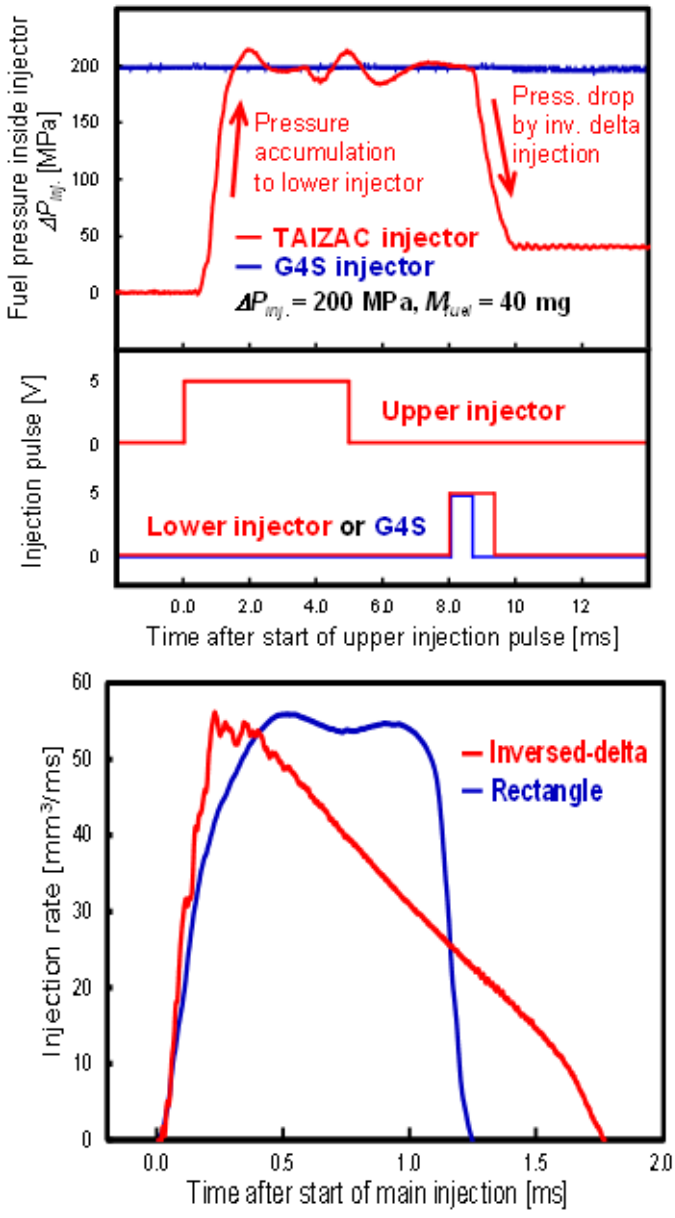


**Figure 14 Example of fuel pressure inside the TAIZAC injector (red line) and DENSO G4S injector (blue line), injection actuation signal and injection rate at the top, middle and bottom chart, respectively**[74].

### 2.2.2 Single Spray Extraction from Multi-orifices Nozzle

In order to investigate the TAIZAC inversed-delta injection potential on the late combustion reduction, it is useful to study a single non-impinging or free Diesel spray flame[12]. However as aforementioned, TAIZAC relies on fuel dischargement rate to realize inversed-delta rate shaping, where to achieve significant ramp-down rate within a short injection period, it was necessary to use a multi-orifices nozzle instead of a single orifice nozzle used typically in CVCC experiments[63], [72]. Thus, a method to extract only a single spray while avoiding interference from other orifices was proposed and examined in this section[77].

By considering the CVCC geometric and machining time limitation, additional φ0.12 mm cylindrical shape orifice was drilled axially on commercial φ0.12 mm × 8 nozzle tip axis. Then an injector nozzle cap with a φ2-mm axial hole was attached to the injector to extract only the axial spray as illustrated in Figure 15. A thin copper gasket was attached between the nozzle and the nozzle cap, and two pressure-releasing holes were drilled at the base of the nozzle cap to avoid fuel back flow from the radial spray accumulated inside the nozzle cap. The nozzle cap was removed and cleaned after at about 30 shots and no significant fuel residue detected inside the nozzle cap, probably because it was burnt during the premixed gases combustion in the next run.

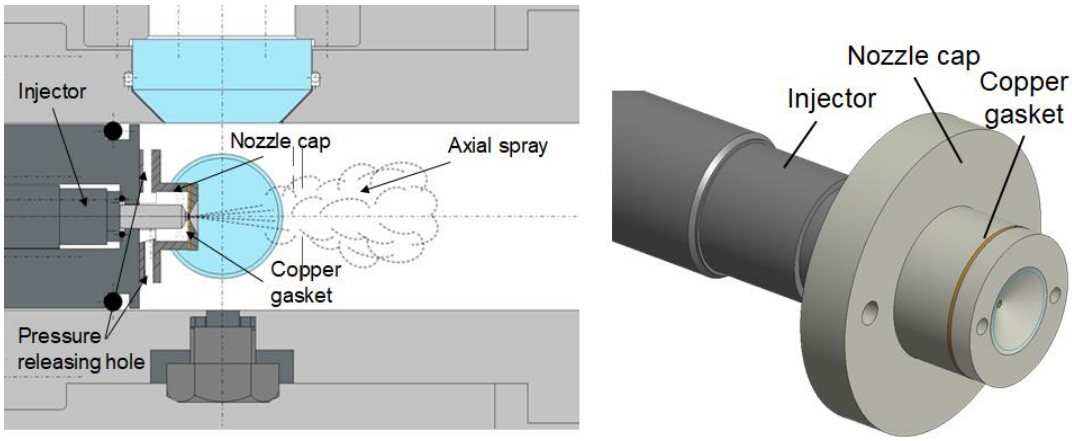


**Figure 15 Illustration of axial spray extraction (left) and closeup view of nozzle cap-attached injector (right)**[77].

Injection amount was examined by injecting the fuel into a container at atmospheric condition where the mass before and after injection was measured using a high-precision electronic balancing machine. Ensemble average at 10 runs of total injection amount from TAIZAC multi orifices φ0.12 mm × 8 + 1 and a single φ0.12

mm axial orifice injection was measured at 45 mg and ranging from 3.4 mg to approximately 5.0mg, respectively. Relatively low injection amount from the axial spray compared to other radial orifices was expected due to its peculiar position and non-tapered cylindrical shape orifice[78], [79] where cavitating orifice was reported to reduce value of flow coefficient from as low as 0.7[80].

### 2.2.3 Axial Spray Examination Based on Momentum Method

Although the axial spray can be extract from multi orifice nozzle by using the nozzle cap, its injection profile is unclear. Since the axial orifice is located at different axis than the other orifices and no hydraulic grounding was performed, examination of actual injection rate from this spray was of interest. Bosch type long-tube injection rate meter is capable to measure the injection rate from TAIZAC injector, but it shows the injection rate results accumulated from all orifices instead from only the axial spray targeted. Several researchers measured single spray directly inside a high-pressure CVCC based on spray momentum conservation principle[15], [38], [81]–[84].

Figure 16 shows a sketch of spray momentum test rig where non-vaporizing spray was injected from left to right, impinging a strike cap attached to a force-calibrated Kistler 6125C11 pressure transducer with an instant-drying rigid glue. If the impinging spray radius is adequately smaller than that of the strike cap, it can be assumed that all the spray hits the strike cap and then moves sideways perpendicular to the spray axis. With this assumption and according to the momentum conservation principle, the spray impinging force F will be equivalent to momentum flux $\dot{M}_f$ at the orifice outlet and any other points along the spray axis, in steady injection case as depicted in Equation (10) and (11) where $P$ and $A$ represents pressure signal acquired and strike cap area at the pressure sensor side, respectively.

$$\mathrm{F} = \dot{M}_f \tag{10}$$

$$\mathrm{P} = \frac{\dot{M}_f}{A} \tag{11}$$

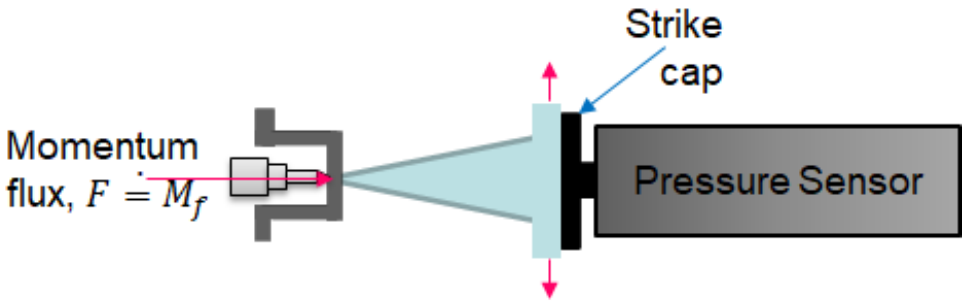


**Figure 16 Illustration of spray momentum test rig for TAIZAC injector axial spray examination.**

Several caution points need to be address in this spray momentum test rig as follows. (1) The strike cap needs to be larger than the spray width or located near enough to the nozzle tip to ensure valid pressure measurement[84]. (2) The strike cap needs to be lightweight since heavy material or excessively large strike cap will absorb the spray force instead of conveying it to the pressure sensor[85]. (3) For more accurate measurement, the strike cap surface must be smooth and not too big in diameter to avoid any vortex formation at its surface[83]. In this study, several parameters such as ambient gas density, impingement distance and injection rate shaping profile were examined for the inversed-delta and rectangle rate shaping injection as shown in Table 2.

**Table 2 Experimental conditions for spray momentum test.**

| | **Unit** | **Value, Notes** |
|---|---|---|
| **Ambient gas density, $\rho_a$** | $kg/m^3$ | 0.0, 9.8, 23.8 |
| **Impingement Distance, S** | mm | 15, 25, 35 |
| **Ambient temperature, $T_a$** | K | 373 |
| **Strike Cap Material** | | Aluminum |
| **Strike Cap Surface Area, $A_s$** | mm | 6 |
| **Strike Cap Connecting Area, $A_C$** | mm | 2 |
| **Ambient pressure, $P_a$** | MPa | 1.6 |
| **Ambient $CO_2$ concentration** | vol % | 100 |
| **Injector** | | TAIZAC |
| **Injection Conditions** | | 175 MPa Inversed-delta<br>175 MPa Rectangle |
| **Nozzle** | | φ0.12 mm x 8 + 1 |

Figure 17 shows the injection mass from the axial spray derived by integrating the value of the spray momentum rate obtained. The actual mass of the inversed-delta and rectangle injection at axial spray were measured by weighting the mass of a container before and after 10 injections, valuing at approximately 5 mg for the injector used particularly for this test. It can be observed that the accuracy of the injected fuel mass is inversely proportional to the impingement distance since less spray impinge the strike cap as the spray width grows as it travels downstream. It was interesting to note that, medium ambient density at 9.8 kg/m$^3$ tends to yield more accurate results, probably the spray becomes less wider compare to that of higher density one and less vortex is produced compare to that of low density one.

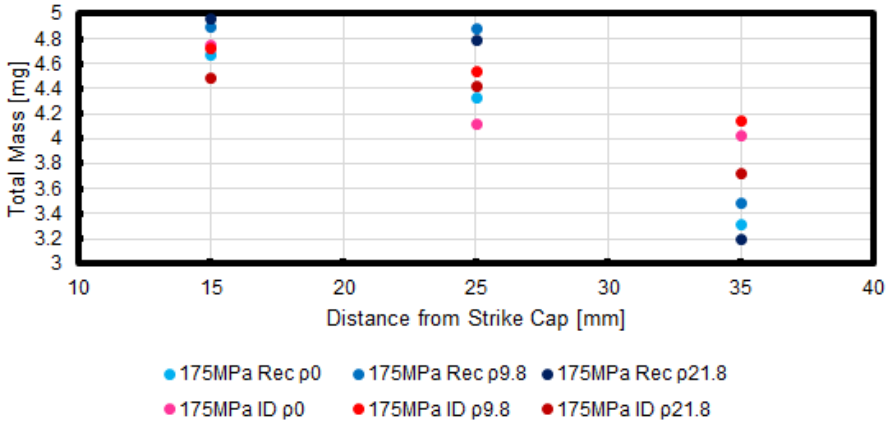


**Figure 17 Fuel injection mass for inversed-delta and rectangle injection derived from the spray momentum flux.**

From Equation (12), spray momentum flux or impinging force F can be converted to the injection rate $\dot{Q}$, where $c$ was the constant coefficient. Figure 18 shows the comparison of the inversed-delta and rectangle injection rate acquired from momentum method (at 15 mm impingement distance and 9.8 kg/m$^3$ density) and Bosch long-tube method (one-ninth from the total value). It is exciting to note that the injection characteristics as in the peak value and general rate shaping shape were highly-matched, suggesting that the axial spray extracted via nozzle cap is adequate enough to represent the inversed-delta and rectangle injection for optical diagnostics examination. It can also be observed that detection response of initial rising slope was faster in the momentum method, since the fuel is injected into less dense ambient air compared to extremely dense fuel tank in Bosch-type long-tube method, suggesting that the momentum method could probably yield a more accurate results for injection rate measurement[86].

$$\dot{Q} = \sqrt{\frac{\mathrm{Fc}A_{orifice}}{A}} \tag{12}$$

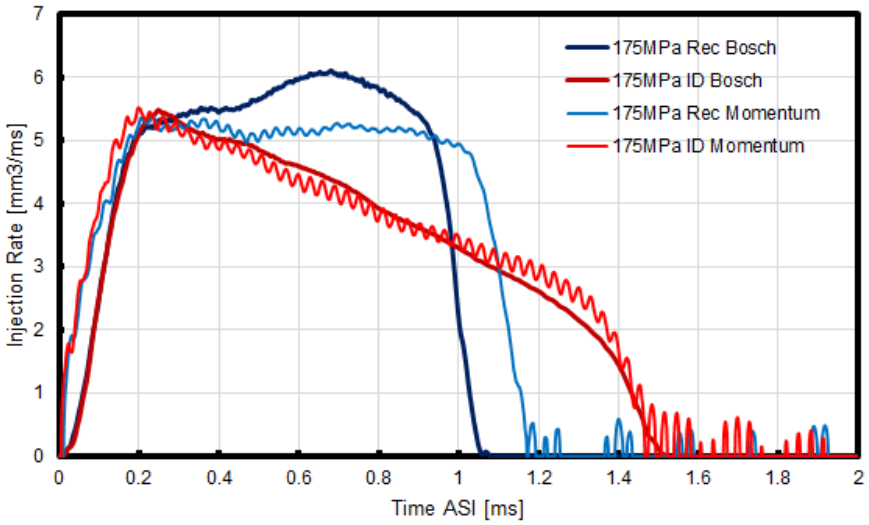


**Figure 18 Injection rate derived from the spray momentum method compare to that of Bosch long-tube method.**

## 2.3 Optical Diagnostics

### 2.3.1 Simultaneous High-speed UV Imaging

Referring to our past publication regarding the late combustion visualization[87], similar optical setup shown in Figure 19 was replicated for this study to confirm the spray tip rich mixture suppression in the inversed-delta injection compare to rectangle injection. Visualization of the late combustion heat release location and mixture concentration with soot-induced radiation and absorption can be achieved by comparing the simultaneous images of 310 nm UV emissions (targeting OH* bandwidth) and 266 nm deep UV absorption (targeting absorption of multiple combustion-related species such as fuel-derived and combustion-derived aromatics in the Diesel fuel.) with flame luminosity, respectively. High-speed camera for UV emissions and UV Diffused Back Illumination DBI imaging was equipped with an UV intensifier each. Two dichroic mirrors were used to directed the respective wavelengths into the band pass filters attached to each camera. For UV DBI image acquisition, a widely tunable Ti: sapphire, high-repetition pulsed laser was used as UV light source at oscillation wavelength, repetition frequency and energy at 266 nm wavelength, 7 kHz and 21 mJ/pulse, respectively while camera acquisition setup conditions is shown in Table 3.

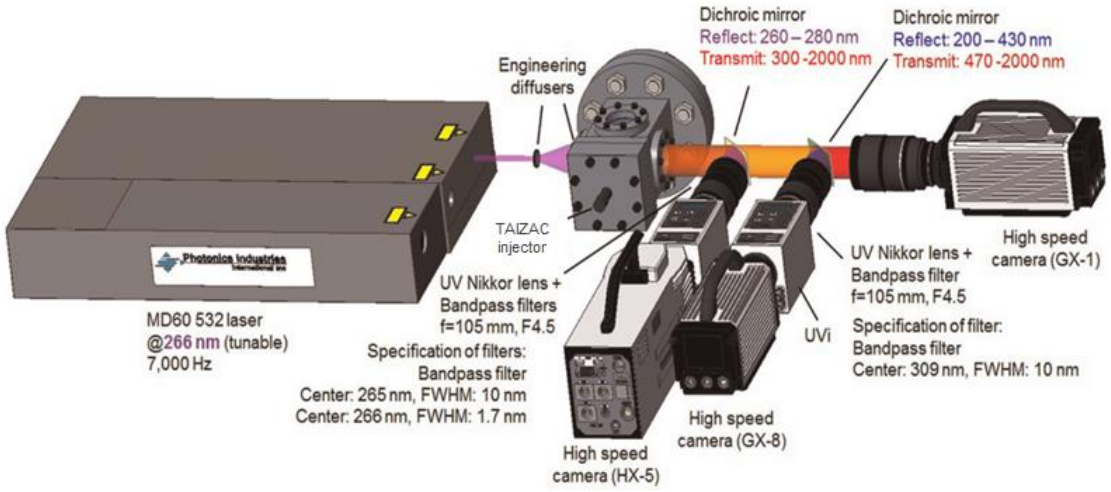


**Figure 19 Setup of diesel spray flame simultaneous UV DBI, UV emissions and soot luminosity high-speed imaging**[77].

**Table 3 Camera acquisition setup for high-speed simultaneous imaging.**

| Image | Camera | Frame rate (fps) | Gate (μs) | UVi Gain | Pixels |
|---|---|---|---|---|---|
| **Soot luminosity** | GX-1 | 7000 | 2 | - | 464 × 464 |
| **UV emission** | HX-3 and UVi | 7000 | 100 | 40 | 896 × 896 |
| **UV laser DBI** | HX-5 and UVi | 7000 | 2 | 25 | 960 × 960 |

Example of high-speed images via this method are shown in Figure 20. Top, middle and bottom images represent soot luminosity, UV emissions at 310 mm and UV DBI at 266 mm, respectively. In early combustion period, strong UV signal intensity from soot radiation and dark shadow from the soot cloud interfered with the interpretation of 310 nm UV signal from OH chemiluminescence and 266 nm shadow from fuel-gas mixture UV absorption. Nevertheless, after the extinction of the soot luminosity, location of the late combustion heat release can be observed, as the abovementioned spray tip rich mixture.

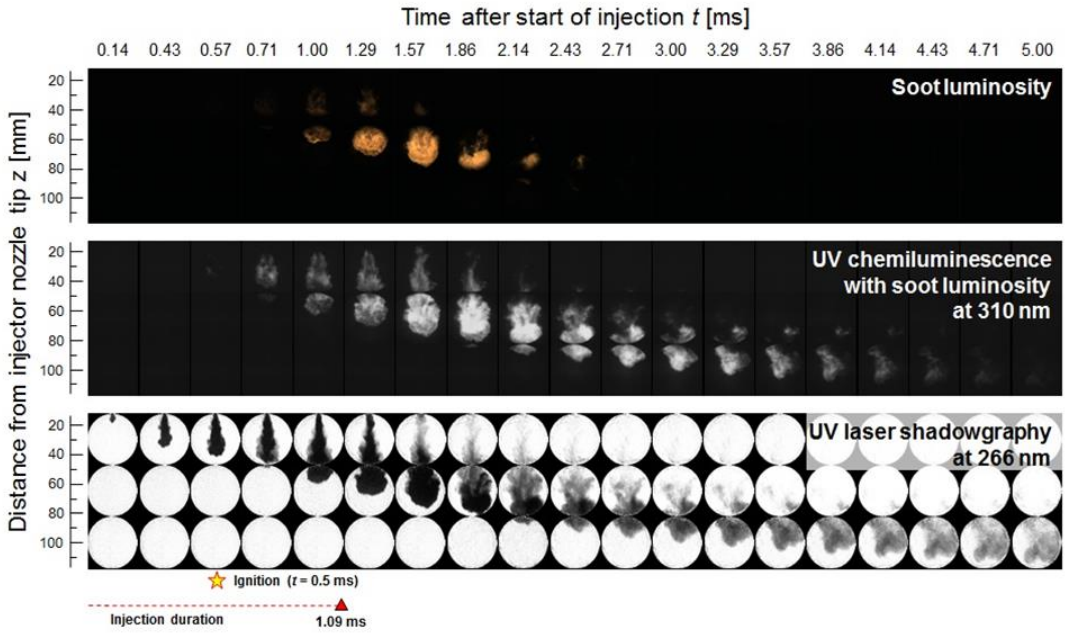


**Figure 20 Example of high-speed images of soot luminosity (top), UV emissions (middle) and UV DBI (bottom) of diesel spray flame. Ambient conditions: $\rho_g$=23.8 kg/m$^3$, Pa=4.8 MPa, Ta=1050 K and 17% $O_2$. Injection conditions: φ0.123 mm orifice, $t_{inj}$=1.09 ms, $m_f$=5 mg and $P_{inj}$=150 MPa** [87].

### 2.3.2 Diffused Back Illumination DBI

From the Equation (4) and (5), it is stated that the injection pressure does not influence the liquid length (axial location of complete fuel vaporization) as the amount of entrained air related to the injected fuel are both directly proportional to the injected fuel velocity $U_f$ (i.e. determine from the injection pressure $P$) suggesting that the liquid length should also remain constant with any injection rate shaping, although marginal relationship of liquid length with ambient and injection parameters is also reported[88]. Musculus et al. study revealed that the air entrainment could be increased up to threefold in transient decelerating injection rate case during the EOI ramp-down period based on transient jet momentum conservation principle[33], [34]. Thus, a shorter liquid length might be anticipated in the progressive ramp-down rate inversed-delta injection as the amount of air entrainment relative to the injected fuel is expected to be enhanced during the injection period. With a similar argument, fuel mixture local equivalence ratio - "layer" could also be shifted towards the nozzle tip, probably leads to shorter soot onset (i.e. closest distance from nozzle orifice to initial soot formation location) due to its high dependency to equivalence ratio ∅[19], [88].

Figure 21 shows the optical setup for the liquid length measurement using Diffused Back Illumination DBI method. Typically, scattering light from liquid fuel perpendicular to the light source as with the Mie Scattering method is preferred for liquid fuel phase penetration measurement. However, Manin et al. suggested that the DBI method can yield consistent results with the Mie scattering with some advantages of a reference light intensity and spatial information, although high threshold level needs to be applied due to beam steering effects[89]. Furthermore, the axial location of soot particle or the soot onset can be simultaneously observed with this method. In this study, a continuous wave 445 nm laser at 700 mW was diffused twice to provide a homogeneous background before penetrating the combustion chamber, and the time-sequence images are acquired with a NAC HX-5 high-speed camera equipped with a 445 nm band-pass filter at 100,000 fps. The setting for optical diagnostics for DBI method and UV emissions which follows later is summarized as in Table 4.

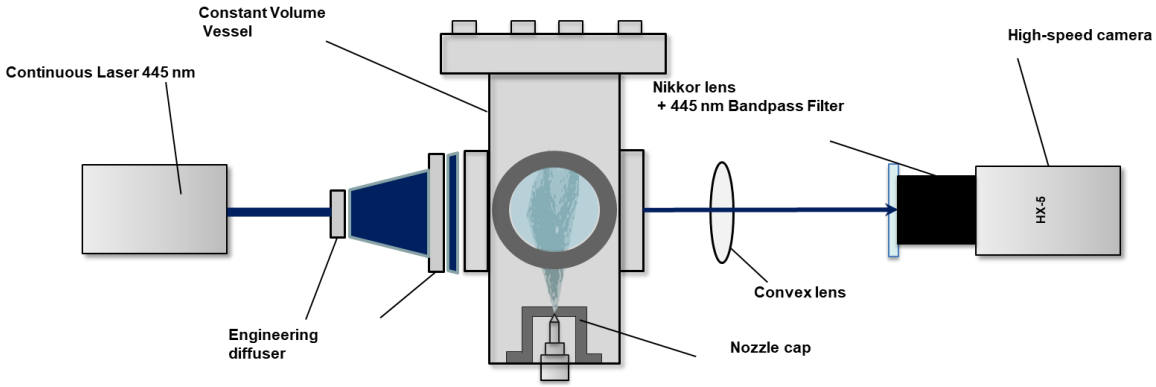


**Figure 21 Optical diagnostics setup of DBI imaging for the liquid length and soot onset**[90].

**Table 4 Camera setting for high-speed optical diagnostics of laser DBI and UV emissions.**

| Image | Subject | Camera | Frame rate fps | Gate μs | Gain | Pixels | Pixel to mm |
|---|---|---|---|---|---|---|---|
| Laser DBI | Liquid length Soot onset | HX-5 | 100,000 | 5 | - | 464×144 | 0.0754 |
| UV emissions | Lift-off length | HX-5 + UVi | 30,000 | 33 | 50 | 512×368 | 0.0684 |

The example of DBI high-speed images are presented in Figure 22, and the image processing method using ImageJ freeware is described as follows[69]. Noise from the camera sensor or the dark current was firstly removed by subtracting all pixels with the average value of non-illuminated regions at the top-left, top-right, bottom-left and bottom-right corner. Each time step image $N_{th}$ was then divided by the background image $N_0$ to remove the background light inhomogeneity. The mean intensity value of 2 × 30-pixel area centering at the jet axis was measured along the spray centerline as depicted in the 0.05 ms timing with a yellow rectangle. The liquid phase and soot particles significantly block the background light while the beam steering from the vapor phase attenuates the signal by approximately 20%. Hence, threshold level at 70% was applied for the liquid length penetration and soot onset measurement.

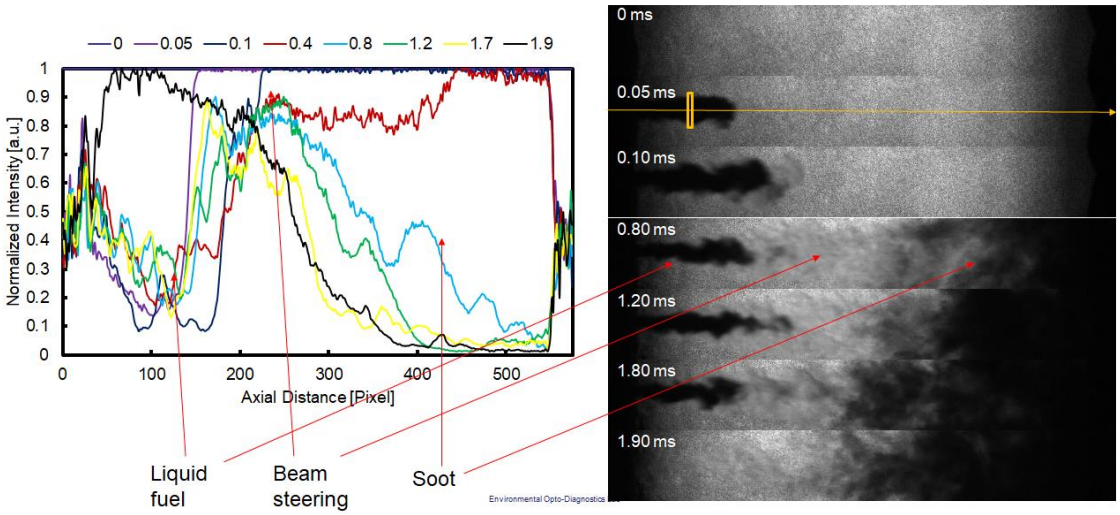


**Figure 22 Example of the high-speed DBI image analysis procedures**[90].

### 2.3.3 Ultra-violet UV Emissions

Investigation on the lift-off length (location of stabilized autoignition) in the inversed-delta injection diesel spray flame is appealing since the fuel velocity reduction and the air entrainment enhancement during the injection period are both expected in the inversed-delta injection. Figure 23 shows the optical setup for the lift-off length imaging of diesel spray flame. Line-of-sight signal from the excited state OH chemiluminescence, OH* was acquired using a NAC HX-5 high-speed camera equipped with an UV intensifier and a 310 nm bandpass filter at 30,000 fps as summarized in Table 4. Note that this image was taken separately from the high-speed DBI imaging.

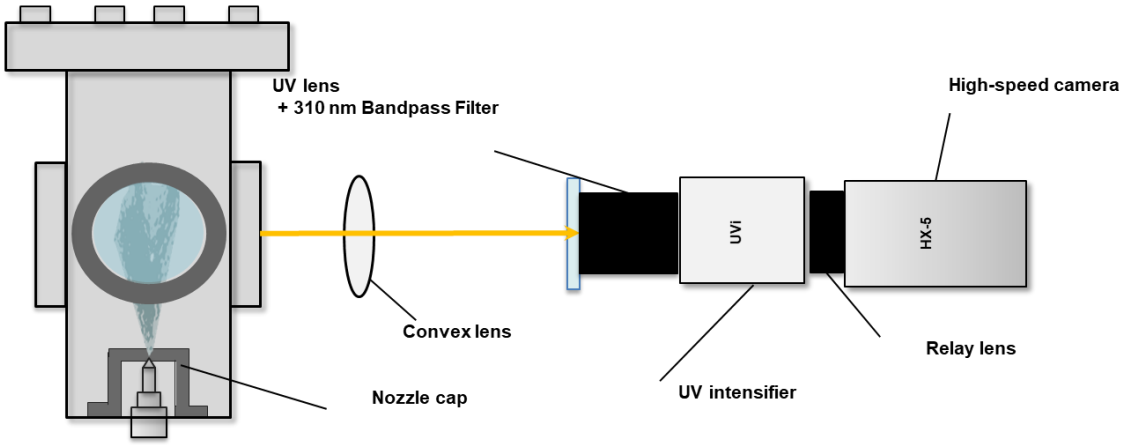


**Figure 23 Optical diagnostics setup of the lift-off length**[90].

The examples and procedures of the image processing method using the ImageJ freeware can be referred to Figure 24. For the processing routine, the dark current was removed by simply subtracting the time step image $N_{th}$ to the background image $N_0$. The threshold for the 16- bit brightness value image was set at 30 counts, and 8-pixel radius median filtering was applied to adequately remove the UV intensifier high noise without significant penalty of difference over the original image. Mean intensity value of 2 × 368-pixel area centering at the spray axis was then measured along the spray centerline as depicted with an orange rectangle at the right image. As suggested in the literature, the lift-off length threshold was applied at the 50% of maximum intensity value in each times steps[22], [38], [69], [91].

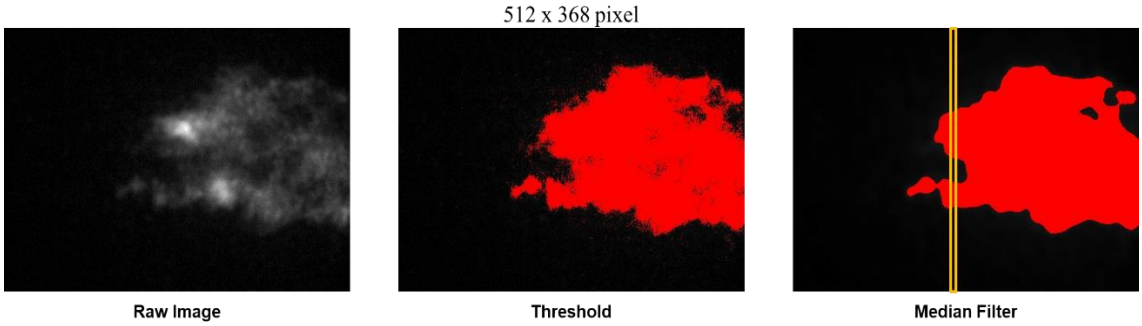


**Figure 24 Examples of the high-speed UV emissions image processing procedures of raw image (left), threshold (middle) and median filtering (right)**[90].

## 2.4 One Dimensional 1D Simulation

### 2.4.1 1D Diesel Spray Model Principle

Relatively simple yet powerful 1D model has been developed to describe the phenomenon occurs in a direct injection diesel spray based on the fuel velocity and momentum supply at the nozzle tip[92], [93]. From Wakuri's Diesel spray to the gas jets analogy, Naber and Siebers have developed first order-reduced model, greatly improved the understanding of Diesel spray physics in quasi-steady injection case such as in the mixing-limited vaporization theory proposed[21]. To explain the air entrainment wave concept, Musculus and Kattke have expended this model to after end of injection EOI period based on transient transport of fuel mass $m_f$ and jet momentum $M$ within the Diesel jet as depicted in Equation (13) and (14), respectively[33]. As illustrated in Figure 25, the Diesel spray is discretized in a one-dimensional array of control volumes along the spray axis where the transient transport for fuel mass and jet momentum in each control volume are calculated as the sequence from the previous time step.

$$\frac{\partial m_f}{\partial t} = \dot{m}_{f,in} - \dot{m}_{f,out} \tag{13}$$

$$\frac{\partial M}{\partial t} = \dot{M}_{f,in} - \dot{M}_{f,out} \tag{14}$$

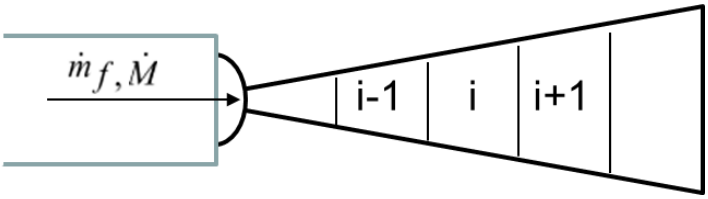


**Figure 25 Illustration of one-dimensional discrete control volume diesel spray.**

From this 1D model approach, they have successfully demonstrated and described the EOI entrainment waves concept and later validated the results with double-pulsed Particle Image Velocimetry PIV experiment of Diesel spray during EOI transient [33], [94]. Recently, a comparable 1D model is used to explain the mixing and combustion processes in split injection strategy[28]. The air entrainment and fuel distribution are expected to be highly influenced by the inversed-delta injection rate shaping but it is difficult to be measured quantitatively. Thus, comparison of the inversed-delta and rectangle injection is conducted using a 1D discrete model based on Musculus and Kattke model with a simple modification on the injection rate shaping [30, 31].

### 2.4.2 1D Simulation Validation

For validation, two injection patterns were simulated for each rectangle and inversed-delta injection, one is with finite ramp period and another one is with instant rising pulse denote respectively by approximation (Appr) and simplified (Simp) as shown in Figure 26. The actual values of ambient density $\rho_a$ fuel density $\rho_f$, ambient temperature $T_a$ and nominal orifice diameter $d$ as shown in Table 1 were utilized. Meanwhile, contracted-area coefficient $c_a$, contracted-diameter coefficient $c_d$, spray cone angle $\theta$ as well the saturated liquid-vapor equilibrium mixture fraction $Z_{sat}$ was referred to the one mentioned in literature at 0.8, 0.86, 23° and 0.34, respectively[68].

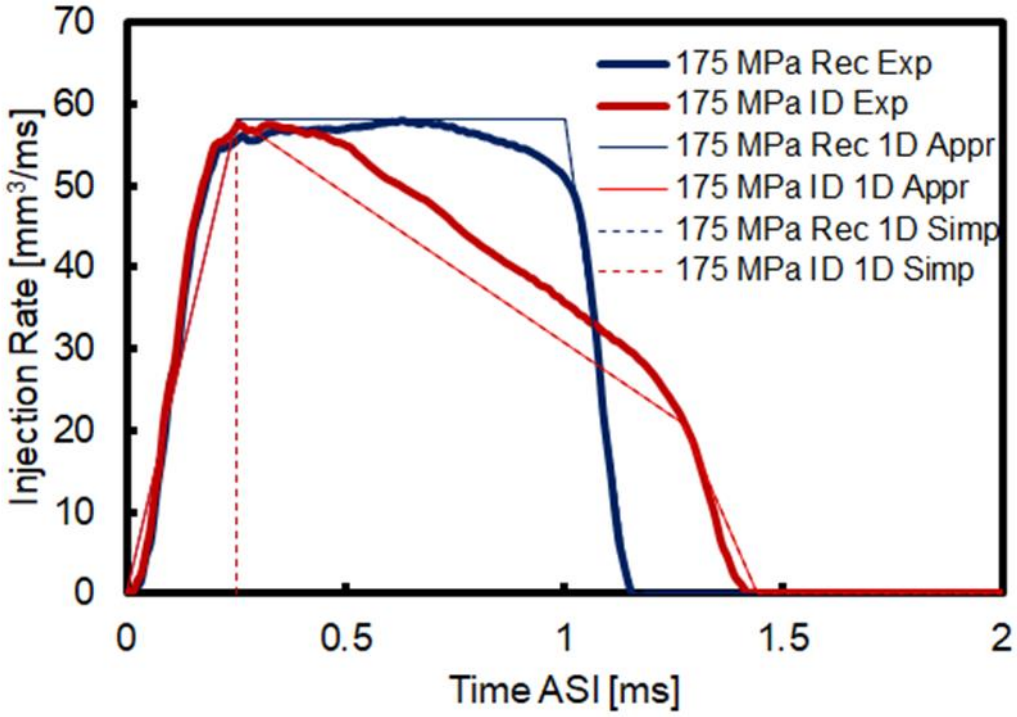


**Figure 26 Injection rate of the experimental (thick line), approximation model (thin line) and simplified model (dotted line) for 175 MPa rectangle and 175 MPa inversed-delta injection.**

In Figure 27, it is observed that the spray tip penetration of rectangle and inversed-delta injection are initially similar and begin to deviate at some point in the experimental data. This trend is well captured in all simulated injection patterns, suggesting that smaller inversed-delta injection spray tip penetration is likely caused by a lack of following jet momentum to push the spray tip further. Note that the timing for the simplified injection pattern is shifted earlier to fit the

experimental results. It is observed that the simplified injection pattern represents the actual spray tip penetration better than the ramp injection pattern, especially in the inversed-delta injection case. For rectangle injection, the downstream penetration is overpredicted probably due to the artefact of different spray combination (i.e. viewing field is limited to 35 mm thus two separate images are combined to represent the whole spray). Apparent bump at around 37.5 mm is indeed noticed suggesting that the actual spray tip penetration might be slightly larger around this axial location. To summarize, the experimental spray tip penetration data match the 1D model of simplified injection pattern adequately, thus it is employed throughout this paper for the equivalence ratio distributions and air entrainment arguments later.

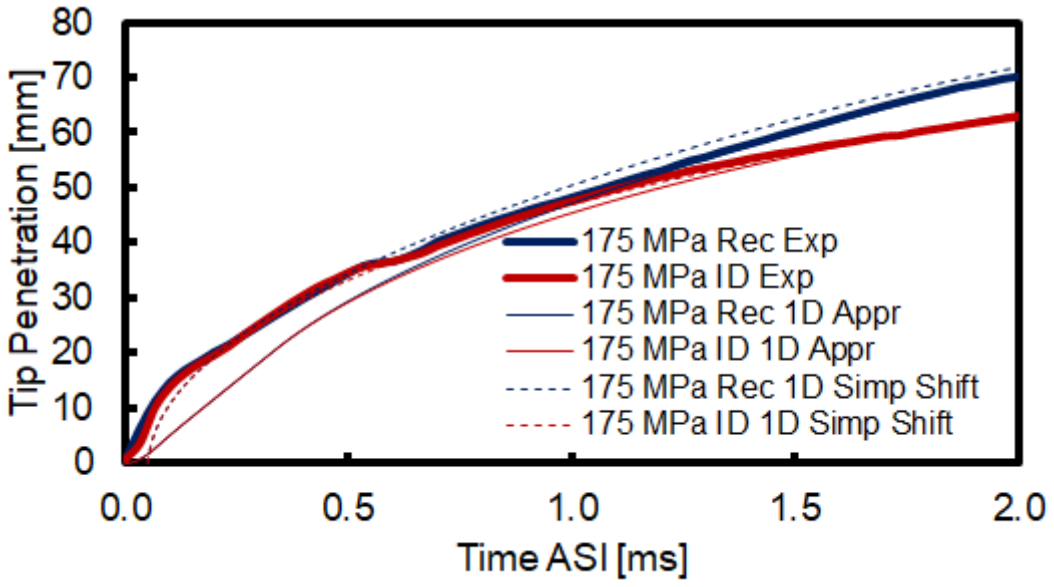


**Figure 27 Tip penetration of the experimental (thick line), approximation model (thin line) and simplified-shifted model (dotted line) for 175 MPa rectangle and 175 MPa inversed-delta injection [Fuel].**

## 2.5 Single Cylinder Engine Test

### 2.5.1 Experimental Setup

Figure 28 and Table 5 show the experimental setup and engine specifications for the engine performance test, respectively. Relatively small engine geometry with bore and stroke respectively at 85 mm and 96.9 mm was used since the focus of this study is on the passenger vehicle Diesel engine. The engine setup includes external supercharger, intercooler, low-pressure EGR system, swirl control valve equipped with multiple sensors for intake pressure, intake temperature, EGR ratio, back

pressure and swirl ratio measurement. A common rail fuel injection system with up to 200 MPa rail pressure and fully controllable injection timing and duration was used. TAIZAC injector equipped with φ0.101 mm × 10 multi-hole nozzle was used for the performance test, injecting Japanese commercial JIS#2 diesel fuel. Piston shape was low-swirl type with cavity outer diameter of φ70 mm and lip inner diameter of φ55.4 mm.

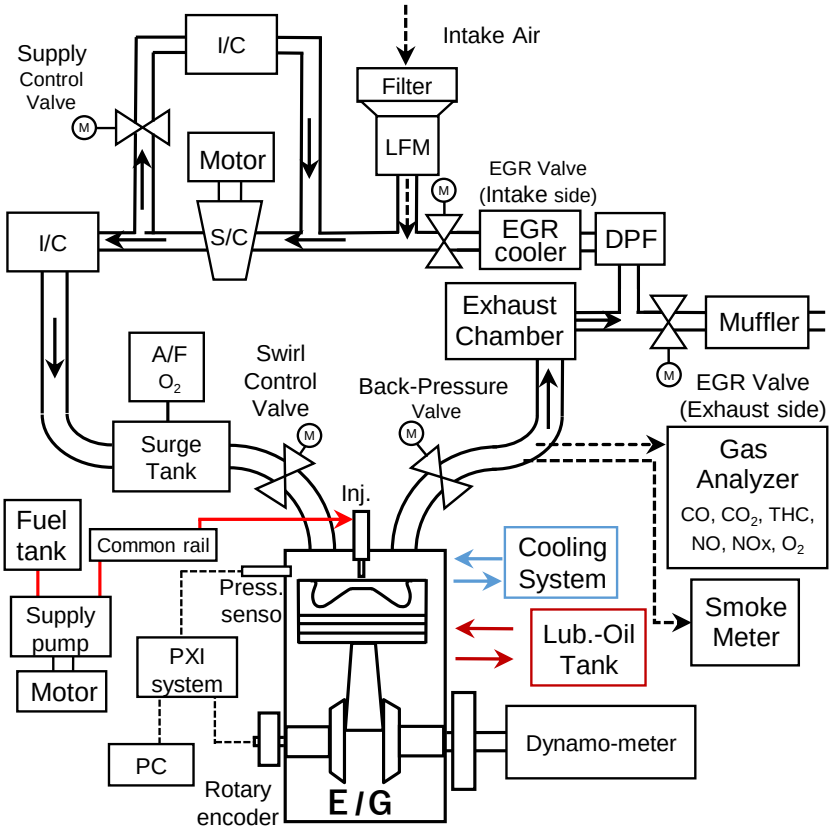


**Figure 28 Experimental setup for engine performance test using TAIZAC injector**[76].

**Table 5 Engine specifications**

| | |
|---|---|
| Engine type | Water-cooled single cylinder direct-injection Diesel engine |
| Bore × stroke [mm] | 85 × 96.9 |
| Displacement [$cm^3$] | 550 |
| Compression ratio | 16.3 |
| Injection system | Common-rail system<br>φ0.1 mm × 10 holes at 200 MPa max. |
| Supercharging | External supercharging |
| Combustion chamber | Low swirl type |

Fuel flow rate was measured with a precision low-flow fuel flowmeter (Model213, MAX Machinery). Cylinder pressure for combustion analysis was measured with a piezo pressure transducer 6052C, KISTLER. Gaseous emissions and smoke were measured with a gas analyzer MEXA1700-DEGR, Horiba and a smoke meter GSM-22A, Tsukasa Sokken, respectively.

As for the heat balance analysis, indicated work was calculated from measured cylinder pressure. Exhaust loss was calculated from enthalpy difference between intake and exhaust gases based on measured emission composition and temperature. Unburnt loss was calculated from measured emission composition. The other loss including cooling loss was obtained by subtracting the indicated work, the exhaust loss, the and unburnt loss from the fuel energy supplied.

### 2.5.2 Experimental Conditions

Table 6 and Figure 29 show experimental & injection conditions and injection rate profiles by using TAIZAC injector, respectively. Triple injection strategy of pilot, pre and main injection was employed. Amount and start timing of each injection were set constant at 1.3, 1.4, 36.3 mg/cycle at -20.5, -9.5, -2.0 deg ATDC, respectively totaling at 39 mg injection amount per cycle, representing a high load condition for the tested engine without EGR application for simpler results interpretation. Note that both injection rate shaping profiles were performed by the same TAIZAC injector to decouple several injector-characteristics-parameter effects (i.e. initial injection rise rate, pilot and pre injections rate, needle actuation response and cavitation constant) with the inversed-delta injection rate shaping effects.

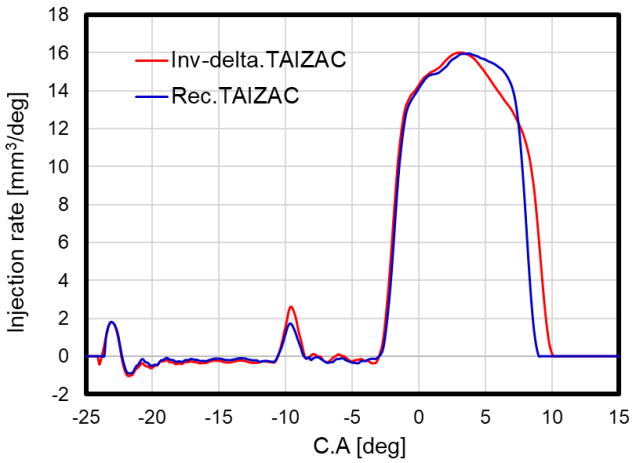


**Figure 29 Measured and tested injection rate shaping profiles using TAIZAC injector**[95].

Table 6 Experimental and injection conditions.

| Experimental conditions | |
|---|---|
| Engine speed [rpm] | 2250 |
| Intake-air temperature [℃] | 50 |
| Intake air-pressure [kPa] | 180 |
| Swirl ratio [-] | 1.3 |
| EGR Ratio [%] | 0 |
| Injection conditions | |
| Injector | TAIZAC |
| Common-rail pressure [MPa] | 200 |
| Sac pressure [MPa] | 185 |
| Injection strategy | Pilot, pre, main |
| Injection pressure [MPa] | 185, 185, 185 |
| Injection amount [mg] | 1.0, 1.0, 37.0 |
| Injection timing [deg. ATDC] | -21.5, -9.5, -2 |
| Fuel | JIS#2 |

### 2.6 Summary

A short conclusion for this chapter can be summarized as follows:

1. Inversed-delta injection rate shaping is successfully realized by TAIZAC injector It is a relatively low cost and robust device since it is consisted of two directly-connected commercial injectors.
2. Single spray is extracted from the multi orifice commercial nozzle by drilling additional axial orifice hole and attaching a nozzle cap: its injection rate and mass can be measured from the spray momentum. Shorter impingement distance and medium ambient density setup yield results with higher accuracy.
3. Simple one-dimensional model is employed to study the air entrainment and spatial mixture distributions of inversed-delta injection spray. The spray tip penetration of the rectangle and inversed-delta injection matched-well with the simulation results, suggesting a fair validity of the model.

# 3 EFFECTS ON DIESEL SPRAY FLAME

Results of non-impinging Diesel spray flame under CVCC experiments are presented and discussed in this chapter. Firstly, simultaneous high-speed UV imaging of Diesel spray flame is acquired to grasp an overall picture, particularly during the late combustion in the inversed-delta injection case. Then, impacts of the inversed-delta injection on combustion duration from apparent heat release rate AHRR profile will be investigated. Further details regarding inversed-delta injection spray characteristics regarding air entrainment is examined from liquid length, lift-off length and soot onset, as well as 1D simulation. Literatures on transient spray air entrainment and inversed-delta conceptual diagram are revisited.

## 3.1 Simultaneous High-speed Imaging

### 3.1.1 Injection Conditions

Injection rate shaping profiles obtained with Bosch-type long tube method from multi orifices injector is presented in Figure 30. Table 7 shows the injection conditions where the total relative momentum of the injected fuel was derived from the injection rate and the actual injection duration was confirmed with high-speed DBI method at 100,000 fps in atmospheric condition. Note that this injection profiles were limited from a TAIZAC injector for the study in this subchapter, where different TAIZAC injector and injection characteristics may be applied for the study performed in other sections.

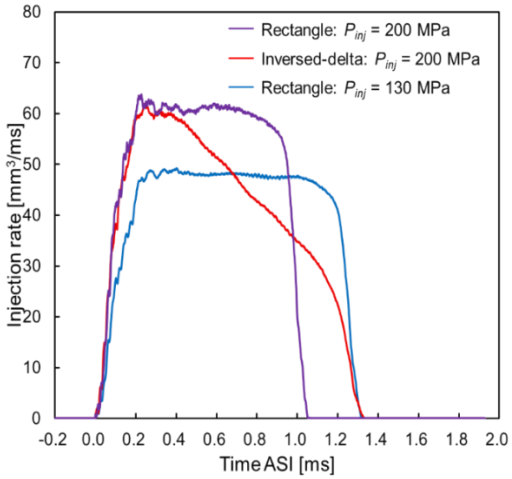


**Figure 30 Injection rate profiles obtained by Bosch long-tube method. Injection conditions: φ0.12 mm × 8+1 and $m_f$=45 mg**[77].

Table 7 Injection conditions for inversed-delta and rectangle injection rate shaping.

| Injection profile | Pressure (MPa) | Rate shaping | Duration (ms) | Relative momentum |
|---|---|---|---|---|
| 200 MPa rectangle | 200 | Rectangle | 1.06 | 1.20 |
| 130 MPa Rectangle | 130 | Rectangle | 1.32 | 0.95 |
| 200 MPa inversed-delta | 200 to 100 | Inversed-delta | 1.34 | 1.00 |

Due to the limit of the common rail pressure system and 45 mg injection amount representing the high-load operating condition, JIS#2 Diesel fuel was injected at 200 MPa initial pressure and dropped down to approximately 100 MPa within 1.34 ms for 200 MPa inversed-delta injection condition. Similar injection amount and duration can be achieved for conventional rectangle injection injected at 130 MPa. Since typically faster combustion duration can be achieved by utilizing even higher injection pressure, it is necessary to compare a relatively complex inversed-delta injection over a simpler high-pressure rectangle injection at 200 MPa within 1.06 ms.

### 3.1.2 Inversed-delta and Rectangle Injection Diesel Spray Flame Comparison

For qualitative comparisons, example of simultaneous high-speed images of 200 MPa rectangle, 130 MPa rectangle and 200 MPa inversed-delta are shown in Figure 31 where left, middle and right image column for each injection profile show the soot luminosity, UV emissions at 310 nm and UV DBI at 266 nm, respectively[77]. The timing after the start of injection (ASI) depicted at the top left corner of each spray and the axial distance from the nozzle tip can be referred at the bottom of each column. A whole diesel spray image is mimic using combination of three separated injections taken at what we called upstream, midstream and downstream region.

Period from 0.43 ms to 2.57 ms show the main combustion period where during this time frame, strong thermal radiation from soot impedes heat release observation from UV chemiluminescence. Similarly, shadow from soot particles also interfere with fuel-gas mixture UV absorption observation. However, inspection of the heat release and mixture concentrations can be performed after the soot was oxidized and disappeared at 3.43 ms for 200 MPa rectangle and 200 MPa inversed-delta injection and at 4.14 ms for 130 MPa rectangle injection.

Except from large spray tip penetration in 200 MPa rectangle injection, the diesel spray flame shape and qualitative shadow optical thickness seems to be similar at 1.00 ms and 1.86 ms ASI timing. It is noted that at 2.57 ms, higher presence of the soot luminosity, UV emissions and UV DBI are detected at the upstream region in

200 MPa inversed-delta injection compared to rectangle injection profiles, suggesting that the fuel-air mixture was distributed more evenly. Starting from 5.00 ms ASI in UV DBI shadow images, it can be observed that the spray tip rich mixture is relatively "thinner" or "softened" in 200 MPa inversed-delta compared to the rectangle injections. The spray tip rich mixture in 130 MPa rectangle persist even at 9.57 ms, while in 200 MPa inversed-delta, the spray tip is softened and disappeared much earlier. It was also interestingly observed that the disappearance timing of soot luminosity, UV chemiluminescence and UV DBI was faster in 200 MPa inversed-delta compared to 130 MPa rectangle injection although their injection duration is identical. In 200 MPa rectangle injection, the spray penetrates much further than the viewing field limit at 117.5 mm, making it difficult to compare its disappearance timing with other injection profiles. The spray tip penetration is highest in 200 MPa rectangle injection while almost similar value is observed for 200 MPa inversed-delta and 130 MPa rectangle injection. Details on the tip penetration quantitative analysis and cooling loss affects will be discussed in the next section.

As discussed in earlier section, diesel spray penetrates faster in reacting condition due to low local density induced by high temperature region where the following spray catch-up easily with the previous spray: it is then either being push-away to lateral side or super-imposed with the following spray, forming the spray tip rich mixture[60], [96]. From the high-speed imaging results, it can be suggested that the spray tip rich mixture is suppressed due to less catch-up expected by reducing following spray momentum gradually as in the inversed-delta injection rate shaping case. It is interestingly noted that the spray seems to be distributed nearer to nozzle vicinity resulting in more even spray. It is of concern that low injection momentum of the following spray might be poorly atomized and mixed that will lead to poor combustion duration and high soot emissions. However, relatively fast UV chemiluminescence and combustible-mixture UV shadow disappearance as well as comparable flame luminosity observed from the high-speed images indicate that the inversed-delta rate-shaping strategy might be effective in reducing combustion duration without significant trade-off with soot production.

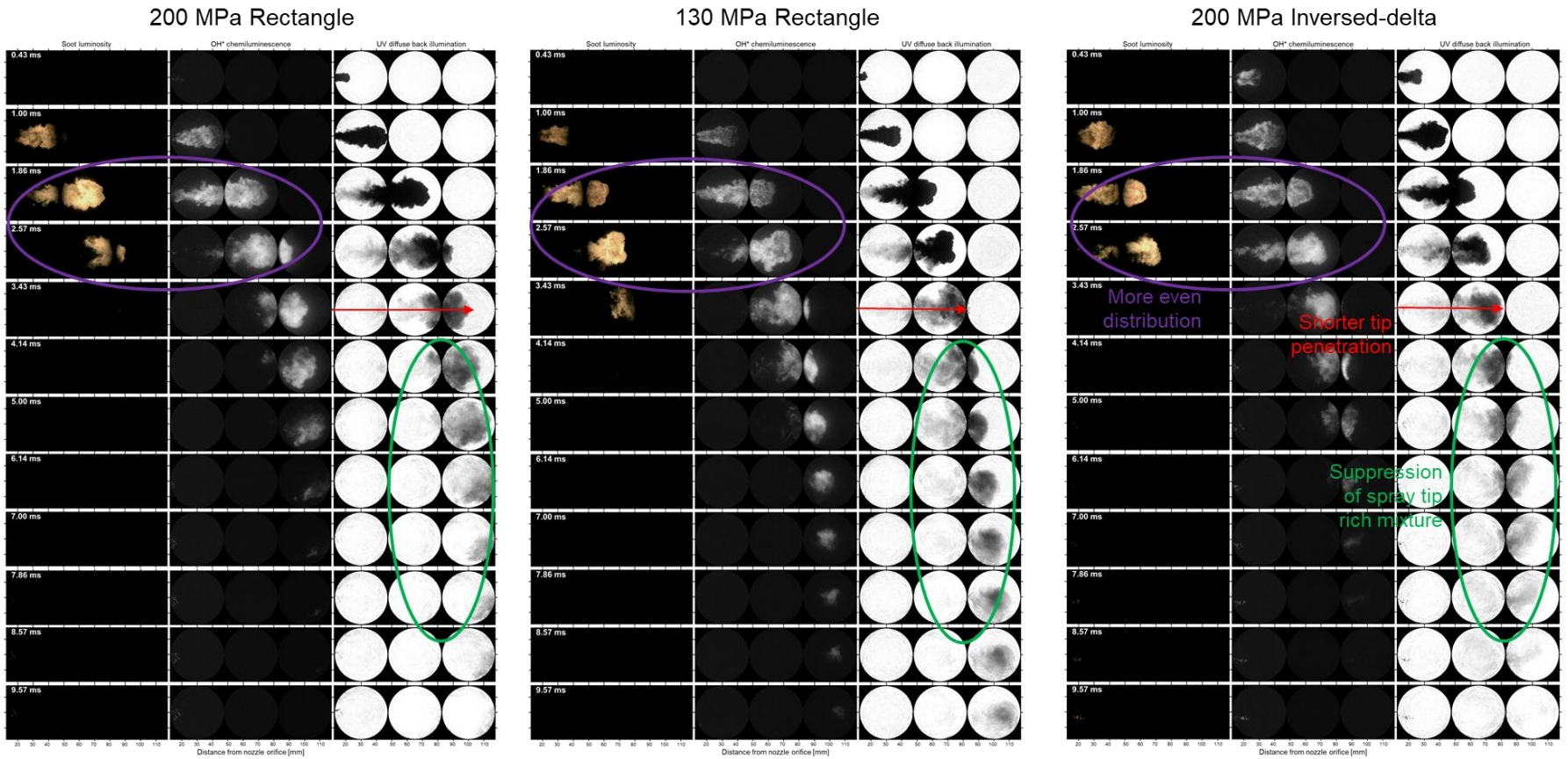


Figure 31 Example of high-speed images for 200 MPa Rectangle (left), 130 MPa Rectangle (middle) and 200 MPa Inverse-delta (right) diesel spray flames: each left, middle and right column correspond to soot luminosity, UV emissions and UV absorption. Ambient conditions: $\rho_g$=23.8 kg/m$^3$, Pa=5.4 MPa, $T_a$=1050 K and 17% $O_2$. Injection conditions: φ0.12 mm orifice and $m_f$=3.4mg.

### 3.1.3 Apparent Heat Release Rate AHRR

Figure 32 shows apparent heat release rate AHRR ensemble average of 10 shots from varieties of spacer setup. Star markers at the graph bottom indicate the ignition delay timing while triangle markers indicate the timing of the end of combustion defined here at approximately 3 J/ms.

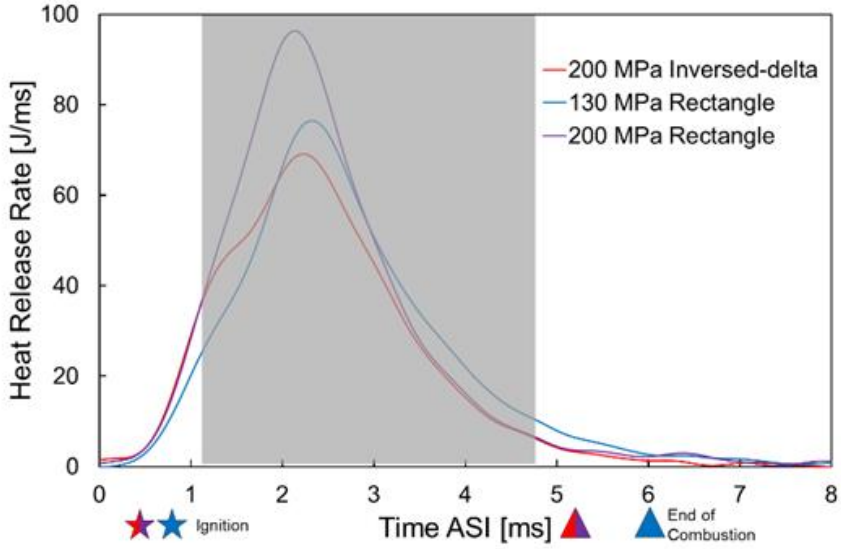


**Figure 32 Pressure-derived apparent heat release rate. Star and triangle markers indicate the timing of ignition and end of combustion, respectively. Data interpretation of area covered with a grey-shaded region will be omitted. Ambient conditions: $\rho_g$=23.8 kg/m$^3$, $P_a$=5.4 MPa, $T_a$=1050 K and 17% $O_2$. Injection conditions: φ0.12 mm orifice and $m_f$=3.4mg**[77].

AHRR acquired in this study needs to be treated with caution because the total heat amount (i.e. integration of area below the graph curve) appeared to be approximately 20% larger in 200 MPa rectangle injection compared to 200 MPa inversed-delta and 130 MPa rectangle injection although their injection amount is similar. It was suspected that the fuel injected from other radial orifices is impeding the heat release analysis from a single axial spray flame extracted due to the fact that the total heat amount calculated is higher than the injected diesel fuel theoretical calorific value, especially in 200 MPa rectangle injection condition. In addition, systematic trend of higher total heat amount in higher injection momentum is also noticed. Fortunately, this interference seems to be more apparent in the diffusion combustion phase, where the late combustion phase seems to be less affected. Thus, for the sake of better argument from the acquired AHRR graph, area covered by a grey-shaded region will be omitted from the discussion.

The trend of combustion duration reduction from heat release rate matched well with the disappearance timing of UV emissions in high-speed images shown in Figure 31. The heat release was shifted earlier and ended faster in 200 MPa inversed-delta compared to 130 MPa rectangle injection regardless of their constant injection duration. Injection duration for 200 MPa inversed-delta was approximately 20% longer than 200 MPa rectangle spray. But from the heat release rate graph and qualitative images comparison, timing for the spray tip rich mixture extinction seems to be similar, indicating faster combustion duration to the injection period ratio in the inversed-delta injection case. Comparable initial heat release rise and ignition delay for 200 MPa inversed-delta and 200 MPa rectangle injection suggesting that the mixing and ignition characteristics of the inversed-delta injection might be governed by its initial injection pressure.

### 3.1.4 Spray Tip Penetration Investigation

From Figure 31, it can be observed that spray tip penetration in 200 MPa rectangle case was the longest probably due to its highest total injection momentum as shown in Table 7. It is interesting to note that the spray tip penetration in 200 MPa inversed-delta injection was slightly shorter than that of 130 MPa rectangle injection although its total injection momentum is slightly higher, suggesting that other factor than momentum supply might govern the tip penetration presented here. For example, Johari and Paduano speculated that during decelerating period, ambient fluid entrainment increased to compensate the decreasing jet axial flow: slower penetration might be caused by air entrainment enhancement since its direction is perpendicular to the injection jet axis[97]. Further study on effects of inversed-delta injection on spray tip penetration was of interest since its shorter penetration indicates weaker impingement force on the chamber wall, potentially able to reduce cooling loss in the actual Diesel engine combustion, although it should be noted that the tip penetration difference was more pronounced at approximately 50 mm from the nozzle tip, larger than passenger vehicle Diesel engine cylinder radius.

Desantes et. al explained that the reacting Diesel spray tip penetration differ than the non-vaporizing or non-reacting spray by sudden expansion and deceleration during auto ignition event, and then accelerate at faster velocity, probably due to low density owing to high-temperature reaction[28]. However, notable findings regarding Diesel spray jet characteristics such as the one reported by Wakuri, Arai and Siebers were all conducted under relatively simple non-vaporizing conditions experiments[14], [22], [60] since the inert ambient gas charged into the combustion

vessel was able to simulate similar ambient density to that of the reacting conditions. Thus, in the present study, the spray tip penetration was attempted via high-speed Diffused Back Illumination DBI technique under non-vaporizing conditions with $CO_2$-charged-CVCC at 1.6 MPa to simulate 23.8 kg/m$^3$ ambient density.

Figure 33 shows optical setup for the spray tip penetration high-speed imaging[98]. White background light from mercury lamp was diffused before entering the vessel and the high-speed images were acquired at 30,000 fps with 4 µs shuttering gate by using a NAC MEMRECAM HX-5 high-speed camera equipped with Nikkor 105mm f2.8 lens. Acquired images were preprocessed to enhance its contrast by dividing the image of each time step $N_{th}$ with the background image $N_0$. Average signal value from 80 x 4 pixel size area (a pixel equivalents to 0.0875 mm) was calculated along the spray axis and 10% threshold level was applied to determine the spray tip penetration.

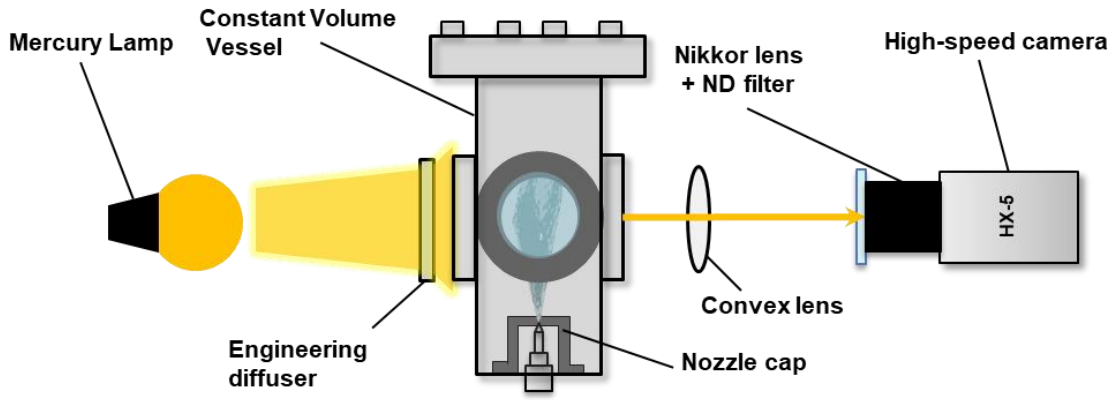


**Figure 33 Experimental setup for free-spray high-speed diffused back illumination DBI**[98].

Injection rate shaping profiles obtained with Bosch-type long tube method from multi-orifices injector is presented in Figure 34. Table 8 shows the injection conditions where the total relative momentum of the injected fuel was derived from the total injection rate and the actual injection duration was confirmed with high-speed laser DBI at 100,000 fps in atmospheric condition.

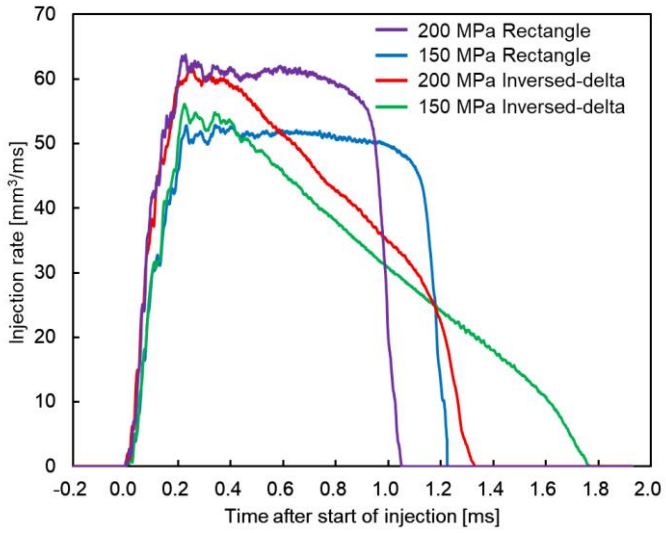


**Figure 34 Injection rate obtained by Bosch long-tube method**[98].

**Table 8 Injection conditions.**

| **Profile** | **Pressure [MPa]** | **Shaping** | **Duration [ms]** | **Momentum [kgms$^{-1}$]** |
|---|---|---|---|---|
| 200 MPa rectangle | 200 | Rectangle | 1.06 | 0.001964 |
| 150 MPa rectangle | 150 | Rectangle | 1.32 | 0.001660 |
| 200 MPa inversed-delta | 200-100 | Inversed-delta | 1.34 | 0.001630 |
| 150 MPa inversed-delta | 150-10 | Inversed-delta | 1.77 | 0.001337 |

Figure 35 shows the quantitative spray tip penetration extracted from the DBI images. The spray tip penetration value was obtained by combining the ensemble average of 3 shots from three different axial location, namely upstream, midstream and downstream region. The total viewing field is from 2.5 mm to 117.5 mm and bumps observed at around 37.5 mm and 72.5 mm axial distance from the nozzle orifice were caused by different regions assembling artefact. The injection amount for each injection profiles were fixed at 3.4 mg and the respective injection durations are shown in Table 8. Increase of injection pressure will increase the injected fuel momentum exponentially, thus the tip penetration increases as the injection pressure was increased in both rectangle and inversed-delta injection rate shaping

profile[14]. By comparing the similar initial injection pressure conditions, it is observed that the spray tip seems to be traveled at similar level initially before diverging out. As discussed previously, it is expected that the following spray has lower momentum to push the spray tip penetration further in the inversed-delta injection. It is interesting to note that the spray tip penetration of 200 MPa inversed-delta progress faster initially but it seems to be slowed down to which it is being surpassed by 150 MPa rectangle injection. As exposed in Table 8, the spray total momentum of 200 MPa inversed-delta and 150 MPa rectangle injection was almost similar. From the momentum view alone, the spray tip penetration of both cases should be comparable however, it was clearly observed that the spray tip penetration of 150 MPa rectangle was larger than that of 200 MPa inversed-delta, starting from a diverging point and the difference becomes larger as it travels further downstream. It is also noted that the spray penetration curve is similar for the same injection profile even at different injection pressure.

The Wakuri's penetration equation based on the spray momentum conservation is valid for the spray penetration behavior during quasi-steady injection event[14]. Arai et al observed that just after the end of injection, the spray tip penetration seems to follow the Wakuri's equation to the timing where the transient spray affects the spray tip, mentioned as stagnating effects[62]. Furthermore, Musculus et al. expected that the end of injection event upstream will affects the tip penetration downstream at roughly half the injection duration after the EOI, likely due to the entrainment wave arrival since it is travelling downstream at twice the spray penetration velocity [34]. Figure 36 shows the spray tip penetration during the relatively steady period where the stagnating effects is absences. Hiroyasu and Arai Diesel penetration equation were plotted into the graph as the solid black lines. Noted that this equation is only valid for rectangle injection case since it is derived from momentum conservation theory specifically in the quasi-steady injection scenario.

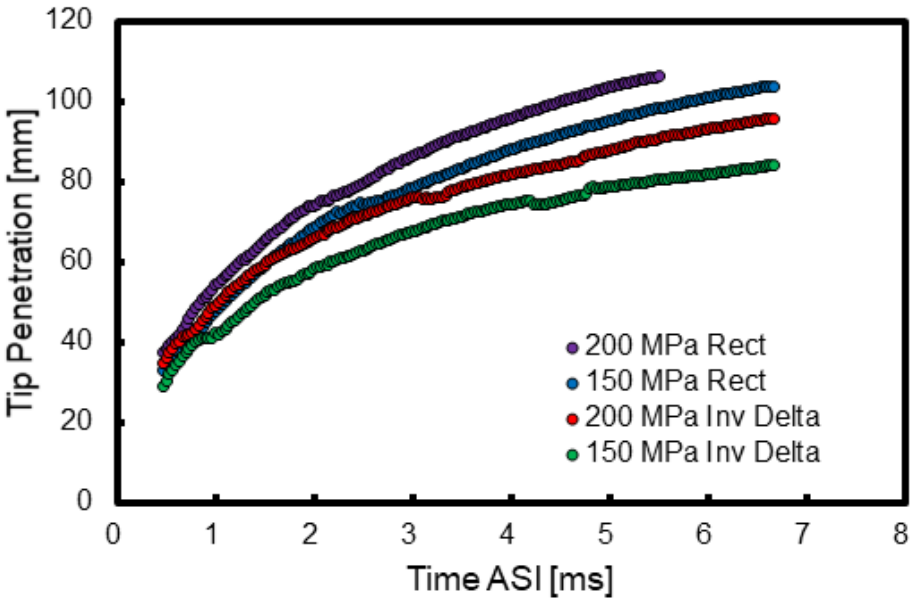


Figure 35 Quantitative analysis of spray tip penetration in non-vaporizing condition. Ambient conditions: $\rho_g$=23.8 kg/m$^3$, $P_a$=1.6 MPa, $T_a$=373 K and 100% $CO_2$. Injection conditions: φ0.12 mm orifice and $m_f$=3.4 mg[98].

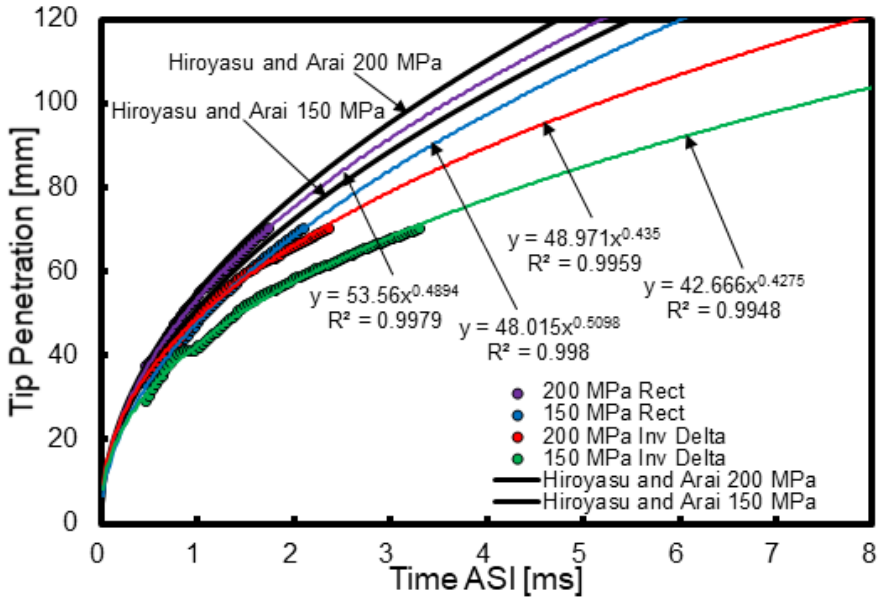


Figure 36 Quantitative analysis of spray tip penetration in non-vaporizing condition before stagnating effects with Hiroyasu and Arai equation fitting[99]. Ambient conditions: : $\rho_g$=23.8 kg/m$^3$, $P_a$=1.6 MPa, $T_a$=373 K and 100% $CO_2$. Injection conditions: φ0.12 mm orifice and $m_f$=3.4 mg[98].

It can be observed that even in a non-typical injector was used in the present study, the tip penetration data obtained fit fairly well with the Hiroyasu and Arai equation, with only a slight overestimation likely due to the flow coefficient value difference. The spray tip penetration in the rectangle cases are proportional to $t^{0.5}$ as frequently reported in the literature[14], [22], [58]. However, it is interesting to note that both 200 MPa and 150 MPa inversed-delta spray tip penetration are proportional to approximately $t^{0.43}$ value. Several reasons can be listed as follow. (1) The spray momentum supply is progressively reduced in the inversed-delta injection thus there should be less momentum available at the spray head to push it forward: the exponential value seems to be dictated by the inversed-delta injection ramp down rate. (2) It is speculated that increased of air entrainment in transient ramp-down profile as in inversed-delta injection might accelerate air entrainment, promoting fuel-air momentum exchange and slowing the tip penetration down further. From the spray tip penetration results obtained, it can be expected that the inversed-delta injection might not only improve combustion duration, but might also be effective in reducing the cooling loss, which are both beneficial for the Diesel engine thermal efficiency improvement.

## 3.2 Impacts on Combustion Duration

### 3.2.1 Experimental Setup and Conditions

Injection rate shaping profiles from 10 shots ensemble average obtained with a Bosch-type long tube method from multi orifices injector is presented in Figure 37. Table 9 shows the injection conditions where the actual injection duration was derived from high-speed laser DBI imaging at 100,000 fps at atmospheric conditions. Relatively high injection mass was selected at 45 mg for all injection profiles corresponding to high-load operation and axial spray injection mass was weighted at approximately 5 mg in all injection profiles for this present experiment.

As shown in Figure 37, although the common-rail pressure was set 25 MPa lower in rectangle injections compared to that of inversed-delta injections, identical initial injection rate and peak are observed. This is due to spilling of accumulated fuel at lower injector through leak tube necessary to enable the DENSO G4S injector needle lift movement, results in lower actual hydraulic pressure compared to the common rail pressure. Hence, the injection pressure presented in this section afterwards is referring to the nozzle inner sac pressure instead of the common rail pressure.

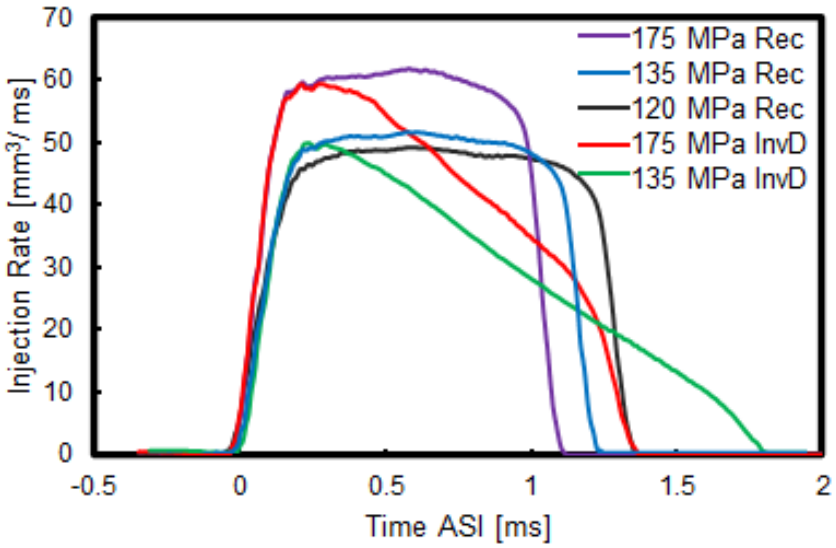


**Figure 37 Injection rate profiles measured using the Bosch-type long-tube method. Injection conditions: φ0.12 mm × 8 +1 additional axial orifice and $m_f$=45 mg.**

**Table 9 Injection rate shaping profiles using TAIZAC injector.**

| Injection Profile | $t_{inj}$ [ms] | Rail ΔP [MPa] | $\Delta P_{inj}$ [ms] |
|---|---|---|---|
| 175 MPa Rectangle | 1.16 | 175 | 175 |
| 135 MPa Rectangle | 1.31 | 135 | 135 |
| 120 MPa Rectangle | 1.41 | 120 | 120 |
| 175 MPa Inversed-delta | 1.41 | 200 | 175 to approx. 50 |
| 135 MPa Inversed-delta | 1.92 | 135 | 135 to approx. 0 |

Due to the limit of common rail system pressure at 200 MPa, fuel was injected at 175 MPa initial sac pressure and dropped down to approximately 50 MPa within 1.41 ms as in 175 MPa inversed-delta injection profile while similar injection amount and duration can be achieved for rectangle injection at 120 MPa injection pressure. 175 MPa rectangle injection represents the injector full potential in terms of injection period and fair comparison to 175 MPa inversed-delta injection initial injection rate. Lastly, the effects of EOI inversed-delta pressure reduction on the late combustion and combustion duration was examined from 135 MPa inversed-delta and 135 MPa rectangle injection profile. Note that although significant following spray pressure reduction (to near-zero) might shift fuel-gas mixture distribution nearer to injector vicinity and suppress the spray tip rich mixture formation, trade-off with poor fuel atomization and significantly long injection period cannot be neglected.

Simultaneous high-speed images of 310 nm UV emissions, 266 nm UV DBI and direct soot luminosity photographs as mentioned in the previous section, were again examined to observe the heat release location and fuel-gas mixture distributions as shown in schematic diagram in Figure 38[100]. The high-speed imaging technique applied in this study is closely similar to that of the previous experiment, except for the UV light source employed[77]. For UV DBI image acquisition in this study, a pulsed UV-LED developed by NAC Image Technology Inc. Japan was used as the light source. This LED system was equipped with a quad UV-LED chip (DUV-LED VPS131, Nikkiso) in 50 mm diameter and average power is 12mW/element, spectrum centered about 265 nm with a 13 nm bandwidth. Nine identical diodes were aligned in a 3 x 3 matrix, capable of emitting approximately 160 mW in total. Short-pulse LED system generates burst light to provide sufficient signal than that of soot UV radiation, at a relatively high-repetition rate of 7,000 Hz. The emitted light was diffused before being collimated with a planoconvex lens. This LED system was relatively cheaper, lightweight, easy to operate and less shot-by-shot fluctuation than that of UV-laser. Furthermore, LED elements can be easily exchanged or mixed with another wavelength for any marker targeted.

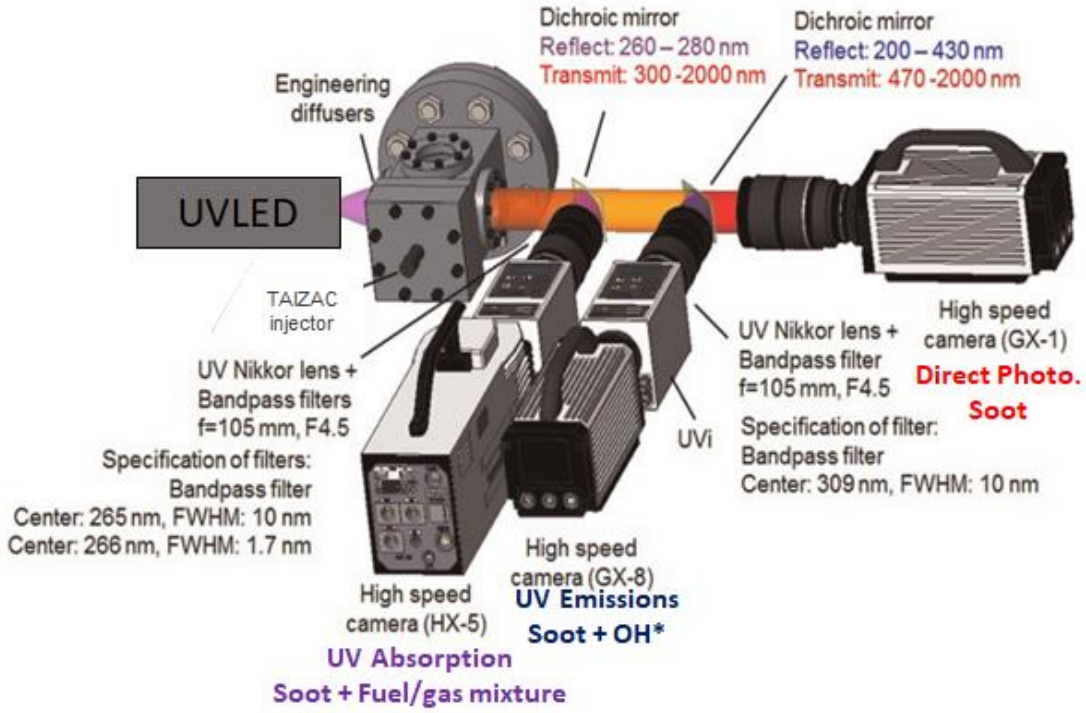


**Figure 38 Setup of Diesel spray flame simultaneous imaging with UVLED as light source**[100].

### 3.2.2 Simultaneous High-speed UV Imaging Results with UVLED Background

Figure 39 shows five shots representative time sequences images of 175 MPa inversed-delta injection, 175 MPa rectangle injection and 120 MPa rectangle injection respectively at the top, mid and bottom row, displaying similarly to results in the previous section except false color scheme was applied to the UV LED DBI and UV emissions images were preprocessed for clarity

Similar to the previous section, thinner spray tip rich mixture optical density, more even UV emissions spatial distributions and shorter spray tip penetration characteristics are noted in the inversed-delta injection compared to that of the rectangle injection, although the differences become smaller as the rail pressure in rectangle injection was reduced. From a one-dimensional discrete spray momentum analysis viewpoint, during inversed-delta injection ramp-down period, reduction of fuel pressure decreases the momentum supply to the preceding spray which results in leaner spray tip concentration and also shorter penetration[28], [33].

UV emissions images at 5,71 ms ASI indicated that no noticeable difference on OH* disappearance timing in all cases. It is counterintuitive since at least the combustion duration should be shortened in 175 MPa rectangle injection compare to 120 MPa rectangle injection (i.e. higher injection momentum, shorter injection period injected within similar conventional injection rate shaping). This ss likely due to considerably low UV emissions signal intensity and slow acquisition frame rate, making it difficult to pinpoint the exact combustion duration solely from the high-speed images. Hence, further investigation of combustion duration will be discussed from the AHRR results in the next section.

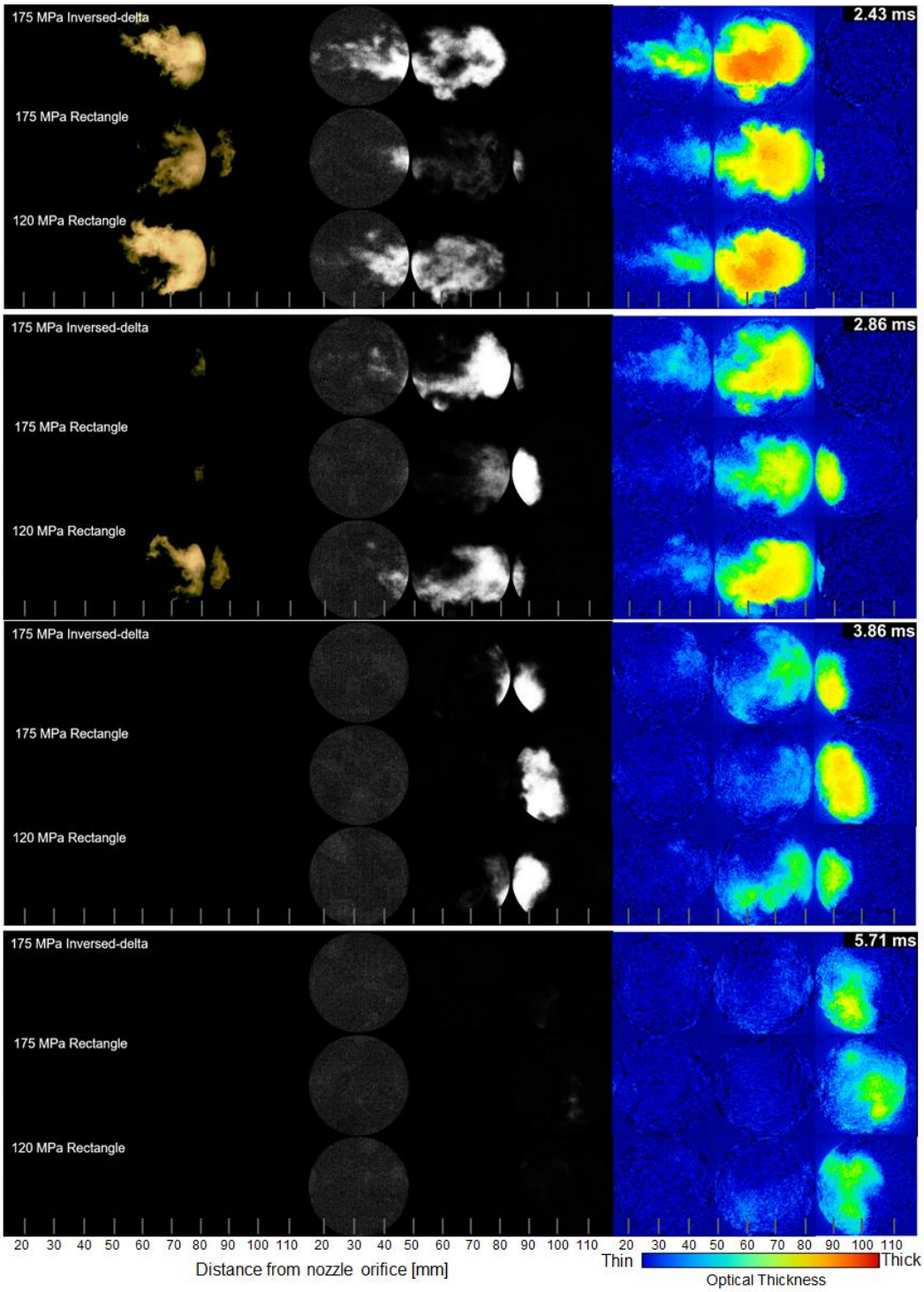


Figure 39 Examples of high-speed images of soot luminosity (left), UV emissions (middle) and UV LED DBI (right) of diesel spray flames corresponding to 175 MPa inversed-delta injection (top), 175 MPa rectangle injection (middle) and 120 MPa rectangle injection (bottom) injection. Ambient conditions: $\rho_g$=23.8 kg/m$^3$, $P_a$=5.0 MPa, $T_a$=1050 K and 17% $O_2$. Injection conditions: φ0.12 mm orifice and $m_f$=5.0 mg[100].

Images comparison between 135 MPa inversed-delta injection and 135 MPa rectangle injection was conducted to investigate the effects of further reduction of injection pressure as shown in Figure 40. The injection amount was set similar to the other injection profiles at 45 mg, while the pressure difference $\Delta P$ was reduced to near-zero and the injection duration was significantly extended.

At 2.57 ms ASI, very strong OH* and soot recessions at viewing field upstream most locations are observed in the inversed-delta injection. The onset location of OH* and soot was overlapping, implying that soot formation probably increases due to less mixing time[19], [68]. It is also noticed that soot luminosity disappeared faster in 135 MPa rectangle injection, but their penetration length seems to be comparable.

The combustion recession result is in good agreement with the work conducted by Knox et al.: the EOI ramp-down slope and pressure are significant in affecting the recession strength[38], [39]. From their 1-D transient gas-jet mixing chemistry model, it was observed that slower ramp-down rate and lower EOI pressure results in over-lean mixture suppression due to less intense EOI air entrainment, enable the combustion to occur nearer the injector vicinity. This strong combustion recession event might be useful in reducing UHC emissions, especially in low-temperature combustion LTC engine.

It is surprising to note that at around 4.00 ms, the optical thickness from UV LED DBI images was significantly thicker and broader in 135 MPa inversed-delta injection compared to than that of 135 MPa rectangle injection. Associated OH* also shows a broader and higher signal intensity in 135 MPa inversed-delta injection, indicating that a considerably high amount of high temperature reaction is still progressing even when the injection event was ended. Although their injection duration substantially differs by approximately 50%, OH* disappearance timing difference was not apparent due to the reasons mentioned in the previous subsection, and details examination will be discussed from AHRR results in the next section.

From the injection momentum viewpoints, if the EOI pressure is reduced to near-zero, intuitively the fuel and combustion species should be distributed much more even, resulting in thinner spray tip rich mixture and shorter spray flame tip penetration. However, soot luminosity in 135 MPa inversed-delta injection persists even at a further downstream location and longer residence time than that of 175 MPa inversed-delta injection probably due to poor soot oxidation on top of its long injection period.

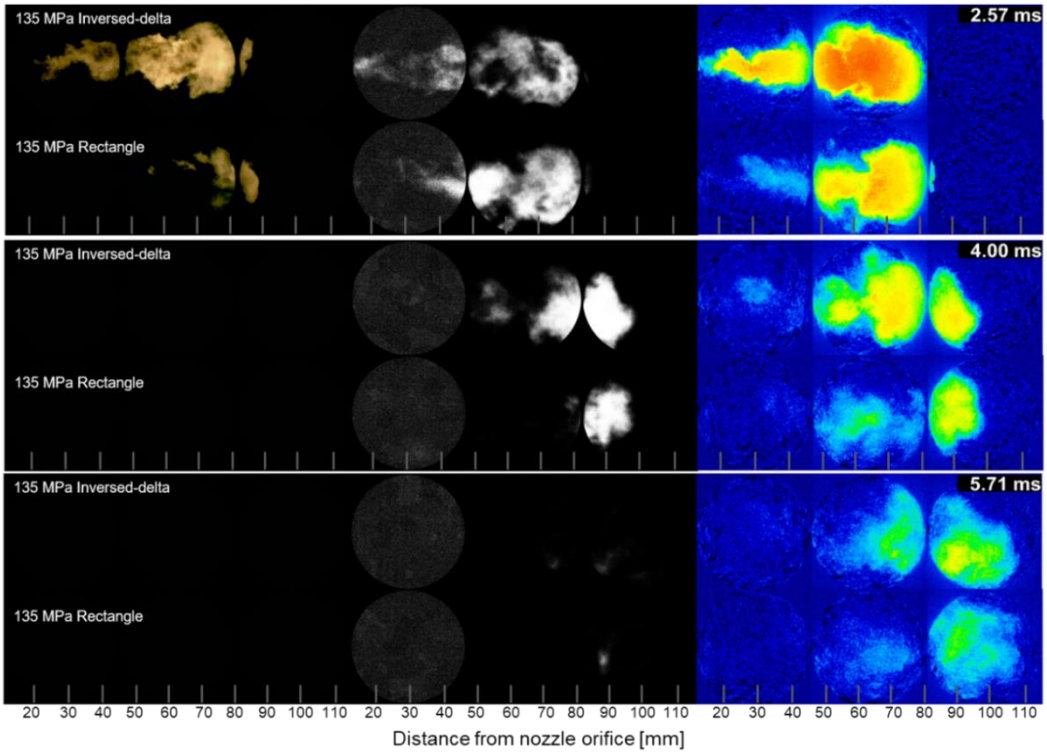


**Figure 40 Examples of high-speed images of soot luminosity (left), UV emissions (middle) and UV LED DBI (right) of diesel spray flames corresponding to 135 MPa inversed-delta injection (top) and 135 MPa rectangle injection (bottom) injection. Ambient conditions: $\rho_g$=23.8 kg/m$^3$, $P_a$=5.0 MPa, $T_a$=1050 K and 17% $O_2$. Injection conditions: φ0.12 mm orifice and $m_f$=5.0 mg**[100].

Direct high-speed images comparison provides insight on the spatial fuel-gas mixture and combustion distributions, but it is difficult to grasp overall flame structure and the corresponding intensity from the time sequence images alone. Thus, spatial-temporal distributions were derived from the UV emissions images by integrating the average signal intensity along the axial spray center for each time step into a single contour chart.

The image processing was conducted with the procedures suggested in the literature[30], [44]. The image processing procedures using ImageJ freeware can be summarized as follows; (1) background subtraction for dark current removal, (2) mean filtering at 4 × 4-pixel for noise extraction, (3) thresholding setting from 30 counts and (4) mean grey value intensity measurement for each pixel along the spray center axis (size at 896 × 896-pixel equivalent to 35 × 35-mm). The image processing procedure was applied to the acquired upstream, midstream and downstream regions with 3 to 5 repetitions each.

Examples of the UV emissions contour map for each repetition and their ensemble average is shown in Figure 41. Images in this figure corresponded to the downstream region (viewing field from 82.5 mm to 117.5 mm axial distance) up to 10.00 ms ASI where the X-axis and the Y-axis represent the spray axial distance and time ASI, respectively. Due to the stochastic nature of diesel combustion, shot-to-shot variation is noticeable, especially at the downstream region. Nevertheless, each image shows that the UV emissions signal intensity is strongly distributed at around 82.5 mm to 92.5 mm in every run which correlated well with the location of the spray tip rich mixture, suggesting that this image analysis method was adequate and convenient to represent the Diesel spray high temperature reaction temporal and spatial distributions.

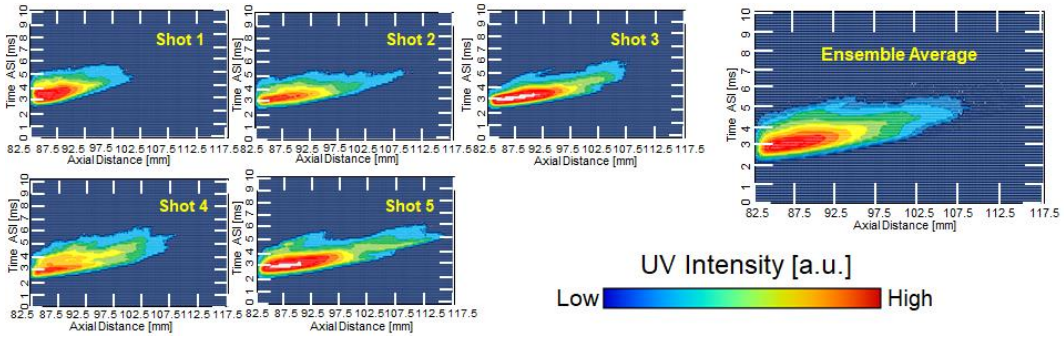


**Figure 41 Shot-by-shot variations and ensemble average (right) of axially integrated UV emissions spatial-temporal distribution of 175 MPa rectangle injection from 82.5 mm to 117.5 mm axial distance from the nozzle tip**[100].

Figure 42 shows the UV intensity contour map of 175, 135 and 120 MPa rectangle injection profiles at three rows from the top while 175 and 135 MPa inversed-delta injection profiles at two rows from the bottom. Note that some peculiar discontinuation at approximately 47.5 mm and 82.5 mm are caused by different spray flame combination and also due to the small axial viewing area at the optical window circular edge. Due to weak UV signal intensity and noisy background during the median filtering procedure, some patchy region artefact is observed particularly in 135 MPa inversed-delta case up to 30.0 mm. At upstream region for all injection profile, relatively high signal intensity is captured at around the EOI timing corresponding to the combustion recession event. These results matche with the high spray flame temperature measured just after the injection was ended, likely due to higher EOI air entrainment that leads to higher combustion temperature[33], [73].

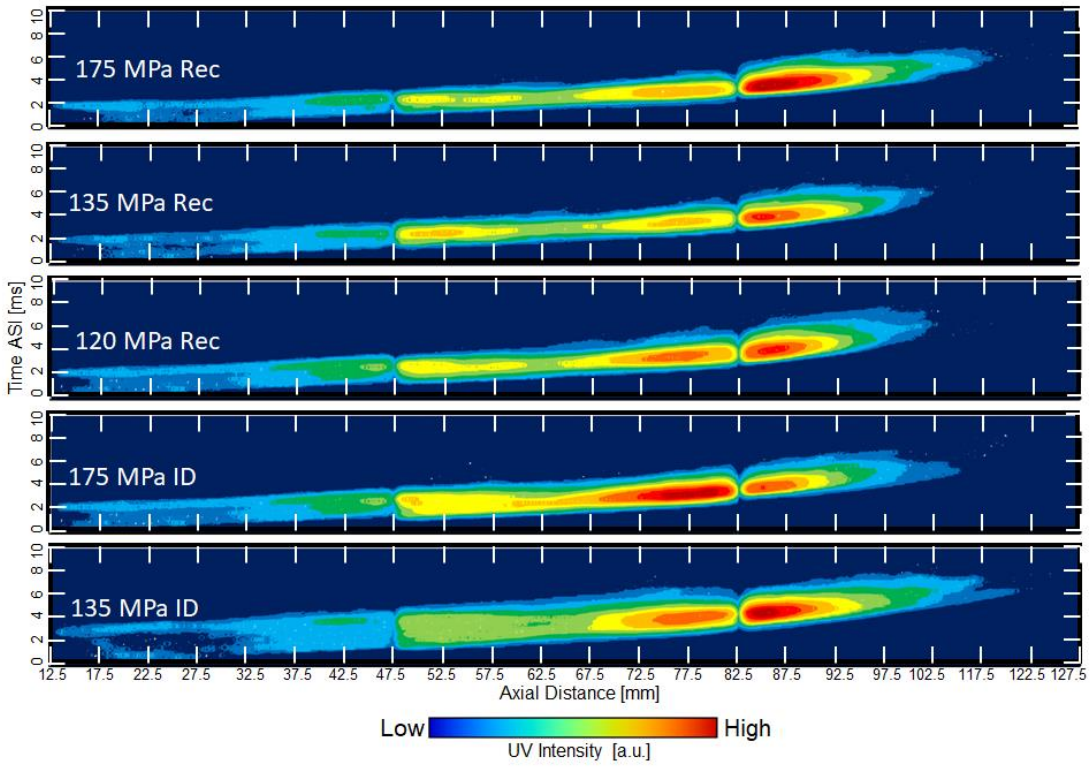


**Figure 42 Ensemble average of axially integrated UV emissions spatial-temporal distribution from 12.5 mm to 117.5 mm starting from 0.0 to 10.0 ms ASI. Ambient conditions: $\rho_g$=23.8 kg/m$^3$, $P_a$=5.0 MPa, $T_a$=1050 K and 17% $O_2$. Injection conditions: φ0.12 mm orifice and $m_f$=5.0 mg**[100].

Strong signal intensity is observed at the spray tip around 80 mm to 90 mm region for all rectangle injection cases where the intensity strength seems proportional with the injection pressure, indicating high combustion activity from the spray tip rich mixture. On the contrary, in 175 MPa inversed-delta injection profile, the location of this peak intensity seems to be shifted upstream and distributed more evenly along the spray axis, resulting in more even distribution of combusting product probably due to more even mixture spatial distributions. Similar to finding from Figure 40, it is interesting to note that UV emissions for 135 MPa inversed-delta injection is strongly detected downstream, comparable to 175 MPa rectangle injection with much broader axial span, probably due to poor atomization, mixing and reaction rate. It can be speculated that in 135 MPa inversed-delta injection, high-temperature reaction and soot oxidation did not fully completed until it progressed further downstream, resulting in long soot oxidation time.

### 3.2.3 Combustion Duration and Combustion Characteristics Analysis

In this section, combustion characteristics of extracted axial spray of the inversed-delta compared to the rectangle injection will be discussed from the AHRR acquired simultaneously during the high-speed simultaneous imaging tests. The pressure trace used for AHRR calculation was obtained with the upstream region setup to avoid pressure oscillation influence, prevalent in the present experiment. In previous section, sizable heat was released from the blocked sprays, impeding the interpretation of AHRR analysis from the targeted axial spray. Therefore, a layers of steel wool was fitted inside the nozzle cap to prevent the blocked sprays from reacting, permitting heat release rate derivation solely from the axial spray.

Figure 43 shows the ensemble average of AHRR from at least five shots for 175 MPa inversed-delta, 175 MPa rectangle and 120 MPa rectangle injection at the left side as well as 135 MPa inversed-delta and 135 MPa rectangle injection at the right side with their corresponding injection rate shown at secondary Y-axis. Figure 44 shows the injection period and combustion duration derived from CA10-90 analysis: CA10 and CA90 correspond to the timing where 10% and 90% amount from the integrated heat release, respectively. Similar total heat release amount at around 170 J in all injection profiles was measured, implying that the heat release rate is successfully derived from the axial spray. Additionally, the ignition delay in all injection profiles are comparable at approximately 450 μs.

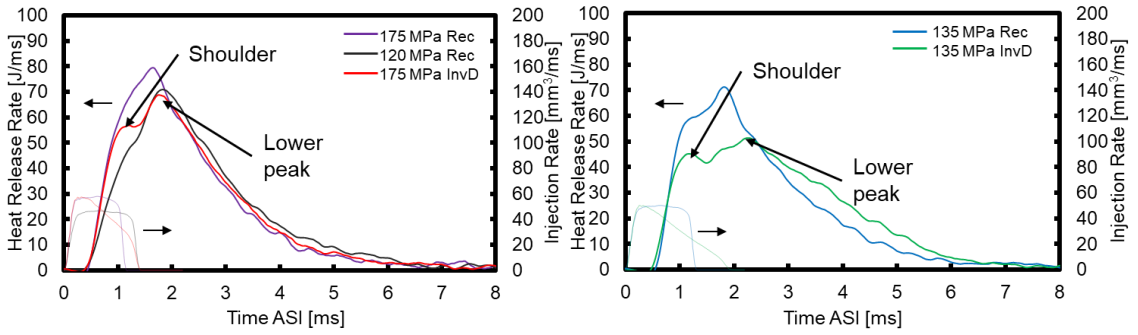


**Figure 43 Example of axial spray AHRR for 175 inversed-delta, 175 MPa rectangle, 120 MPa rectangle (left) and 135 MPa inversed-delta, 135 MPa rectangle (right). Ambient conditions: $\rho_g$=23.8 kg/m³, $P_a$=5.0 MPa, $T_a$=1050 K and 17% $O_2$. Injection conditions: φ0.12 mm orifice and $m_f$=5.0 mg**[100].

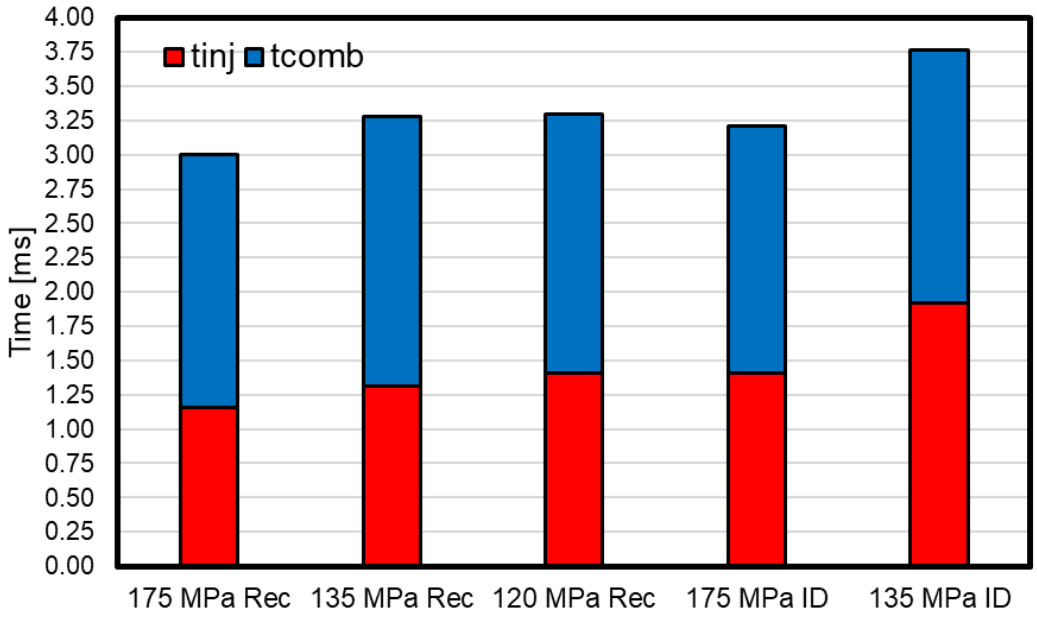


**Figure 44 Injection Period and Combustion Duration based on CA10-90 analysis from pressure-derived AHRR. Ambient conditions: $\rho_g$=23.8 kg/m$^3$, $P_a$=5.0 MPa, $T_a$=1050 K and 17% $O_2$. Injection conditions: φ0.12 mm orifice and $m_f$=5.0 mg**[100].

The combustion duration in 175 MPa inversed-delta injection is shorter by 3% compared to that 120 MPa rectangle injection although their injection duration is similar. Furthermore, it is noted that their heat release rate peak value at around 2.0 ms is comparable, while the rate of heat release during the late combustion phase seems to be slightly smaller in 175 MPa inversed-delta injection.

The initial rise of AHRR is comparable in 175 MPa inversed-delta and 175 MPa rectangle injection, probably due to similar preignition mixing characteristics however, the combustion duration was elongated by 7% in 175 MPa inversed-delta injection. It is interestingly noticed that their AHRR seems to be progressed similarly up to 0.9 ms, but then the AHRR of the inversed-delta injection begins to deviate from that of the rectangle injection, slowing down the combustion rate that results in lower peak but longer combustion duration. The effect of the EOI pressure on the combustion characteristics was investigated from the 135 MPa inversed-delta and 135 MPa rectangle injection AHRR comparison. Similar trends with 175 MPa AHRR comparison case are also observed in 135 MPa comparison case as well. Here, the AHRR of 135 MPa inversed-delta injection is still relatively high at 4.0 ms, results in a significantly longer combustion duration compared to that of 135 MPa rectangle injection.

It is interesting to note that the AHRR of the inversed-delta injection departs from that of rectangle injection of similar initial pressure at a deviation point, being observed as a unique “shoulder”-like shape. This shoulder formation suppresses heat release peak but leads to longer combustion duration as trade-off. Previously, much effort has been emphasized in reducing the heat release peak in attempt to reduce in-cylinder pressure and NOx emissions by restricting the initial fuel injection rate through ramp and boots injection rate shaping. However, these injection rate shaping strategies usually results in higher soot emissions and extended combustion period due to initial fuel-air mixing deterioration[47], [48]. By optimizing the inversed-delta injection strategy, one may be potentially able to reduced NOx emissions and engine noise levels simultaneously without significant soot emissions and thermal efficiency deterioration as the trade-off.

The inversed-delta injection is able to reduce combustion duration limited to the fixed injection period comparison cases (similar injection period) and it was observed that the inversed-delta injection exhibits a distinct “shoulder” characteristic. This shoulder formation seems to restrain the progress of AHRR in the inversed-delta injection. Therefore, the mechanism of the shoulder will be investigated from the spray structure perspective in the next subsection.

### 3.2.4 Investigation on the Combustion Mechanism

From the literature, it is widely accepted that the local heat release or high temperature reaction marked with OH radicals present near the stoichiometric thin layer region, surrounding the spray periphery[101]–[103]. For example, high heat release rate in high-pressure injection can be expected since its spray tip penetrates further, extending the spray length which results in increment of the reaction zone region. Therefore, it could be deduced that the reacting surface area might be directly related to the bulk heat release rate amount.

Investigation of the inversed-delta and rectangle spray tip penetration and cone angle might provide useful insight on the spray structure or geometry, and possibly shoulder formation mechanism. These macroscopic spray characteristics are relatively easy to measure, yet highly useful in determining other directly related parameters such as air entrainment (complex to be measured directly)[62]. For that purpose, non-vaporizing conditions observation of the injection profiles in the present study was conducted with similar setup and image analysis technique as shown in Figure 33. The spray tip penetration was measured with the similar approach in previous subsection while the spray cone angle was calculated using the

trigonometric function from the spray width measured at 5-, 10- and 15-mm axial distance from the nozzle tip. Figure 45 shows the AHRR, spray tip penetration and spray cone angle obtained for five injection profiles from 0.0 to 2.0 ms ASI as shown at the top, middle and bottom row, respectively.

In all injection profiles, the spray cone angle is similar and does not significantly change during the injection period, although the exact value of the spray cone angle is difficult to determine from the low-sensitivity DBI approach applied here[89]. From this zoomed-in chart, it is evident that the spray tip penetration of the inversed delta injections is smaller than that of the rectangle injections even at relatively low injection pressure rectangle injection at 120 MPa. It is interesting to observe that the timing of the spray tip diverging point closely matches the shoulder formation timing at around 0.9 ms. From the spray structure standpoint, the AHRR shoulder is likely to be formed as the reacting zone area at the spray periphery is suppressed, begins when the spray tip penetration of the inversed-delta injection departs from that of the rectangle injection.

Kokjohn and Reitz have performed a multimode combustion modeling, combining a comprehensive kinetics scheme for volumetric heat release and a level-set-based model for turbulent flame propagation to investigate the roles of flame propagation, turbulent mixing and volumetric heat release in the Diesel combustion[104]–[106]. Their results showed that the combustion process in a conventional Diesel engine (i.e. high temperature and short ignition delay) is indeed dominated by volumetric heat release in a thin layer zone enveloping the spray periphery rather than flame propagation. The Diesel spray rate of combustion is controlled by the transport of a reactive mixture to the reaction zone, suggesting that bulk heat release rate is directly related to the spray structure that is mainly dependent on the spray tip penetration and the cone angle.

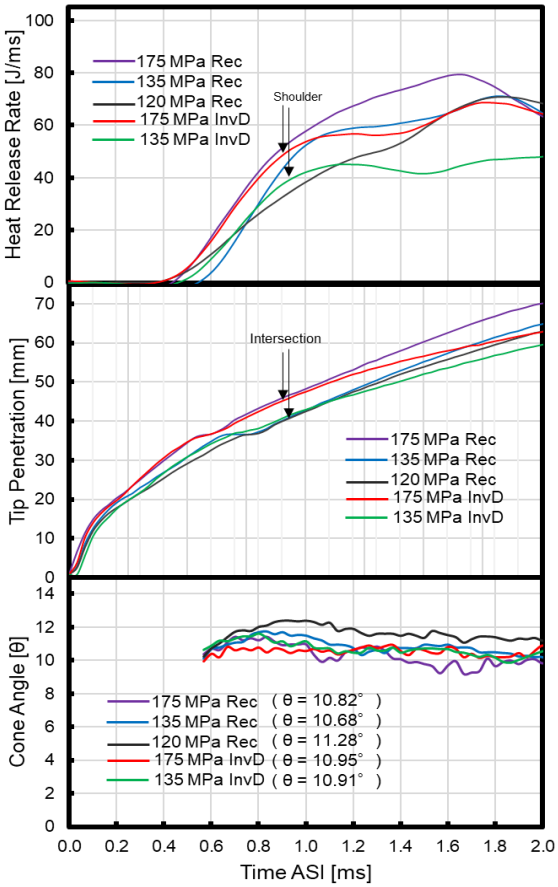


**Figure 45 The ensemble average of AHRR (top), spray tip penetration (mid) and spray cone angle (bottom, noted with quasi-steady average angle). Ambient conditions: $\rho_g$=23.8 kg/m$^3$, $P_a$=5.0 MPa, $T_a$=1050 K and 17% $O_2$. Injection conditions: φ0.12 mm orifice and $m_f$=5.0 mg**[100].

The inversed-delta injection combustion behavior in non-impinging Diesel spray flame can be summarized as follows. The initial heat release rate up to the shoulder is dependent to the initial injection rate/pressure. Then, the rate of heat release is suspected of being determined by the reactive zone volume that is proportional to the spray tip penetration. From the spray momentum standpoint, it is suspected that the inversed-delta injection ramp-down slope and EOI pressure probably governs the tip penetration (i.e. the tip penetration is highest in the rectangle injection, while lowest in steepest ramp-down slope coupled with smaller EOI pressure for the inversed-delta injection case). Manipulation of reaction zone volume and additional turbulence pulse might be advantageous for mixing promotion, although its trade-off with wall cooling loss need to be taken into consideration.

## 3.3 Investigation of Air Entrainment from the Liquid Length, Lift-off Length and Soot Onset Characteristics

### 3.3.1 Injection Profiles Matrix

From previous sections, it is understood that inversed-delta injection exhibits spray tip rich mixture suppression but has only limited effects on combustion duration reduction, suggesting the air entrainment enhancement might be lesser than previously anticipated. Therefore, it is of interest to study the air entrainment quantity in the inversed-delta injection case, but its direct qualitatively measurement optical setting is complex, which is out of the time limit and scope for this present study. Fortunately, it is known that the Diesel combustion and emissions behaviors are highly dependent on the events occurring at the spray flame upstream region: relatively easy to observe the fuel-air mixing and auto-ignition properties indirectly from the so-called liquid length and lift-off length, respectively[19]–[22], [107]. However, most of the research works are conducted under quasi-steady injection rate with only a few discussing on the transient injection rate influence[10], [26], [35], [46], [108], [109]. Investigation on the inversed-delta-injected Diesel spray flame characteristics is unavailable to date thus, its effects on the Diesel spray liquid length, lift-off length and soot onset (i.e. shortest axial distance from nozzle tip to soot particle formation) will be discussed in this section with a wider variation yet systematic injection profiles test matrix. Results from this study could provide useful insight on the inversed-delta injection mixing processes, providing a date set that provide huge opportunity for numerical modeler for future work.

Figure 46 and Table 10 shows the injection rate ensemble averaged at ten shots using Bosch-type long tube method from a multi orifices φ0.12 mm ×8+1 injector and details, respectively. Relatively high injection mass was set for all injection parameters since the late combustion is more pronounced in high load operating condition. The Diesel spray flame behaviors were diagnosed from the above mentioned φ0.12 mm axial spray. Its injection mass and injection rate in this particular study can simply be obtained by dividing the total injection mass to the number of orifices. Due to the pressure leak necessary the for lower injector actuation, actual sac pressure for the inversed-delta injection was slightly smaller by approximately 20 to 25 MPa than the common rail pressure supplied. The EOI pressure for inversed-delta injection was estimated from the injection rate acquired.

Selection criteria for five inversed-delta and seven rectangle injection-rate shaping profiles performed in this parametric study were based on several aims. Firstly, the effects of EOI pressure reduction based on injection mass variation at 40, 45 and 50

mg with similar initial injection pressure of 175 MPa is represented at the left column in Figure 46 and Table 10; noted that lower EOI pressure is exhibited for higher injection amount due to higher hydraulic spill in the inversed-delta injection profiles. Influence of initial injection pressure (couple with the EOI pressure influence) was investigated with 175, 160 and 140 MPa 45 mg inversed-delta and rectangle injection profiles. Thirdly, the effects of the injection rate shaping injected within similar injection period was investigated with 175 MPa inversed-delta and 110 MPa rectangle injection at 45 mg, and 175 MPa inversed-delta and 123 MPa rectangle injection at 40 mg. Examination on impacts of inversed-delta injection ramp-down rate and split injection strategies are intended in the future study.

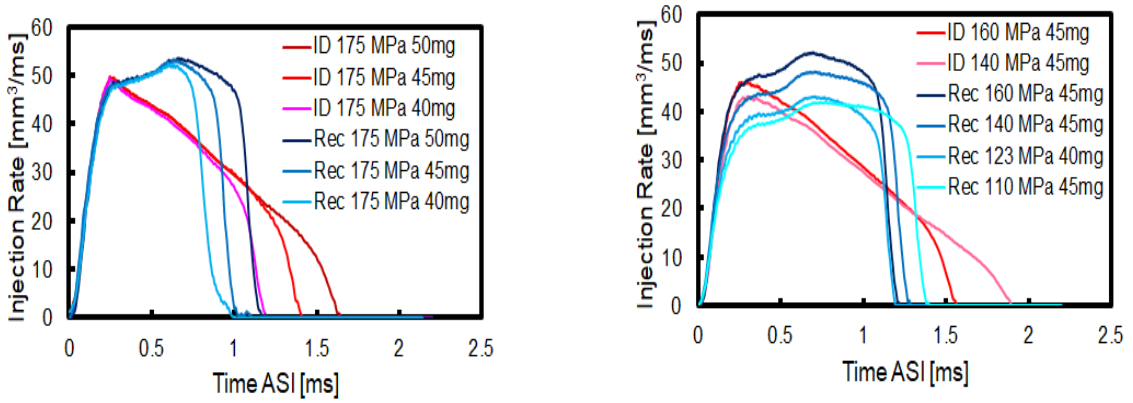


**Figure 46 Injection rate profiles measured using the Bosch-type long-tube method. Injection conditions: φ0.12 mm × 8 original +1 additional axial orifice**[90].

**Table 10 Injection rate shaping profiles using TAIZAC injector.**

| Injection Profile | $t_{inj}$ ms | $P_{rail}$ MPa | $P_{inj}$ MPa | $m_f$ mg | Injection Profile | $t_{inj}$ ms | $P_{rail}$ MPa | $P_{inj}$ MPa | $m_f$ mg |
|---|---|---|---|---|---|---|---|---|---|
| 175 MPa ID 50mg | 1.74 | 200 | 175-15 | 50 | 160 MPa ID 45mg | 1.70 | 180 | 160-25 | 45 |
| 175 MPa ID 45mg | 1.50 | 200 | 175-35 | 45 | 140 MPa ID 45mg | 2.07 | 160 | 140-5 | 45 |
| 175 MPa ID 40mg | 1.31 | 200 | 175-55 | 40 | 160 MPa Rec 45mg | 1.45 | 160 | 160 | 45 |
| 175 MPa Rec 50mg | 1.37 | 175 | 175 | 50 | 140 MPa Rec 45mg | 1.52 | 140 | 140 | 45 |
| 175 MPa Rec 45mg | 1.22 | 175 | 175 | 45 | 123 MPa Rec 40mg | 1.44 | 123 | 123 | 40 |
| 175 MPa Rec 40mg | 1.12 | 175 | 175 | 40 | 110 MPa Rec 45mg | 1.65 | 110 | 110 | 45 |

### 3.3.2 Liquid Length, Lift-off Length and Soot Onset with Respect to Start of Injection Timing

Figure 47 shows the examples of liquid penetration acquired during the injection period for 12 injection parameters arranged in a similar manner mentioned in Figure 46 and Table 10. Three sets of columns represent the high-speed images taken at the time steps depicted at the top right corner for 0.50, 0.75 and 1.00 ms ASI timing. The injection profiles are noted at the bottom of all images in each set, and the axial location of the spray is shown at the top and bottom of each image column with purple vertical dashed lines indicate its steady liquid length averaging from 5 shots. Noted that the images were processed to enhance its contrast. Figure 48 summarized the steady liquid length and its standard deviation for all injection profiles.

Noticed that the liquid length is largely fluctuating at a value of approximately 10% during the injection period. It is interesting to note that the injection pressure and injection rate shaping show neither significant nor systematic influence on the quasi-steady liquid penetration and the near field liquid cone angle. From the liquid length scaling law derived based on the mixing-limited assumption, the liquid length can be determined at the location where its centerline mixture fraction is equal to the mixture fraction for a saturated liquid-vapor equilibrium state $Z_{sat}$[21], [22]. From Equation (4) and (5), lower injection pressure proportionally induces smaller air entrainment suggesting the value of the centerline mixture fraction at the associated liquid length should be constant in any injection rate shaping profile.

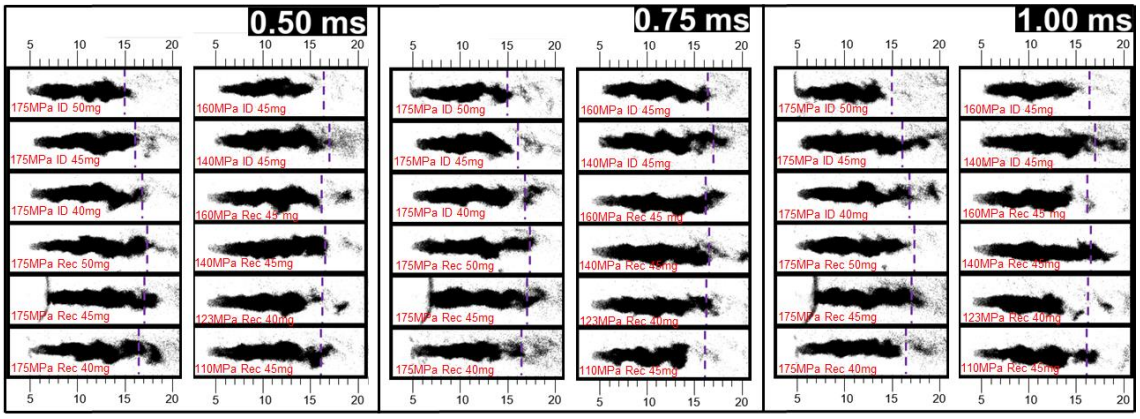


**Figure 47 Examples of the liquid phase fuel high-speed DBI images at 0.50 (left), 0.75 (middle) and 1.00 ms (right) from the start-of-injection timing. Ambient conditions: $\rho_a$=23.8 kg/m³, $P_a$=5.0 MPa, $T_a$=1050 K and 17% $O_2$. Injection conditions: d=φ0.12 mm**[90].

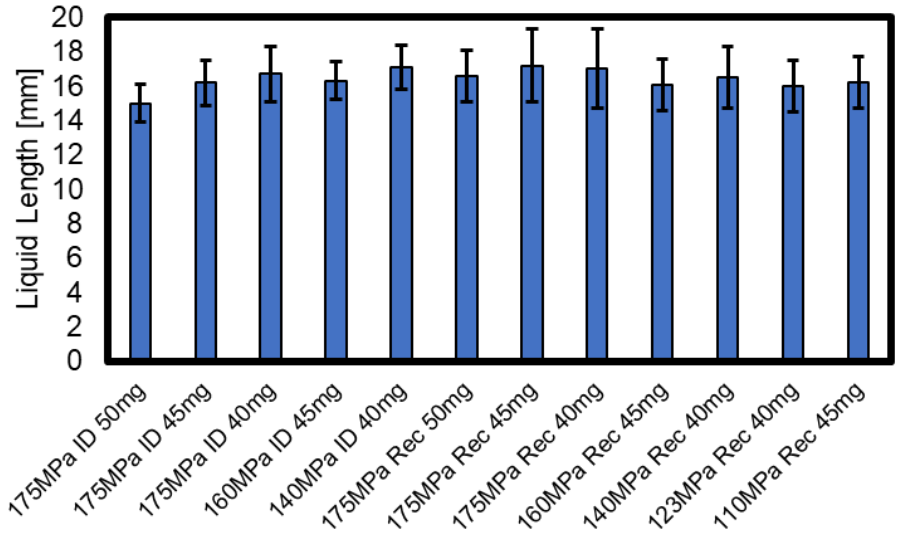


**Figure 48 Liquid length ensemble average and standard deviation.**

Study of the lift-off length in the slow and fast ramp-down was conducted by Knox et al. realized by direct assembly of three injectors which are somewhat similar to the TAIZAC injector construction concepts although the ramp-down rate is less steeper due to the larger inner volume[38], [39], [110]. It is mentioned that the slower ramp-down rate results in stronger combustion recession due to favorable air-fuel mixture formation upstream to the lift-off length, probably due to less over-lean effects owing to weaker entrainment waves. On the other hand, faster ramp-down rate induces stronger entrainment waves and forms air-fuel mixture that is too lean for the auto-ignition to occur, thus suppressing the combustion recession event. This observation and reasoning are plausible with the liquid length recession noticed in the present study. However, the question of how will progressive ramp-down rate as in the inversed-delta injection effects the lift-off length during the injection period is unclear.

Figure 49 shows the OH* signal representative image obtained at 30,000 fps, acquired separately from the DBI images. Four sets of column cells represent the high-speed images taken at the time steps depicted on the top at 0.70, 0.90, 1.10 and respective end of injection EOI timing for each injection profile. The images are arranged with the similar fashion to the one mentioned in Figure 46, and the injection profile is indicated at the bottom of each image. Yellow dashed vertical lines show the location of the lift-off length while the axial location markers are laid at the top and bottom of each column. Figure 50 summarized the ensemble average lift-off length, standard deviation and ignition delay for all injection profiles. The

standard deviation was calculated from ensemble average of 5 shots during a relatively stable period of lifted flame location., excluding a short unstable period after the autoignition and after the EOI timing.

Similar to the liquid length results, it is observed that the lift-off length is independent of injection rate shaping profiles, apart from a slight dependent on the injection pressure for the rectangle injection as reported by some researchers[23], [107]. The axial distance of first OH* appearance shown in 0.50 ms is correlated to its ignition delay before shifting to a quasi-steady location at approximately 0.90 ms. It is interestingly noted that the lift-off length seems to be constant although the injection pressure or the injected velocity is significantly reduced as in 175 MPa ID 50mg and 140MPa ID 45mg cases, affirming that the effects of fuel velocity on the lift-off length is marginal[107].

Idicheria et al. investigated the relationship between the ambient oxygen concentration with the lift-off length $H$ and corresponding cross-sectional average equivalence ratio $\emptyset(H)$ represents by Equation (15) and (16)[19]. Where $(A/F)_{st}$, $x$, $x^+$, $\rho_a$, $\rho_f$ , $\theta$, $c_a$, $d$, $a$ and $\beta$ indicates air-fuel ratio at stoichiometric mixture, penetration length, characteristics penetration length, ambient density, fuel density, spray cone angle, area-contraction coefficient, orifice diameter, constant value of 0.66 and fuel volume fraction profile, respectively. It is concluded that, although the lift-off length H is inversely proportional to the oxygen concentration, the $\emptyset(H)$ collapsed at the same value, emphasizing the importance of the local equivalence ratio for auto-ignition and the lift-off position.

$$\overline{\emptyset} = \frac{2(A/F)_{st}}{\sqrt{1 + 16(x/x^+)^2 - 1}} \tag{15}$$

$$x^+ = \sqrt{\frac{\rho_f}{\rho_a}} \frac{\sqrt{c_a} d}{\alpha \tan(\theta/2)} \beta \tag{16}$$

The equations above indicate that the spray equivalence ratio spatial distribution is independent of the injection pressure as observed in a typical stratified structure of a diesel spray flame[68]. Since the lift-off length or the auto-ignition location remains stable during injection period in this study, it seems that the axial mean equivalence ratio $\emptyset(H)$ is independent of the injection pressure variations during the injection period (in other words, the injection rate shaping), contrary to our expectation based on EOI entrainment wave concept.

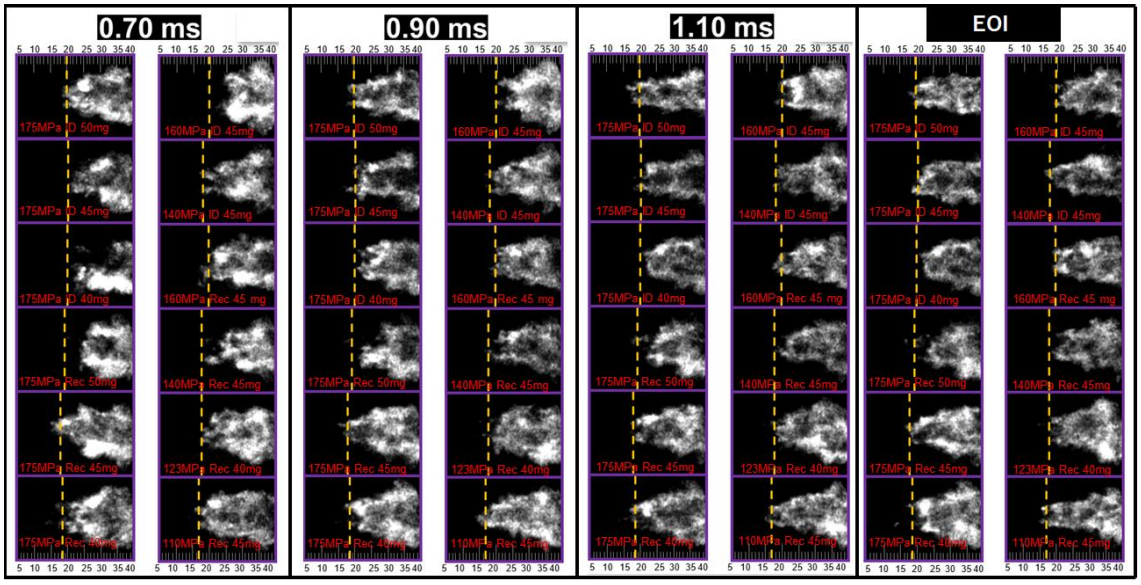


**Figure 49 Examples of the high-speed UV emissions images of 310 nm at 0.70, 0.90, 1.10 ms and at the EOI from the start of injection timing. Ambient conditions: $\rho_a$=23.8 kg/m$^3$, $P_a$=5.0 MPa, $T_a$=1050 K and 17% $O_2$. Injection conditions: d=φ0.12 mm**[90].

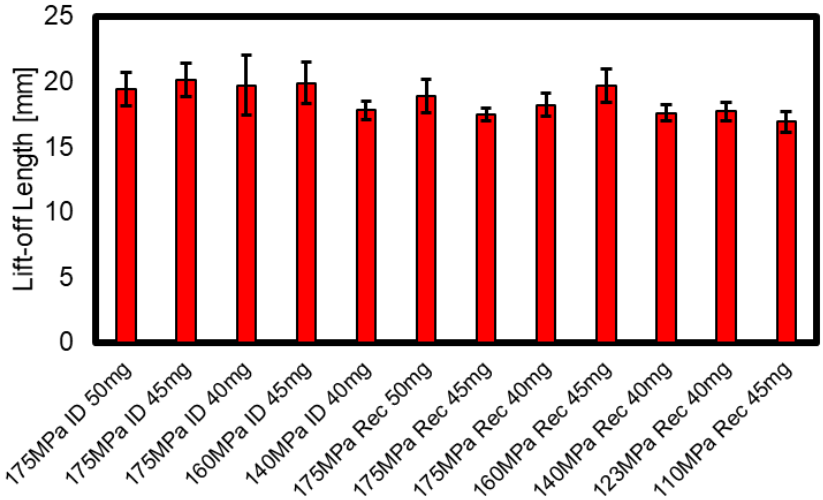


**Figure 50 Lift-off length ensemble average, standard deviation and ignition delay.**

It is well-known that the initial soot formation or the soot inception is strongly dependent to the air-fuel equivalence ratio Ø and temperature T, suggesting that the soot onset could serve as an excellent indicator of the local equivalence ratio. Since the liquid length images discussed previously are acquire with the viewing field up to 40-mm axial distance, the impact of the injection rate shaping profiles on the soot onset can be conveniently investigated from the same images.

The arrangement sequence of each injection profile in Figure 51 is set similar to the previous liquid length images shown in Figure 47. Four sets of time step are aligned in an array where the top-left, top-right, bottom-left and bottom-right cell represents the high-speed images taken at 0.90, 1.00, 1.25 and 1.50 ms, respectively. The injection profile is mentioned at the bottom of all images and the spray axial distance is indicated at the top and bottom of each image column, and purple vertical dashed lines mark the referral liquid length. A thick and relatively narrow shadow at the left side of the image indicates the liquid fuel region, followed by a relatively brighter spot where the vapor phase fuel-air mixture slightly refracts the background light, and at the right side of the image is shadow from the soot particles.

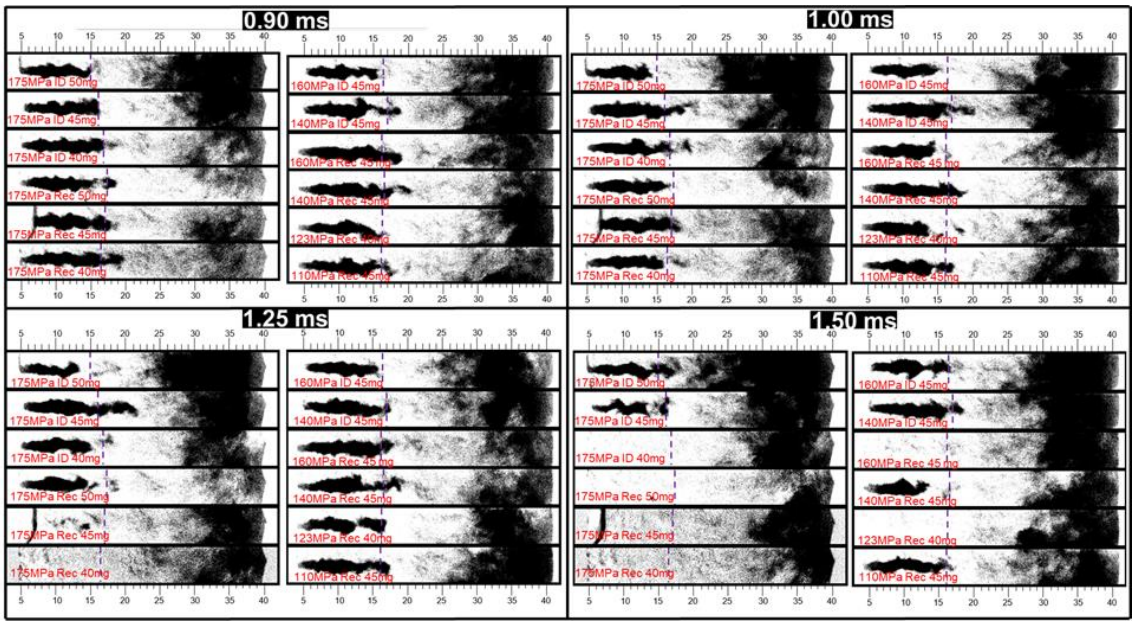


**Figure 51 Examples of the high-speed DBI images at 0.90 (top-left), 1.00 (top-right), 1.25 (bottom-left) and 1.50 ms (bottom-right) from the start-of-injection timing. Ambient conditions: $\rho_a$=23.8 kg/m$^3$, $P_a$=5.0 MPa, $T_a$=1050 K and 17% $O_2$. Injection conditions: d=φ0.12 mm**[90].

At 0.90 ms, the soot onset location appears to be similar in all the rectangle injection profiles. It is interesting to note that as the combustion progresses, the soot onset for the inversed-delta injections progressively recedes towards the nozzle tip, while this trend is not as apparent for the rectangle injection profiles. Furthermore, it is observed that the soot onset recession is stronger in lower EOI injection pressure inversed-delta injection as such in 175 MPa ID 50 mg and 140 MPa ID 45 mg cases. These results are significant since it implies that the air entrainment per injected fuel amount might actually be promoted in the inversed-delta injection during the

injection period: axial location of soot formation equivalence ratio might be accelerated and shifted nearer to the nozzle tip (will be discussed in the next section based on 1D simulation).

### 3.3.3 Liquid Length, Lift-off Length and Soot Onset with Respect to End of Injection Timing

Although no significant difference was noticed on the liquid length and lift-off length for all injection profiles during injection period, investigation of those properties were extended and examined according to their end of injection EOI timing since the entrainment waves strength and speed are dependent on the injection timing and pressure at the EOI. Figure 52 shows the liquid penetration similar to Figure 47, but the time steps were adjusted based on the EOI timing to highlight the vaporizing event just after the injection was ended. It is observed that in the rectangle injection profiles, the liquid fuel is fully vaporized at approximately 0.03 ms after EOI except for a relatively low injection pressure condition as in 110MPa Rec 45mg case. In the inversed-delta injection profiles, although the exact EOI observation timing is less explicit, it is noted that the liquid fuel in the inversed-delta injection presence is still apparent at later timing of 0.04 ms from EOI. The liquid fuel at this timing has a much smaller width, but the final penetration distance appears to be comparable to the quasi-steady one.

Results from Kook et al. EOI transient liquid length study showed that the liquid length slightly recedes towards the nozzle tip in a short instance just after the EOI in the fast ramp-down (i.e. resembling the rectangle injection) while no liquid length recession is observed in the slow ramp-down (i.e. resembling the inversed-delta injection). It is suspected that the air entrainment after the EOI is weaker and slower in the inversed-delta injection compared to that of the rectangle injection, since the entrainment waves strength and velocity is correlated to the EOI pressure[26], [33]. From fuel-air mixture momentum conservation perspective, if the spray cone angle remains constant during injection rate decelerating period, the air entrainment have to be increased to compensate the decreasing injected fuel mass[33].

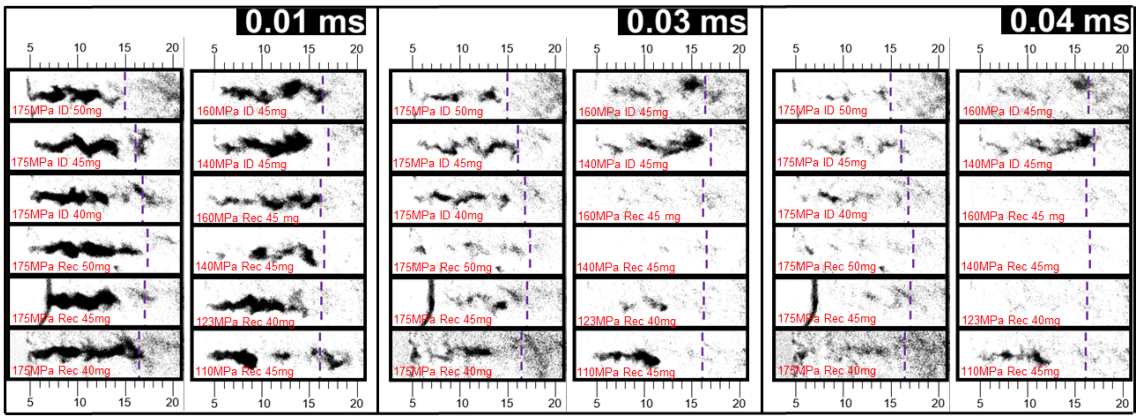


**Figure 52 Examples of the liquid phase fuel high-speed DBI images at 0.01 (left), 0.03 (middle) and 0.4 ms (right) from the end-of-injection timing. Ambient conditions: $\rho_a$=23.8 kg/m$^3$, $P_a$=5.0 MPa, $T_a$=1050 K and 17% $O_2$. Injection conditions: d=φ0.12 mm**[90].

Figure 53 represents the UV emissions at 310 nm images with similar injection profiles to the one presented in Figure 49, but the timing was adjusted according to their respective EOI timing. Due to the finite time necessary for fuel vaporization, mixing and ignition processes, no changes are observed at 0.20 ms from EOI. However, approximately from 0.60 ms after EOI the combustion recession event is noticed at all injection profiles where the combustion recession seems to occur at a faster rate for the rectangle injection than that of the inversed-delta injection. At 0.8 ms from EOI, the combustion recession length for the inversed-delta injection reaches comparable magnitude as in the rectangle injection case. It can be stated that the combustion recessions occur at the similar recession length or strength, but the rate of combustion recession is much faster for the rectangle injection, likely due to the stronger and faster EOI entrainment waves. It should be noted that the effects of atomization deterioration due to EOI pressure reduction on the liquid length and combustion recessions could be considered as well, but it is out of scope of this study.

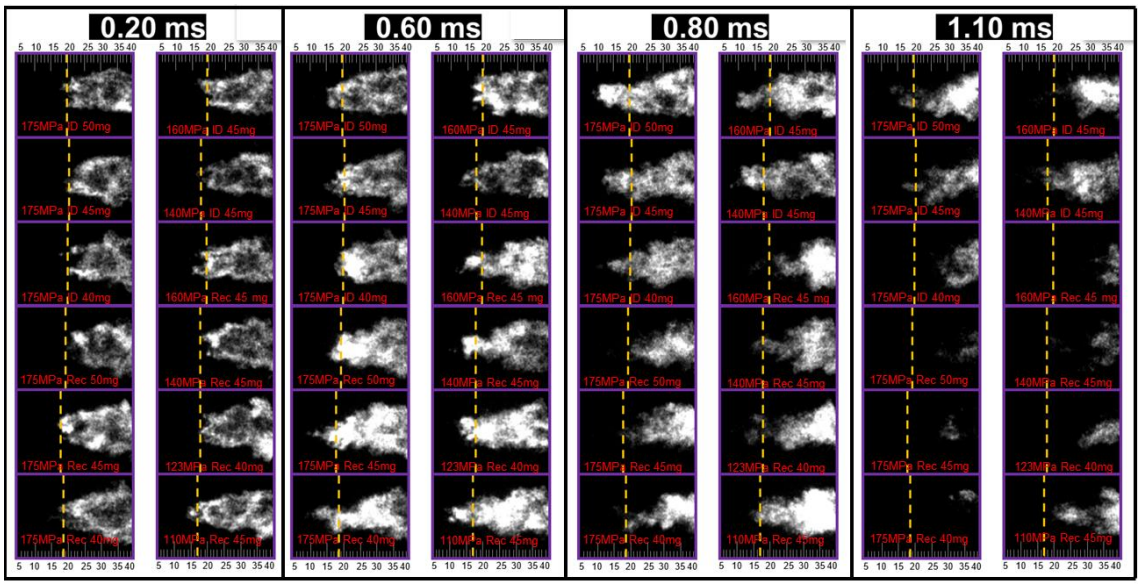


**Figure 53 Examples of the high-speed UV emissions images of 310 nm at 0.20, 0.60, 0.80 and 1.10 from the end-of-injection timing, from left-to-right. Ambient conditions: $\rho_a$=23.8 kg/m$^3$, $P_a$=5.0 MPa, $T_a$=1050 K and 17% $O_2$. Injection conditions: d=φ0.12 mm**[90].

It is noticed that the combusting product appears to linger more at the upstream region in the inversed-delta injection case, and seems to be dependent to its EOI injection pressure: lower EOI injection pressure results in more OH* existence nearer to the nozzle tip, probably due to the slower following spray velocity in the inversed-delta injection. Higher upstream region combustion activity coupled with lower spray penetration in the inversed-delta injection as observed in the previous sections might potentially reduce the cooling loss in the actual Diesel engine since contact between the hot gases and the combustion chamber wall should be suppressed likely[76], [77], [111]. Attempt to understand details of the cooling loss reduction mechanism in the inversed-delta injection case is investigated through infrared high-speed imaging of the wall-impinging Diesel spray flame in the next chapter.

Figure 54 shows the high-speed DBI images with the timing adjusted to their respective EOI timing. Here, observation of soot recession strength inverse proportionality to EOI injection pressure for the inversed-delta injection profiles is more explicit. Note that for larger injection pressure reduction cases, the soot onset recedes close to the location of the liquid length. Meanwhile, the soot onset for all rectangle injections are comparable just after the injection was ended at 0.05 ms

from EOI and the soot recession strength seems to be inversely proportional to the injection pressure. Again, these results suggest that the air entrainment per injected fuel amount might actually be promoted in the inversed-delta injection during the injection period and will be discussed further in the next section.

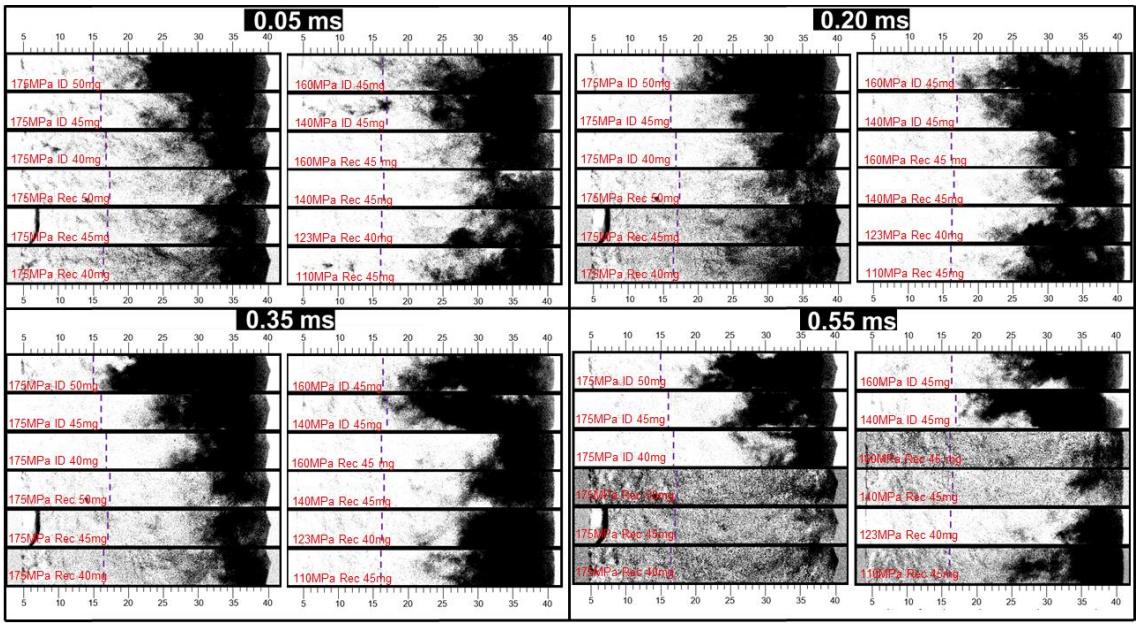


**Figure 54 Examples of the high-speed DBI images at 0.05 (top-left), 0.20 (top-right), 0.35 (bottom-left) and 0.55 ms (bottom-right) from the end-of-injection timing. Ambient conditions: $\rho_a$=23.8 kg/m$^3$, $P_a$=5.0 MPa, $T_a$=1050 K and 17% $O_2$. Injection conditions: d=φ0.12 mm**[90].

### 3.3.4 Discussions from One-dimensional Modeling

1D simulation based on Musculus and Kattke model was adapted to examine the effects of the inversed-delta injection on the associated air entrainment and equivalence ratio distributions[33]. Since the spray cone angle in the rectangle and inversed-delta injection was found similar in previous investigation, it could be speculated that the air entrainment per fuel injected might be enhanced owing to the jet momentum conservation[33], [98]. As a result, the liquid length should gradually decrease since the similar mixture fraction $Z_{sat}$ can be achieved much faster at nearer location to the nozzle tip.

Figure 55 shows the experimental and simulation results of the liquid penetration in the inversed-delta and rectangle injection cases. The ensemble averaged liquid penetration and individual shots are shown by a thick and narrow solid line, respectively. Noted that the calculated liquid penetration is overpredicted and normalized value is presented to avoid confusion. Pickett et al. suggested that this

model can be validated based on the spray tip penetration rather than the spray cone angle or the liquid length due to the difficulty to measure actual spray angle experimentally and potentially incorrect liquid fuel distributions radial profiles, respectively[68]. Furthermore, the value of $Z_{sat}$ for the fuel and thermodynamics conditions investigated in the present study was not measured, instead it was referred to $Z_{sat}$=0.34[68]. Nonetheless, this implication does not affect the overall understanding of mixing and vaporization process which is the primary interest here. However, the simulation results showed that the liquid length of the inversed-delta injection progressively shortened during the injection period, contrary to the experimental data, suggesting opportunity to improve this simple 1D model particularly at the upstream region.

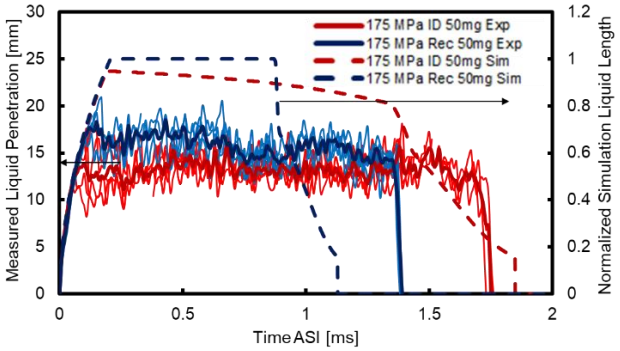


**Figure 55 Liquid penetration of the experiment (solid lines) and 1D simulation (dashed line) for 175 MPa rectangle and 175 MPa inversed-delta injection.**

From Figure 56, the soot onset seems relatively constant for the rectangle injection profiles, independent to the injection pressure. Meanwhile, it is evident that the soot onset is receding towards the nozzle during the injection period in the inversed-delta injection profiles, and the recession strength seems to be inversely proportional to the EOI injection pressure. This observation is clearly different from the trends exhibit by the liquid length and lift-off length: if the air entrainment does not increase during the inversed-delta injection period, the soot onset location is also supposed to be constant.

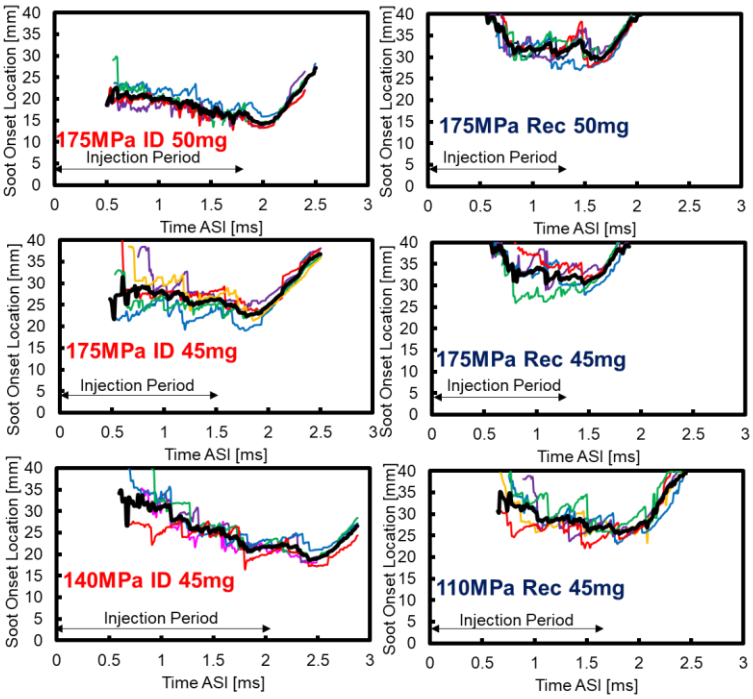


**Figure 56 Ensemble averaged (thick black line) and shot-by-shot variations (thin solid lines) of the soot onset. Ambient conditions: $\rho_a$=23.8 kg/m³, $P_a$=5.0 MPa, $T_a$=1050 K and 17% $O_2$. Injection conditions: d=φ0.12 mm.**

To explore further, Figure 57 shows the fuel-air equivalence ratio $\emptyset$ contour spatial distributions or the stratified "layer" calculated from the 1D simulation with the DBI images laid on top. Four selected injection profiles is indicated at the bottom-right corner of each contour chart and the results are divided into four cells that represent 0.50, 1.10, 1.40 and 1.90 ms ASI timing from top to bottom. The typical value of soot inception at jet centerline at approximately $\emptyset_{cl} = 2$ is marked with a green dashed vertical line. Note that it is difficult to locate its precise location at earlier timing, and after the entrainment waves perturbation.

It is interesting to note that, the experiment soot onset location correlates reasonably well with the soot inception value marked by the vertical green lines in all injection profiles. For rectangle injections, the same soot onset location is likely caused by the similar stratified structure in any injection pressure according to Equation (16). On the other hands, the calculated jet centerline equivalence ratio of $\emptyset_{cl} = 2$ and experimental soot onset progressively shifted upstream during the injection period in the inversed-delta injection case with comparable timing and strength, indicating that the soot onset is highly sensitive to the instantaneous variations of the local equivalence ratio.

From the soot onset recession and spray tip rich mixture suppression results[77], the air entrainment per injected fuel amount is likely to be promoted during the inversed-delta injection period from around the midstream region and possibly beyond. Key findings from this section can be described as follows. (1) No notable difference is observed on liquid length and lift-off length between the inversed-delta injection and rectangle injection, possibly due to lack of sensitivity of the optical diagnostics methods and insufficient injection period (i.e. relatively long time is required for lift-off stabilization[66]). (2) Weaker air entrainment wave in the inversed-delta injection compare to that of rectangle injection, leading to insufficient mixing after EOI. (3) Promotion of air entrainment in the inversed-delta injection case might be notable only from soot onset location downward, starting from the midstream region. Further investigation on the inversed-delta injection plausible air entrainment mechanism is necessary.

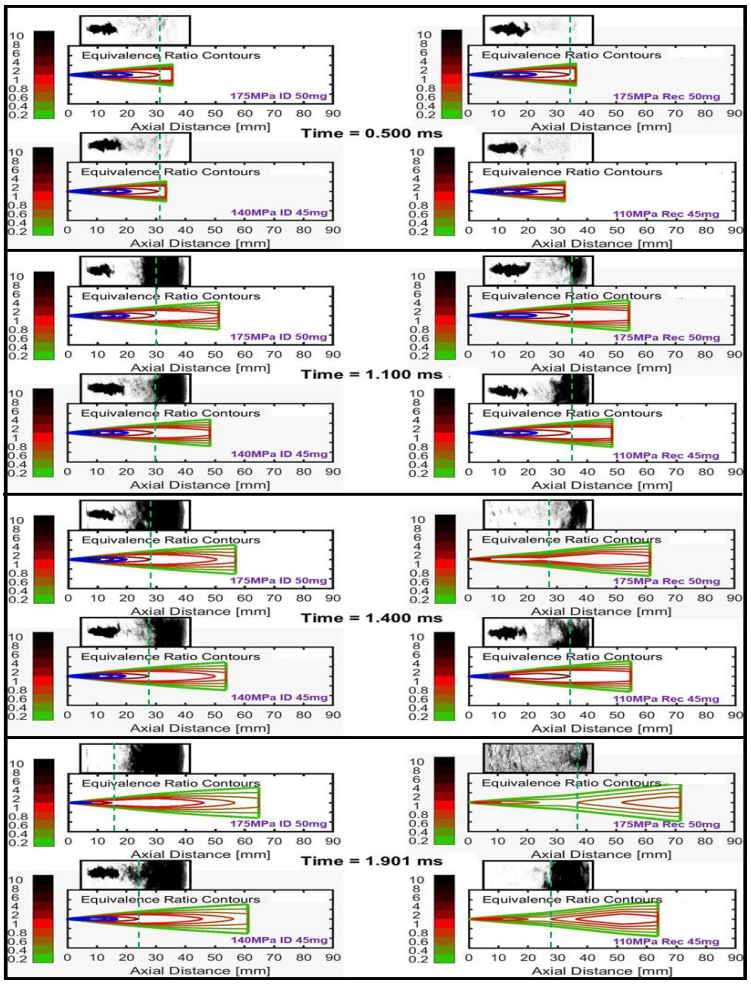


**Figure 57 Examples of the acquired DBI images and simulated fuel-air equivalence ratio distributions at 0.50, 1.10, 1.40 and 1.90 ms from the start-of-injection timing**[90].

## 3.4 Discussions on Inversed-delta Injection Conceptual Model

### 3.4.1 Expectation on Inversed-delta Injection Diesel Spray Flame Characteristics

Following our expectation as illustrated in Figure 11, extensive experimental results presented throughout this chapter proved the suppression of spray tip rich mixture, reduction of tip penetration and more even mixture distributions in the inversed-delta injection compare to than those of the rectangle injection. However, the inversed-delta injection effects in reducing combustion duration is limited and no notable different are observed on liquid length and lift-off length during injection period, indicating insignificant air entrainment promotion up to soot onset location. In some cases of excessive pressure reduction, longer soot residence time and broader spray tip rich mixture are observed, suggesting insufficient fuel-air mixing. Therefore, study on air entrainment mechanism in the inversed-delta injection or in EOI transient is imperative to enhance our understanding for effective strategy in reducing combustion duration.

1D modeling serve as a sophisticated tool in understanding the concept of the entrainment wave during the EOI transient although it should be interpreted with a great care since the Diesel jet in the 1D model is assumed as non-compressible, non-diffusing and constant jet spreading angle[33]. Due to the simple nature of the 1D model, the physics of air entrainment promotion mechanism is unclear thus results obtained might be overestimated. Singh and Musculus examine this entrainment wave event using a more realistic fully compressible, unsteady Navier-Stokes momentum equations in axisymmetric two-dimensional 2D computational fluid dynamics CFD simulation after EOI[105]. This Reynold-averaged Navier-Stokes RANS model predicts a broader region of increased air entrainment at a lower peak of 50% increment instead of factor of 3 predicted by 1D model with two phases of entrainment promotion, named as the acoustic wave and the momentum wave. The 2D CFD results resemble the entrainment wave profile measured by Eagle et al. via particle image velocimetry PIV technique[35].

Hu et al. strive to elucidate the fluid-mechanical mechanisms of air entrainment during transient EOI or deceleration phase by applying large eddy simulation LES on turbulent gas jet investigation[112]. Increase of entrainment during deceleration phase is also confirmed with this approach, although the shape of the entrainment wave is less defined than that of 1D model. Frequent indentations or large-scale vortices are observed after EOI likely because the spray becomes unstable due to transient spray momentum supply. From combination of Laser Induced Fluorescence LIF and particle image velocimetry PIV method on gas jet by Bruneaux et al[13],

large structure indeed enhanced ambient air influx the surrounding air engulfment, suggesting the large-structure plays a dominant role behind the entrainment wave mechanism.

### 3.4.2 Inversed-delta Injection Concept

LES simulation employing detailed chemical reaction schemes for inversed-delta and rectangle Diesel spray comparison was conducted by Adachi et al. [55]. The simulation results are adapted for the inversed-delta injection conceptual diagram shown in Figure 58 with some key findings highlighted in the textboxes. The rectangle injection and inversed-delta injection is depicted respectively at the left and the right column.

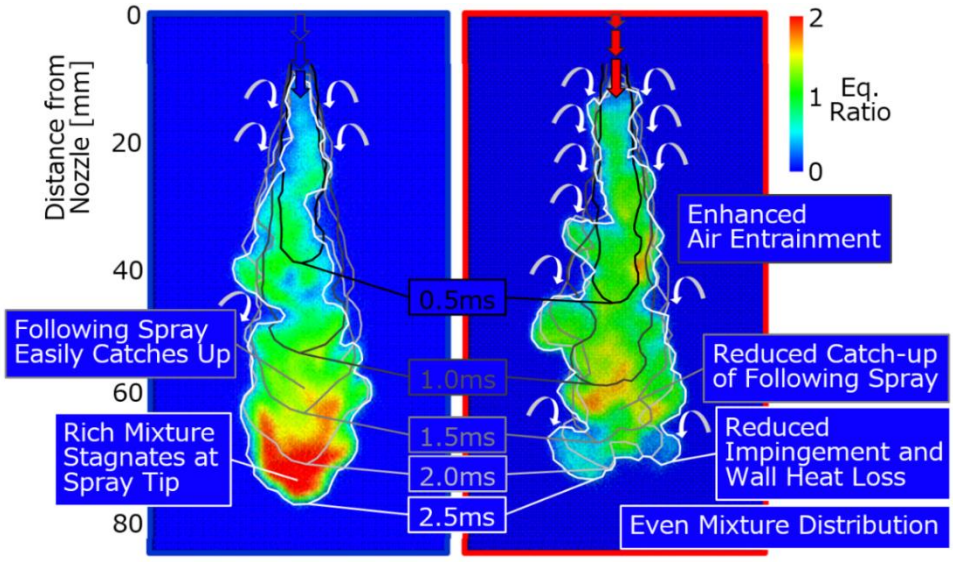


**Figure 58 Conceptual diagram of spray tip rich mixture formation process with conventional rectangle (left) and inversed-delta (right) injection rate shaping in Diesel spray flame**[55], [76].

Similar to our initial prediction, the spray tip penetration of inversed-delta injection is shorter and more even equivalence ratio contour spatial distribution is simulated in the inversed-delta injection compare to those of the rectangle injection. The rectangle injection exhibits relatively smooth spray flame outlines with occasional indentations while the transient inversed-delta injection displays more unstable edges with frequent indentations possibly due to enhanced growth and axial separation of large vortical structures, approximately at 30 mm axial distance and beyond, suggesting that air entrainment enhancement in inversed-delta injection is more pronounced starting approximately from the soot onset location[55].

Although the inversed-delta Diesel spray flame structure shown in the LES results correlate-well with high-speed imaging results obtained in the present study, its impacts on combustion duration reduction based on AHRR profiles and the large structure formation are less pronounced. This discrepancy could be caused by several factors. First, the experimental inversed-delta injection ramp-down rate might not be as aggressive as in the LES simulation. Secondly, temporal and spatial resolutions of the optical setup and technique in the present study might not be sufficient to visualize the transient indentation occasion. Experiment on direct measurement of Diesel spray flame vortices structure, air entrainment and its relationship with local heat release rate in the inversed-delta injection compare to those of the rectangle injection are currently ongoing.

### 3.5 Summary

A short conclusion for this chapter can be summarized as follows:

1. Inversed-delta injection exhibits spray tip rich mixture suppression, more even fuel distribution and shorter spray tip penetration than those of rectangle injection.
2. From apparent heat release rate AHRR, inversed-delta injection shows lower heat release peak than that of rectangle injection at similar initial pressure, potentially able to reduce engine noise. However, the effects of inversed-delta injection in reducing combustion duration is limited due to the AHRR shoulder formation: likely caused by smaller reacting zone surface area owing to the shorter tip penetration in inversed-delta injection case.
3. Liquid length and lift-off length during injection period are similar in both inversed-delta and rectangle injection cases likely due to trivial air entrainment enhancement. After the end of injection EOI, slower liquid fuel vaporization and combustion recession are observed in inversed-delta injection case probably due to the weaker EOI entrainment wave.
4. Soot onset progressively shortens during injection period for the inversed-delta injection while the location of soot recession seems constant in all rectangle injection cases: air entrainment per injected fuel amount might be enhanced in the inversed-delta injection starting from the soot onset location likely due to large structure air engulfment.

# 4 EFFECTS ON DIESEL ENGINE APPLICATION

This chapter will discuss TAIZAC inversed-delta injection rate shaping effects on Diesel engine thermal efficiency followed by a brief introduction on a novel infrared IR high-speed imaging of wall-impinging Diesel spray flame. At later part, tailpipe emissions results of inversed-delta injection and rectangle injection are compared. Focusing on smoke emissions, details investigation of soot production is conducted in a CVCC via DBI method.

## 4.1 Impacts on Thermal Efficiency

### 4.1.1 Engine Performance Test

From CVCC results, it was revealed that the inversed-delta injection does not significantly reduce the combustion duration but its spray tip penetration and combustion event occur more at upstream region, suggesting that the wall heat loss might be reduced and the thermal efficiency might be improved by the TAIZAC injector inversed-delta injection approach.

Figure 59 shows measured cylinder pressure and apparent rate of heat release for inversed-delta and rectangle injection using the TAIZAC injector at the top and bottom chart, respectively. The entire pressure histories and heat release rate during the pilot and pre injections, and heat release peak from the main injection are comparable in both injection profiles. Compare to the rectangle injection, at approximately 12 crank angle degree CAD, inversed delta injection heat release rate is slightly lower for 3CAD, before reversing the trend from 15 to 25 CAD, and then both of them become comparable again throughout the late combustion period.

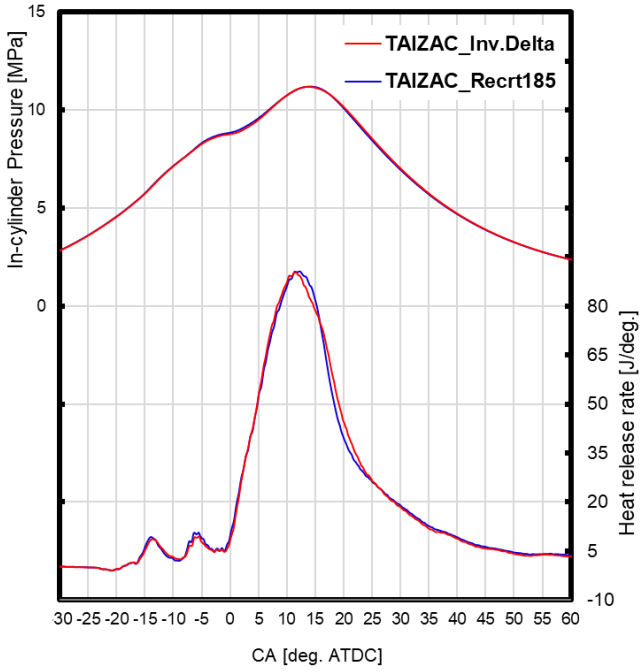


**Figure 59 Cylinder pressure (top) and apparent heat release rate (bottom) for rectangle and inversed-delta injections**[95]**. Injection rate profile can be referred to Figure 29.**

Figure 60 exhibits a comparison of heat balance analysis results between inversed-delta and rectangle injection using the TAIZAC injector, where the values of indicated thermal efficiency, exhaust loss, cooling loss and unburned loss are depicted. Despite of limited effects on combustion duration reduction, the inversed-delta injection successfully improves Diesel engine thermal efficiency by of 1.0pt compared to that of the conventional rectangle injection, that is accepted as a significant value among the Diesel engine community. Notable reduction of cooling loss by 1.3pt is observed, where this excess energy is reasonably split between the engine work and the exhaust loss.

Figure 61 shows comparisons of degree of constant volume and combustion temperature for the TAIZAC inversed-delta and rectangle injection profile. Slightly shorter combustion duration and lower cooling loss (i.e. usually accompanies with a higher exhaust loss) observed previously are in good agreement with the slight increase of constant volume degree value and exhaust gases temperature, respectively. It is interestingly noted the combustion duration (indicates by higher value of degree of constant volume) is slightly reduced in the inversed-delta injection despite of its elongated injection period compared to the rectangle injection, as shown previously in Figure 29.

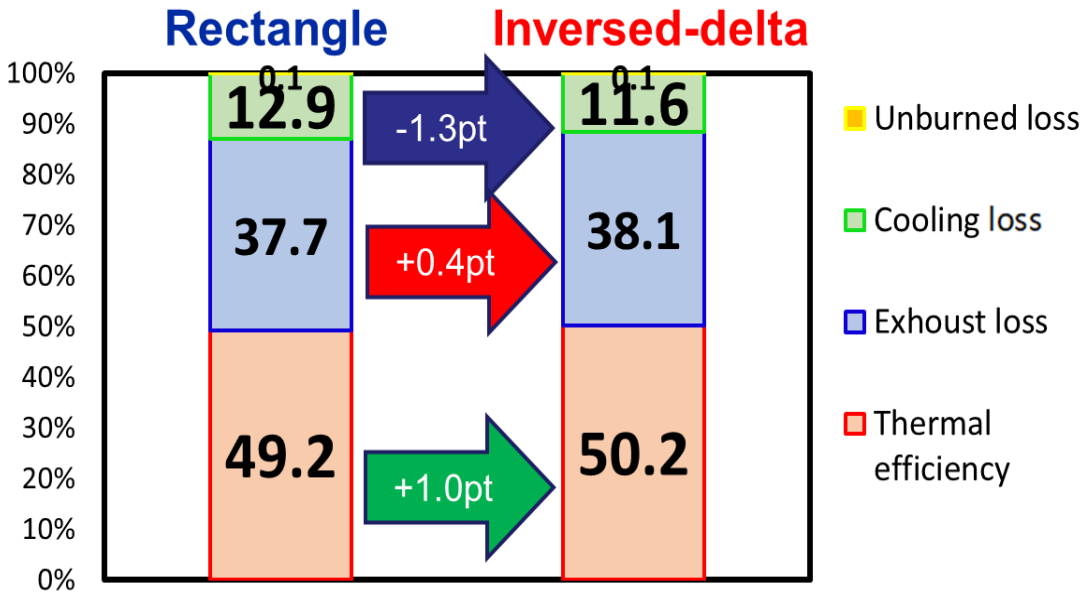


Figure 60 Heat balance for rectangle and inversed-delta injection conditions[95].

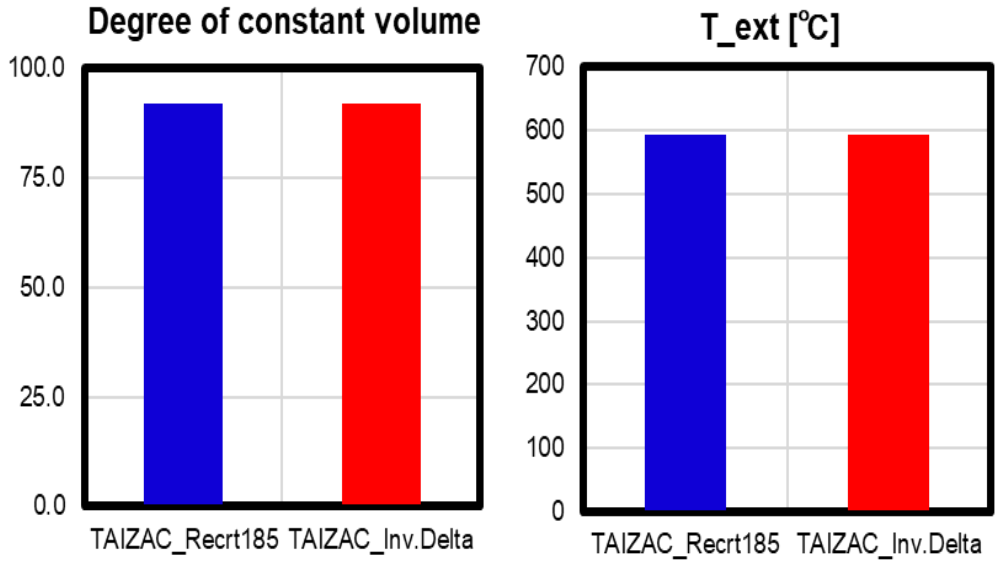


Figure 61 Degree of constant volume (left) and exhaust temperature (right) for rectangle and inversed-delta injection conditions[95].

### 4.1.2 High-speed IR Thermography of Wall Impinged by Diesel Spray Flame

The possible mechanisms for the reduced cooling loss by the inversed-delta injection need to be examined since its cooling loss in Diesel engine is significantly reduced. Recently, research on IC engine cooling loss mechanism is gaining attraction, however most of them are limited to simulation approach[113]–[115] or point-based measurement using heat flux sensors[116], [117].

Due to complex mechanism of heat transfer from Diesel spray flame to combustion chamber wall, several factors including hot flame impingement to the piston wall by velocity, temperature, contact duration and surface area need to be considered, addressing the needs to grasp the big picture of heat flux phenomena on the combustion wall surface in temporal sequence manner.

Slow development of high-speed infrared IR camera with at least 10,000 Hz order at adequate resolution has impeded the study on wall heat flux visualization. However, such camera has been made available in the market in year 2015, requiring development of an appropriate optical setup and novel diagnostics technique. In this section, first test to directly measure the wall heat flux during the Diesel spray flame impingement based on its IR thermal radiation is attempted with an optical setup illustrated in Figure 62[118]. The experiment was conducted in the similar CVCC as previously mentioned, and Diesel spray flame from axially-drilled orifice of φ0.12 mm was impinged to a quartz window with 35-mm-diameter effective view field at 27 mm axial distance. The quartz window was coated with a 1.2 μm-thick layer of chromium as a thermal radiation layer and to avoid soot radiation leakage. This chromium layer was strengthened with an additional layer of SiO at 10 nm thickness. Quartz window was selected due to its relatively low cost, but the results should be interpreted with caution since its thermal diffusivity value is smaller by two-order of magnitude compare to aluminum used as the Diesel engine chamber wall. Time sequence images were acquired with a TELOPS, FAST-IR M3k high-speed IR camera at 10,000 fps, 128×128 pixel at ambient conditions similar to the one presented in the previous chapter. Details on this experimental setup are explained elsewhere[118].

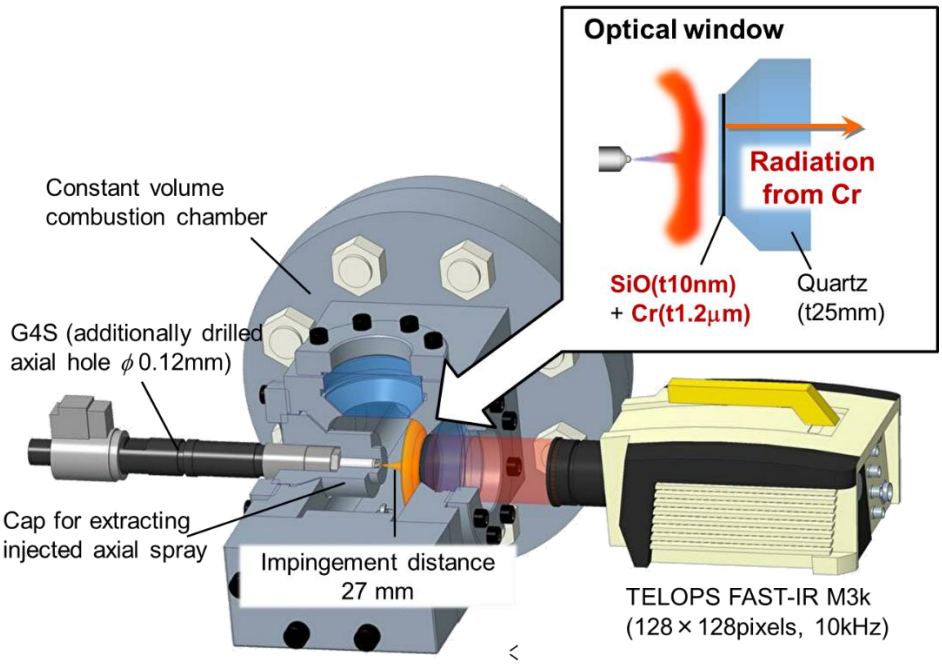


**Figure 62 Optical setup for high-speed infrared imaging of thermal radiation from chromium-coated quartz window surface impinged by Diesel spray flame in CVCC**[118].

Figure 63 shows the examination of IR signal from the 100°C-heated-quartz-window (to avoid vapor condensation from premixed gases combustion products). From the hot Diesel spray flame (up to 2500°C) contacts with the coated window, it was estimated that the window surface temperature will increase up to 300°C, thus example of theoretical black body radiation for the correspond temperature is shown as (A) Black Body Radiation. Note that horizontal axis indicates the wavelength from near IR at 1500 to far IR at 5500 nm. (B) depicts the individual emissivity from the quartz window and the chromium layer substance. It was estimated that the heat from the impinging Diesel spray flame penetrates the wall at about 0.2 mm in depth and heats it up 300°C, thus the value of the chromium layer and quartz window was multiplied with the individual emissivity (B) as shown at the middle row of the chart. (C) shows the wavelength range of the quartz window transmissivity and the fast IR camera sensitivity. Finally, the final product of (A), (B) and (C) as depicted as (D) shows the IR radiation detected. From the calculation results, it is proved that IR signal detected by the IR camera is mainly originated from thermal radiation of chromium thin layer instead of that from quartz window and the background signal can be mostly eliminated simply through background image subtraction owing to minimal overlapping signal.

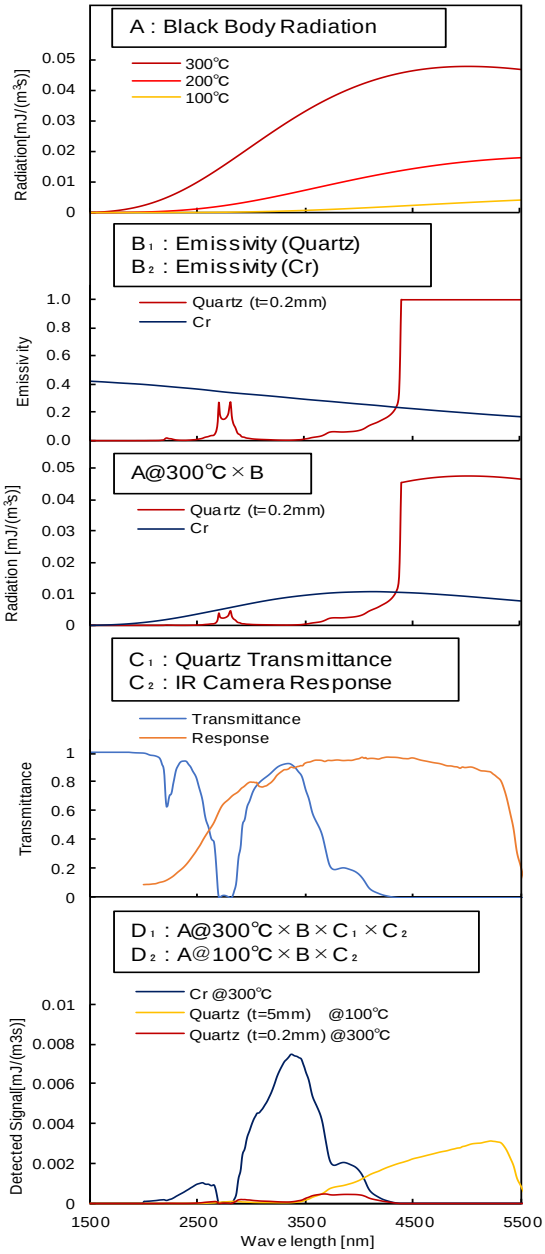


**Figure 63 Calculation of detected signal from IR camera**[118].

Figure 64 shows the example images of the soot luminosity from the side view, the soot luminosity from the front view and the wall IR radiation signal from the front view, respectively. Note that the wall IR radiation images were taken separately from the soot luminosity images, where the side and the front view of soot luminosity were acquired simultaneously with non-coated quartz window. Firstly, it can be observed that the Diesel spray flame exhibit a “donut”-like shape at the center of the image just after the impingement occasion. The luminous flame then spread throughout the entire viewing field with a random pattern corresponding to non-uniform soot

concentration distribution before beginning to disappear starting from the center as the injection period ends. While, from IR radiation images of the chromium layer, it is noted that the appearance and disappearance timing are delayed compared to that of flame luminosity, suggesting that the IR signal is not originating from the background soot radiation but from the thermal radiation of the chromium coating itself. It is interestingly noticed that the IR radiation signal exhibit a "streaky or fiber"-like pattern fluttering towards the radiation direction in a nonuniform-like manner. These streaky patterns width and fluttering movement frequency is observed at a magnitude of 1 mm and 1 ms, respectively. Coincidently, Dejima et al. also measured the same high frequency heat flux fluctuation in engine cylinder wall using MEMS heat flux sensors[116] and the same trends of this streaky fluttering feature is also observed by Kawanabe et al from LES results[113].

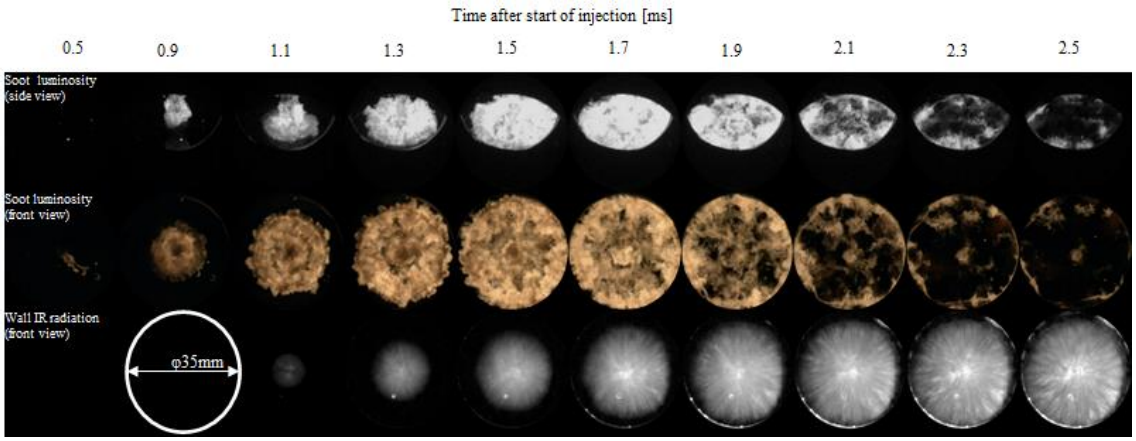


**Figure 64 Example of high-speed images of Diesel spray flame luminosity direct imaging from side-view (top), its front view (middle) and infrared radiation from chromium layer (bottom) in 200 MPa rectangle injection. Ambient conditions: $\rho_a$=23.8 kg/m$^3$, $P_a$=5.0 MPa, $T_a$=1050 K and 17% $O_2$**[118].

Figure 65 shows comparison of chromium layer IR radiation for 175 MPa inversed-delta injection, 175 MPa rectangle injection and 100 MPa rectangle injection respectively at the left, middle and right column in false color scheme for better clarification. Note that the injection mass is similar at 45 mg in all injection profiles and the injection duration is comparable in 175 MPa inversed-delta and 100 MPa rectangle injection cases. As mentioned above, the timing of first IR radiation appearance corresponds to the spray tip arrival or impingement timing, thus earlier appearance is evident in both high 175 MPa injection pressure profiles. High

intensity is observed around the spray axis center prior to being distributed into radial direction afterwards. From 3.0 to 5.0 ms, it can be observed that intense IR radiation signal can be observed in slightly larger area for rectangle injection profiles. While intense IR signal in inversed-delta injection seems to be concentrated more at the center of the viewing field, or at the spray axis. Combining this observation and the combustion recession images shown in Figure 53, lower cooling loss in inversed-delta injection is considered be caused from its smaller following spray momentum and slower spray velocity after the combustion recession event, leading to smaller surface area of high temperature. However, this speculation should be examined further in great detail since the IR image taken here is not corresponded to heat flux observation yet.

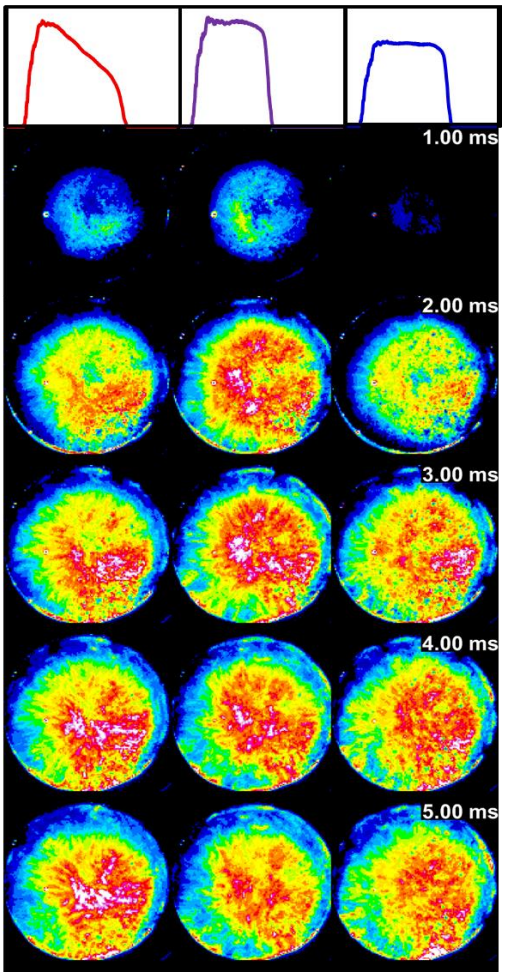


**Figure 65 False color images of Diesel spray flame infrared radiation from chromium layer in 175 MPa inversed-delta (left), 175 MPa rectangle (middle) and 100 MPa rectangle (right) injection profiles. Ambient conditions: $\rho_a$=23.8 kg/m$^3$, $P_a$=5.0 MPa, $T_a$=1050 K and 17% $O_2$.**

Since the IR radiation signal is expected to be originated mainly from the quartz window temperature after being impinged by the Diesel spray flame, detail analysis on the inversed-delta and rectangle injection total wall heat loss amount was estimated based on their corresponding IR radiation signal integration. The measurement area was subjected into two regions: the whole viewing field area at 35-mm-diameter and relatively smaller spray center region at 10-mm diameter where frequent high intensity IR signal was observed in the inversed-delta injection case as shown in Figure 65. Figure 66 shows total wall heat loss for 175 MPa inversed-delta injection, and 175, 100, 200 as well as 160 MPa rectangle injection impinged to the quartz windows at 35-mm-diameter and 10-mm-diameter measurement area on the left and right side, respectively (example images with subjected area measurement indicator are depicted at the top row). In φ35 mm measurement area, the total wall heat loss is higher in rectangle injection profiles compare to that of 175 MPa rectangle injection, except for the very low injection pressure at 100 MPa implying that the cooling loss is suppressed with the inversed-delta injection, leading to the thermal efficiency improvement. Meanwhile for φ10 mm measurement area, the total wall heat loss is initially higher in the rectangle injection profiles compare to that of the inversed-delta injection. It is interestingly noted that the IR radiation signal increases at a faster rate in the inversed-delta injection, reversing the trend with the rectangle injections particularly after approximately 3 ms ASI. However, this data needs to be interpreted with care since the piston is already expanded downward during this period, suggesting that larger wall IR radiation signal alone does not necessarily translates to higher cooling loss in the actual engine. More detail examination is necessary before carrying out the wall heat loss, heat flux and temperature qualitative analysis from this novel optical diagnostics technique.

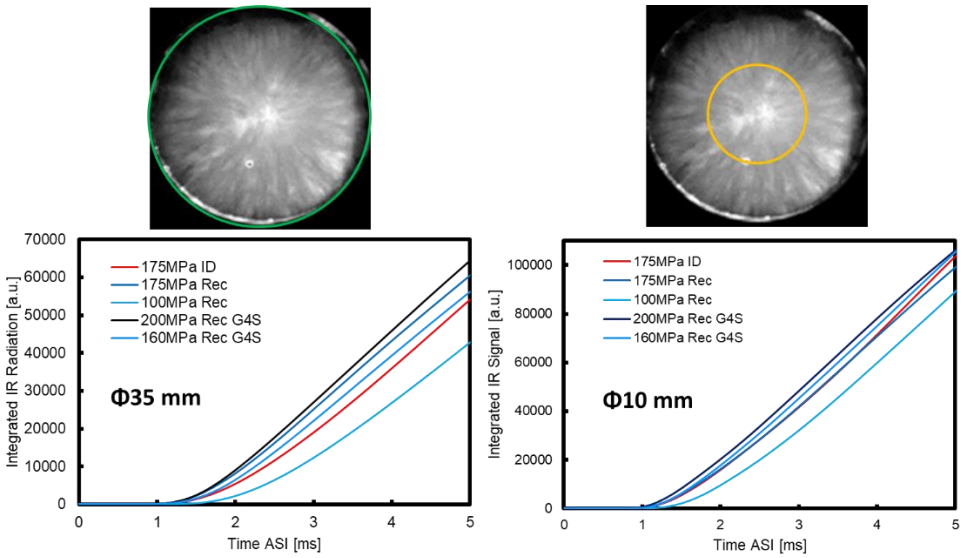


**Figure 66 Example wall IR images (top row) and total wall heat loss based on the wall IR radiation signal integration (bottom row) at 35-mm-diameter (left column) and at 10-mm-diameter (right column). Ambient conditions: $\rho_a$=23.8 kg/m$^3$, $P_a$=5.0 MPa, $T_a$=1050 K and 17% $O_2$.**

## 4.2 Impacts on Emissions

### 4.2.1 Tailpipe Exhaust Emissions

Several injection and combustion strategies were proposed to improve the thermal efficiency such as by ultra-high injection pressure exceeding 300 MPa and wall thermal insulation. Although those approaches did increase the thermal efficiency, its implementation to production vehicle was impeded by the NOx emissions trade-off[52], [53].. With ever stringent emissions standards on top of high fuel efficiency demand, examination on the TAIZAC inversed-delta injection exhaust emissions is imperative.

Figure 67 shows the exhaust NOx and smoke tailpipe emissions from the TAIZAC injector inversed-delta and rectangle injection, where the injection profiles is shown previously in Figure 29. The NOx emissions for both injection profiles is comparable despite of 0.4pt increment in the exhaust loss slightly higher. Meanwhile, it can be observed that the inversed-delta injection smoke emissions is approximately 15% compare to the rectangle injection. Since the absolute value obtained here is relatively low, this magnitude of difference can be can be managed with just the EGR system application, implying no needs for any special measure. Although not exhibited in the chart, the differences in THC and CO emissions for both injection profiles are also not significant[76].

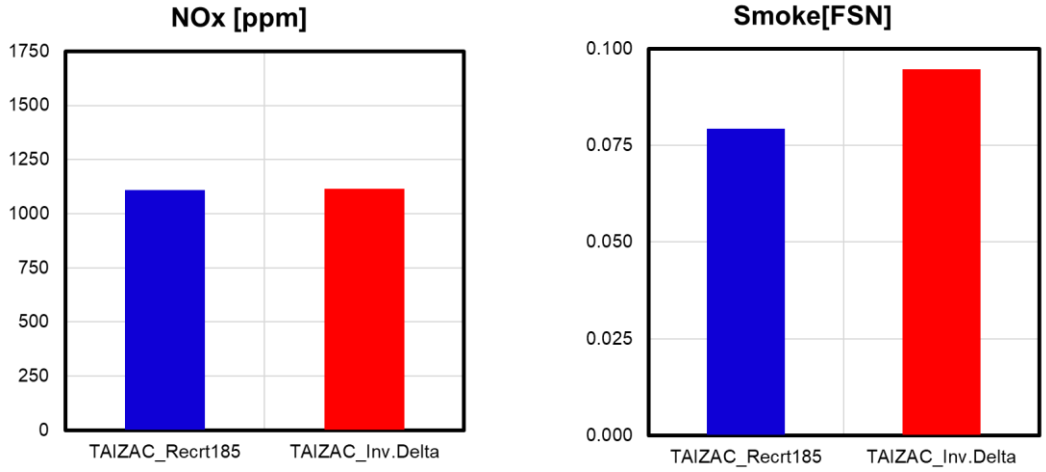


**Figure 67 Tailpipe emissions of NOx (left) and smoke (right) for rectangle and inversed-delta injection**[95]**. Injection rate profile can be referred to Figure 29.**

### 4.2.2 Soot Production Investigation in Constant Volume Combustion Chamber

Although small in terms of absolute value, the smoke emissions increment mechanism in the inversed-delta injection is of interest. By taking advantage of optically accessible CVCC, the study of soot production (i.e. competition between soot formation rate and soot oxidation rate) is performed by applying the Beer-Lambert law from high-speed DBI method using continuous wavelength laser source at 630 mW at 20,000 fps with 0.0875 pixel-to-mm resolution conversion[119], [120]. Table 11 shows the injection profiles, note that high injection mass at 55 mg is performed to study the effects of near-zero EOI pressure reduction, while low injection pressure rectangle injection is performed due to its similar injection period with 175 MPa inversed-delta 45mg injection. The ambient conditions were set similar to the one presented in the combusting conditions presented in Chapter 3. Only the upstream and midstream region of the Diesel spray flame images were acquired (i.e. viewing field from 12.5 mm to 82.5 mm of the spray axial distance) since no significant soot luminosity was observed in Figure 31 shown previously.

**Table 11 Injection conditions for inversed-delta and rectangle injection.**

| Injection Profile | $t_{inj}$ [ms] | $P_{rail}$ [MPa] | $\Delta P_{inj}$ [ms] | Mass [mg] |
|---|---|---|---|---|
| 175 MPa inversed-delta 55mg | 2.35 | 200 | 175 to 0 | 55 |
| 175 MPa inversed-delta 45mg | 1.66 | 200 | 175 to 35 | 45 |
| 175 MPa rectangle 55mg | 1.51 | 175 | 175 | 55 |
| 175 MPa rectangle 45mg | 1.37 | 175 | 175 | 45 |
| 110 MPa rectangle 45mg | 1.66 | 175 | 175 | 45 |

Figure 68 shows the example soot particle DBI high-speed images for 175 MPa inversed-delta injection and 175 MPa rectangle injection at the top and bottom row, respectively for each set of timing at 1.0, 1.5, 2.0, 2.5, 3.0 and 3.5 after the start of injection ASI (as noted at the top right corner). The soot particles structure in Diesel spray flame seems to be similar for both injection profiles at 1.0 ms and 1.5 ms, while the soot onset for the rectangle injection is slightly shifted downstream since the injection was ended at 1.5ms. At 2.0 ms ASI, it is noticed the soot particle shadow at the spray head is wider in the rectangle injection likely due to richer mixture concentrated at the spray head, although the soot optical thickness for both sprays seems to be similar. As mentioned previous in Section 3.3.3, the soot onset recession is apparent in the 175 MPa inversed-delta injection for the timing beyond 2.0 ms ASI, resulting in higher soot particle appearance at the upstream region[40], [90].

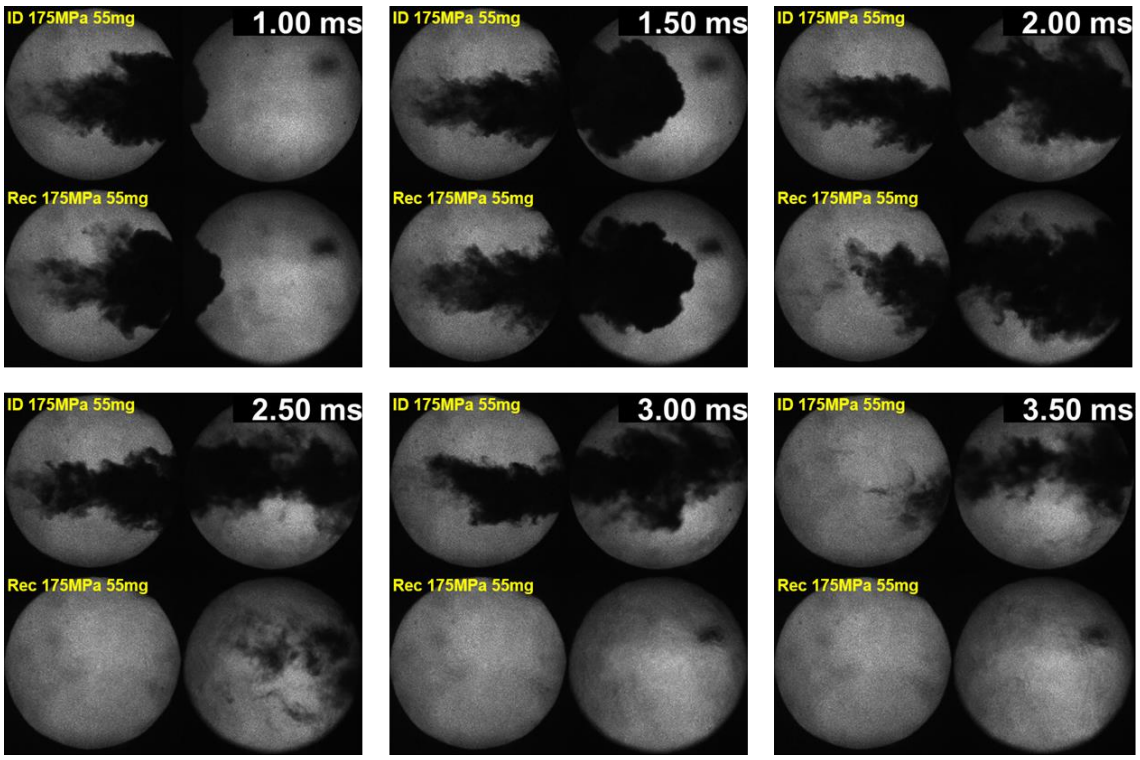


**Figure 68 Example of high-sped images of soot particles in 175 MPa inversed-delta 55mg(top) and 175 MPa rectangle injection(bottom) with timing ASI indicated at top right corner. Ambient conditions: $\rho_a$=23.8 kg/m$^3$, $P_a$=5.0 MPa, $T_a$=1050 K and 17% $O_2$.**

From the general qualitative comparison alone, it is difficult to judge whether the total soot production is increased or decreased in the inversed-delta injection compared to the rectangle injection. For example, higher soot particles seems to be distributed at the upstream region in the inversed-delta injection while the soot

spray seems to be thicker and wider in the rectangle injection. Thus, total extinction area TEA analysis was performed for their qualitative soot production amount comparison. Figure 69 and Figure 70 exhibit the global and regional (i.e. upstream and downstream region) TEA analysis results and their respective subjected area image example (marked by red rectangles), as well as their referral injection rate displayed at the top row. From Figure 69, the inversed-delta injections seem to produce higher total soot particles production compared to that of rectangle injections. However, this data should be interpreted with great care since the soot production is a product of TEA value and time, meaning that larger amount of total soot production could be caused either by higher soot formation rate or lower soot oxidation rate, or both. For example, higher TEA value at a particular timing indicates larger amount of soot formation at "early timing" and slower soot oxidation at "later timing", implying that the temporal information should also be emphasized from the TEA results as well.

From more segregated area of TEA analysis as in Figure 70, it is revealed that the soot formation rate is comparable in both injection profiles since similar TEA value is observed during the main injection period. On the other hand, longer soot residence timing and relatively higher TEA value after the end-of-injection period in the inversed-delta injections suggested that it soot oxidation rate is much slower compare to that of rectangle injection, probably due to insufficient mixing owing to the weaker EOI entrainment waves as mentioned in the previous sections.

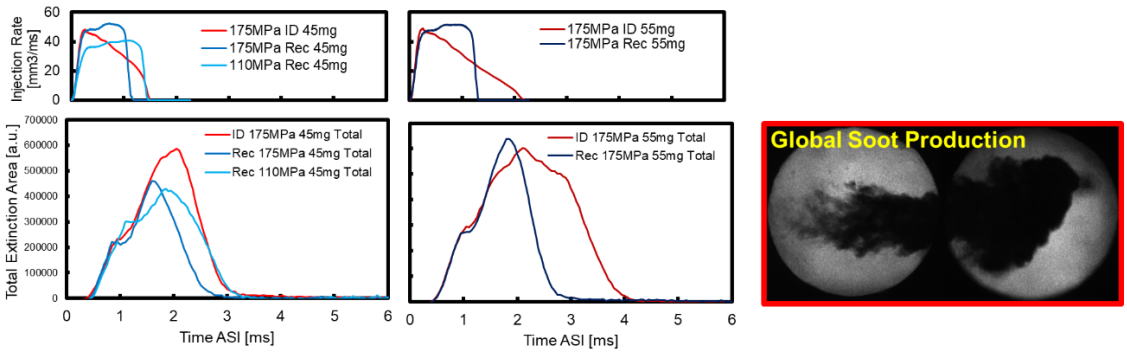


**Figure 69 Injection rate (top row), global total extinction area of soot production (left) and subjected region marked in red rectangle (right). Ambient conditions: $\rho_a$=23.8 kg/m$^3$, $P_a$=5.0 MPa, $T_a$=1050 K and 17% $O_2$.**

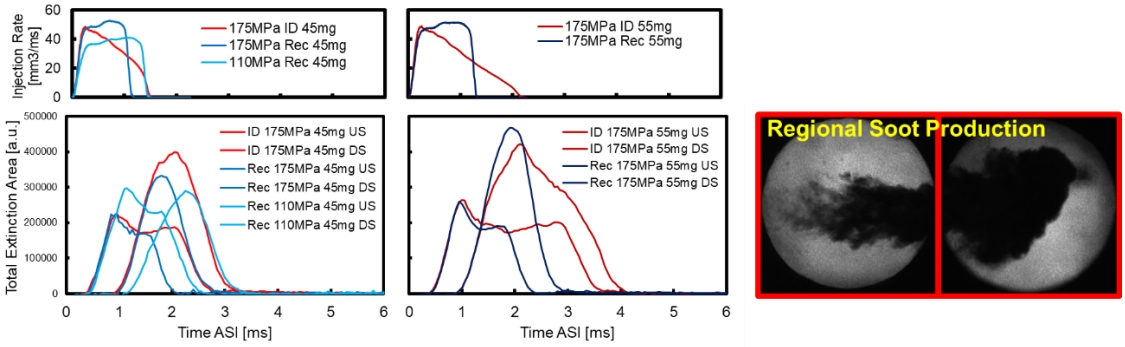


**Figure 70 Injection rate (top row), regional total extinction area of soot production (left) and subjected regions marked in red rectangles (right). Ambient conditions: $\rho_a$=23.8 kg/m$^3$, $P_a$=5.0 MPa, $T_a$=1050 K and 17% $O_2$.**

### 4.3 Summary

A short conclusion for this chapter can be summarized as follows:

1. Inversed-delta injection increases Diesel engine thermal efficiency by 1.0pt compared to rectangle injection at similar initial injection pressure due to significant cooling loss reduction, despite of elongated injection period. Meanwhile, its impact on combustion duration reduction is marginal.
2. IR radiation from chamber wall impinged by rectangle injection diesel spray flame seems to be spread from the center towards the edge. However, in inversed-delta injection, intense IR radiation frequently appears around the center at a smaller area, probably due to its slower following spray momentum and combustion recession event.
3. Inversed-delta injection slightly increases the NOx and smoke tailpipe emissions. Investigation on soot production in CVCC shows that the inversed-delta injection exhibits comparable soot formation rate but slower soot oxidation rate compared to those of the rectangle injection, possibly due to weaker EOI entrainment wave.

# 5 CONCLUSIONS AND RECOMMENDATIONS

This chapter aims to summarize the main conclusions and important contributions of this dissertation. Recommendations for future work will also be provided.

## 5.1 Conclusions

The conclusions of the present study are as follow:

[1] Inversed-delta injection rate shaping was successfully achieved by directly connecting two commercial injectors and controlling their actuation timing. This in-house-developed injection system is called TAndem Injectors Zapping ACtivation: TAIZAC injector.

[2] Inversed-delta injection Diesel spray flame exhibit spray tip rich mixture suppression, shorter tip penetration and more even flame spatial distributions features compared to those of rectangle injection, likely due to its lower following momentum.

[3] Air entrainment per injected fuel amount is expected to be promoted in inversed-delta injection beyond the spray midstream region, probably due to large vortices growth. However, its influence on combustion duration reduction in constant volume combustion chamber and engine test is marginal.

[4] Engine performance test shows that inversed-delta injection reduced cooling loss significantly by 1.3%, results in 1.0% thermal efficiency improvement compare to that of rectangle injection.

[5] High-speed IR thermography of chamber wall impinged by the Diesel spray flame investigation shows that the IR radiation from rectangle injection seems to be spread from the center towards the edge. While, in inversed-delta injection case, intense IR radiation frequently appeared at a smaller area around the spray center even long after the injection event was ended, probably due to its weaker following spray momentum and slower combustion recession.

[6] Smoke emissions increased by approximately 15% in inversed-delta injection compared to that of rectangle injection, likely due to its slower soot oxidation owing to lack of mixing after the end of injection period.

## 5.2 Future Recommendations

The above summarized results of the present study are useful in designing injection rate shaping strategy that can potentially reduce the combustion duration and improve the engine thermal efficiency further.

In near future, firstly investigation on effects of the inversed-delta injection on its overall spray structure, particularly on the large-scale turbulence needs be clarified possibly with ultra-high temporal and spatial resolution optical diagnostics technique. Then, relationship between these local large vortices structure, air entrainment and heat release rate promotion need to be investigated, and simple numerical model needs to be developed based on the experimental data.

With better understanding, optimization of injection rate shaping for rapid combustion concept and its necessary hardware needs to be proposed and developed: for example, more aggressive inversed-delta ramp-down slope and after-injection mixing pulse strategy.

# REFERENCES


[1] European environment agency, "Recent trends and projections in EU greenhouse gas emissions," pp. 1–9, 2018.

[2] European Union, "Worldwide Emission Standards and Related Regulations - Passenger Cars / Light and Medium Duty Vehicles. May 2019," *Cont. Futur. Motion*, no. May, p. 210 pages, 2019.

[3] F. Leach, R. Ismail, M. Davy, A. Weall, and B. Cooper, "The effect of a stepped lip piston design on performance and emissions from a high-speed diesel engine," *Appl. Energy*, vol. 215, no. February, pp. 679–689, 2018.

[4] "Innovative combustion technology: Cross-ministerial Strategic Innovation Promotion Program (SIP)." [Online]. Available: https://www.jst.go.jp/sip/k01.html. [Accessed: 01-Apr-2019].

[5] J. O'Connor and M. Musculus, "Optical Investigation of the Reduction of Unburned Hydrocarbons Using Close-Coupled Post Injections at LTC Conditions in a Heavy-Duty Diesel Engine," *SAE Int. J. Engines*, vol. 6, no. 1, pp. 379–399, 2013.

[6] J. O'Connor and M. Musculus, "Post Injections for Soot Reduction in Diesel Engines: A Review of Current Understanding," *SAE Int. J. Engines*, vol. 6, no. 1, pp. 400–421, 2013.

[7] J. B. Heywood, "Internal Combustion Engine Fundamentals." McGraw-Hill Publishing, New York, NY, 1988.

[8] P. F. Flynn *et al.*, "Diesel combustion: An integrated view combining laser diagnostics, chemical kinetics, and empirical validation," *SAE Tech. Pap. Ser.*, no. 1999-01–0509, pp. 1–13, 1999.

[9] H. Kosaka, T. Aizawa, and T. Kamimoto, "Two-dimensional imaging of ignition and soot formation processes in a diesel flame," *Int. J. Engine Res.*, vol. 6, no. 1, pp. 21–42, 2005.

[10] X. Wang, Z. Huang, O. A. Kuti, W. Zhang, and K. Nishida, "Experimental and analytical study on biodiesel and diesel spray characteristics under ultra-high injection pressure," *Int. J. Heat Fluid Flow*, vol. 31, no. 4, pp. 659–666, 2010.

[11] Y. Zhang, S. Li, W. Qi, and K. Nishida, "Evaporation characterization of fuel spray impinging on a flat wall by laser-based measurement," *Int. J. Engine Res.*, vol. 18, no. 8, pp. 776–784, 2017.

[12] G. Bruneaux, "Mixing process in high pressure diesel jets by normalized laser induced exciplex fluorescence Part I: Free jet," *SAE Tech. Pap. Ser.*, no. 2005-

01–2097, 2005.

[13] G. Bruneaux, M. Causse, and A. Omrane, “Air Entrainment in Diesel-Like Gas Jet by Simultaneous Flow Velocity and Fuel Concentration Measurements, Comparison of Free and Wall Impinging Jet Configurations,” *SAE Int. J. Engines*, vol. 5, no. 2, pp. 76–93, 2011.

[14] Y. Wakuri, M. Fujii, and T. Amitani, “Studies on the Penetration of Fuel Spray in a Diesel Engine,” *Bull. JSME*, vol. 3, no. 9, pp. 123–130, 1960.

[15] R. Gramlich *et al.*, “Air Entrainment and Momentum Distribution in the Near Field of Diesel Sprays from Group Hole Nozzles,” in *27th ILASS Europe 2016, Brighton, UK, September 4-7*, 2016.

[16] S. Riess, L. Weiss, A. Peter, J. Rezaei, and M. Wensing, “Air entrainment and mixture distribution in Diesel sprays investigated by optical measurement techniques,” *Int. J. Engine Res.*, vol. 19, no. 1, pp. 120–133, 2018.

[17] R. Payri, J. Gimeno, M. Bardi, and A. Plazas, “Effect of Injection Rate Shaping Over Diesel Spray Development in Non Reacting Evaporative Conditions,” in *Proceedings of the ASME 2012, Torino, Piemonte, Italy, May 6-9*, 2012, no. ICES2012-81206.

[18] J. M. Desantes, J. M. García-Oliver, T. Xuan, and W. Vera-Tudela, “A study on tip penetration velocity and radial expansion of reacting diesel sprays with different fuels,” *Fuel*, vol. 207, pp. 323–335, 2017.

[19] C. A. Idicheria and L. M. Pickett, “Soot formation in diesel combustion under high-EGR conditions,” *SAE Tech. Pap. Ser.*, no. 2005-01–3834, pp. 1–16, 2005.

[20] R. Payri, J. M. García-Oliver, M. Bardi, and J. Manin, “Fuel temperature influence on diesel sprays in inert and reacting conditions,” *Appl. Therm. Eng.*, vol. 35, no. 1, pp. 185–195, 2012.

[21] J. D. Naber and D. L. Siebers, “Effects of gas density and vaporization on penetration and dispersion of diesel sprays,” *SAE Tech. Pap. Ser.*, no. 960034, pp. 1–30, 1996.

[22] D. L. Siebers, “Scaling liquid-phase fuel penetration in diesel sprays based on mixing-limited vaporization,” *SAE Tech. Pap. Ser.*, no. 1999-01–0528, pp. 1–26, 1999.

[23] D. Siebers, B. Higgins, and L. Pickett, “Flame lift-Off on direct-injection diesel fuel jets：Oxygen concentration effects,” *SAE Tech. Pap. Ser.*, no. 2002-01–0890, 2002.

[24] D. L. Siebers and B. Higgins, “Flame lift-off on direct-injection diesel sprays under quiescent conditions,” *SAE Tech. Pap. Ser.*, no. 2001-01–0530, 2001.

[25] C. A. Idicheria and L. M. Pickett, “Formaldehyde Visualization Near Lift-off Location in a Diesel Jet,” *SAE Tech. Pap. Ser.*, no. 2006-01–3434, pp. 1–13, 2006.

[26] S. Kook, L. M. Pickett, and M. P. B. Musculus, “Influence of diesel injection parameters on end-of-injection liquid length recession,” *SAE Int. J. Engines*, vol. 2, no. 1, pp. 1194–1210, 2009.

[27] N. Horibe, Z. Bao, T. Taguchi, K. Egoshi, H. Kawanabe, and T. Ishiyama, “Improvement of Thermal Efficiency in a Diesel Engine with High-Pressure Split Main Injection,” *SAE Tech. Pap. Ser.*, no. 2018-01–1791, pp. 1–11, 2018.

[28] J. M. Desantes, J. M. García-Oliver, A. García, and T. Xuan, “Optical study on characteristics of non-reacting and reacting diesel spray with different strategies of split injection,” *Int. J. Engine Res.*, vol. 20, no. 6, pp. 606–623, 2018.

[29] N. Maes, P. C. Bakker, N. Dam, and B. Somers, “Transient Flame Development in a Constant-Volume Vessel Using a Split-Scheme Injection Strategy,” *SAE Int. J. Fuels Lubr.*, vol. 10, no. 2, 2017.

[30] A. A. Moiz, M. M. Ameen, S. Y. Lee, and S. Som, “Study of soot production for double injections of n-dodecane in CI engine-like conditions,” *Combust. Flame*, vol. 173, pp. 123–131, 2016.

[31] M. P. B. Musculus, T. Lachaux, L. M. Pickett, and C. A. Idicheria, “End-of-injection over-mixing and unburned hydrocarbon emissions in low-temperature- combustion diesel engines,” *SAE Tech. Pap. Ser.*, no. 2007-01–0907, pp. 1–27, 2007.

[32] M. P. B. Musculus, P. C. Miles, and L. M. Pickett, “Conceptual models for partially premixed low-temperature diesel combustion,” *Prog. Energy Combust. Sci.*, vol. 39, pp. 246–283, 2013.

[33] M. P. B. Musculus and K. Kattke, “Entrainment waves in diesel jets,” *SAE Int. J. Engines*, vol. 2, no. 1, pp. 1170–1193, 2009.

[34] M. P. B. Musculus, “Entrainment waves in decelerating transient turbulent jets,” *J. Fluid Mech.*, vol. 638, pp. 117–140, 2009.

[35] W. E. Eagle, M. P. B. Musculus, L.-M. C. Malbec, and G. Bruneaux, “Measuring transient entrainment rates of a confined vaporizing diesel jet,” in *ILASS Americas, 26th Annual Conference on Liquid Atomization and Spray Systems, Portland, Oregon, USA, May*, 2014.

[36] S. Kook, L. M. Pickett, M. P. B. Musculus, K. Kattke, and R. K. Gehmlich, “Liquid-phase diesel spray penetration during end-of-injection transient,” in

*The Seventh International Conference on Modeling and Diagnostics for Advanced Engine Systems COMODIA 2008, Sapporo, Japan, July 28-31*, 2008, pp. 413–420.

[37] B. W. Knox, C. L. Genzale, L. M. Pickett, J. M. Garcia-oliver, and W. Vera-tudela, "Combustion Recession after End of Injection in Diesel Sprays," *SAE Int. J. Engines*, no. 2015-01–0797, pp. 1–17, 2015.

[38] B. Knox and C. Genzale, "Effects of end-of-injection transients on combustion recession in diesel sprays," *SAE Int. J. Engines*, no. 2016-01–0745, pp. 1–18, 2016.

[39] B. W. Knox and C. L. Genzale, "Scaling combustion recession after end of injection in diesel sprays," *Combust. Flame*, vol. 177, pp. 24–36, 2017.

[40] W. Morrison, C. Koci, T. Bazyn, G. Martin, C. Gehrke, and K. Svensson, "The Influence of Diesel End-of-Injection Rate Shape on Combustion Recession," *SAE Int. J. Engines*, vol. 8, no. 2, pp. 647–659, 2015.

[41] H. Juneja, Y. Ra, and R. D. Reitz, "Optimization of injection ratesShape using active control of fuel injection," *SAE Tech. Pap. Ser.*, no. 2004-01–0530, pp. 1–18, 2004.

[42] Y. Wakisaka and A. Azetsu, "Effects of Fuel Injection Rate and Injection Pressure on Intermittenton Intermittent Spray Combustion," *SAE Tech. Pap. Ser.*, vol. 1, no. 2793, 2000.

[43] Y. Wakisaka and A. Azetsu, "Effects of fuel injection rate shaping on combustion and emission formation in intermittent spray," *SAE Tech. Pap. Ser.*, no. 2002-01–1159, 2002.

[44] V. Macian, R. Payri, S. Ruiz, M. Bardi, and A. H. Plazas, "Experimental study of the relationship between injection rate shape and Diesel ignition using a novel piezo-actuated direct-acting injector," *Appl. Energy*, vol. 118, pp. 100–113, 2014.

[45] R. Payri, J. Gimeno, J. P. Viera, and A. H. Plazas, "Needle lift profile influence on the vapor phase penetration for a prototype diesel direct acting piezoelectric injector," *Fuel*, vol. 113, pp. 257–265, 2013.

[46] R. Payri, J. Gimeno, M. Bardi, and A. H. Plazas, "Study liquid length penetration results obtained with a direct acting piezo electric injector," *Appl. Energy*, vol. 106, pp. 152–162, 2013.

[47] J. M. Desantes, J. Benajes, S. Molina, and C. A. González, "The modification of the fuel injection rate in heavy-duty diesel engines Part 2: Effects on combustion," *Appl. Therm. Eng.*, vol. 24, no. 17–18, pp. 2715–2726, 2004.

[48] J. M. Desantes, J. Benajes, S. Molina, and C. A. González, "The modification of the fuel injection rate in heavy-duty diesel engines. Part 1: Effects on engine performance and emissions," *Appl. Therm. Eng.*, vol. 24, no. 17–18, pp. 2701–2714, 2004.

[49] L. M. Pickett and D. L. Siebers, "Orifice diameter effects on diesel fuel jet flame structure," *J. Eng. Gas Turbines Power*, vol. 127, p. 187, 2005.

[50] D. Farrace *et al.*, "A progress review on soot experiments and modeling in the Engine Combustion Network (ECN)," *SAE Int. J. Engines*, vol. 9, no. 2, 2016.

[51] K. Nishida, J. Zhu, X. Leng, and Z. He, "Effects of micro-hole nozzle and ultra-high injection pressure on air entrainment, liquid penetration, flame lift-off and soot formation of diesel spray flame," *Int. J. Engine Res.*, vol. 18, no. 1–2, pp. 1–16, 2017.

[52] N. Nishikawa *et al.*, "Thermo-swing wall insulation technology; - A novel heat Loss reduction approach on engine combustion chamber -," *SAE Tech. Pap. Ser.*, vol. 1, 2016.

[53] N. Uchida and T. Okamoto, "Simultaneous Improvements in Thermal Efficiency and Exhaust Emissions in a Heavy-duty Diesel Engine by Utilizing Newly Designed Multiple Injectors System," in *Conference on Thermo- and Fluid Dynamic Processes in Direct Injection Engines THIESEL 2016, Valencia, Spain, September 13-16*, 2016.

[54] K. Kondo, K. Sakai, and T. Aizawa, "High-Speed Simultaneous Imaging of UV-Chemiluminescence, UV-Absorption and Flame Luminosity during Late Combustion in a Diesel Spray Flame," *Int. Combust. Engine Symp. Tokyo, Japan, December 5-7*, 2016.

[55] T. Adachi, B. Zhou, J. Kusaka, and T. Aizawa, "Numerical analysis on temporal and spatial distribution of equivalence ratio and heat release rate in diesel spray combustion by using LES coupled with detailed chemistry," in *JSAE Spring Congress, Yokohama, Japan, May 23-25*, 2018.

[56] H. Naohiro *et al.*, "High-Speed Imaging of UV-Chemiluminescence during Late Combustion in a Multi-Cylinder Diesel Engine," *Int. Combust. Engine Symp. Tokyo, Japan, December 5-7*, no. 23, pp. 1–8, 2016.

[57] N. Hasegawa *et al.*, "Analysis of heat release process during late combustion in a diesel engine," *JSAE Trans.*, vol. 49, no. 3, pp. 581–589, 2018.

[58] Y. Zama, W. Ochiai, T. Furuhata, and M. Arai, "Velocity measurement inside a diesel spray by using time-resolved PIV under high ambient density condition," in *12th Triennial International Conference on Liquid Atomization*

*and Spray Systems ICLASS 2012, Heidelberg, Germany, September 2-6*, 2012.

[59] Y. Zama, W. Ochiai, T. Furuhata, and M. Arai, "Velocity distribution inside a diesel spray under high ambient density condition," in *The Eight International Conference on Modeling and Diagnostics for Advanced Engine System COMODIA 2012, Fukuoka, Japan, July 23-26*, 2012.

[60] M. Arai, "Physics behind Diesel Sprays," in *12th Triennial International Conference on Liquid Atomization and Spray Systems ICLASS 2012, Heidelberg, Germany, September 2-6*, 2012.

[61] L. M. Pickett, S. Kook, and T. C. Williams, "Visualization of Diesel Spray Penetration, Cool-Flame, Ignition, High-Temperature Combustion, and Soot Formation Using High-Speed Imaging," *SAE Int. J. Engines*, vol. 2, no. 1, pp. 439–459, 2010.

[62] M. Arai, "Diesel Spray Behaviour and Air Entrainment," *J. Nanosci. Nanotechnol. Appl.*, vol. 2, no. 1, pp. 1–17, 2018.

[63] N. Maes *et al.*, "Characterization of Spray A flame structure for parametric variations in ECN constant-volume vessels using chemiluminescence and laser-induced fluorescence," *Combust. Flame*, vol. 174, pp. 138–151, 2016.

[64] J. Dahlstrom, O. Andersson, M. Tuner, and H. Persson, "Experimental Comparison of Heat Losses in Stepped-Bowl and Re-Entrant Combustion Chambers in a Light Duty Diesel Engine," *SAE Tech. Pap. Ser.*, vol. 1, 2016.

[65] T. Aizawa, Y. Toyama, S. Akiyama, M. Fareez, E. Soshu, and S. Taizo, "Inversed-Delta-Injected Diesel Spray Flame via Simultaneous UV-Chemiluminescence, UV-Absorption and Flame Luminosity High-Speed Imaging," *JSAE Spring, Yokohama, Japan, May 23-25*, no. 22, pp. 1–8, 2018.

[66] L.-M. Malbec, C. Angelberger, F. Tagliante, G. Bruneaux, and L. M. Pickett, "Experimental study of the stabilization mechanism of a lifted Diesel-type flame using combined optical diagnostics and laser-induced plasma ignition," *Combust. Flame*, vol. 197, pp. 215–226, 2018.

[67] C. A. Idicheria and L. M. Pickett, "Quantitative Mixing Measurements in a Vaporizing Diesel Spray by Rayleigh Imaging," *SAE Tech. Pap. Ser.*, vol. 1, no. 647, 2007.

[68] L. M. Pickett *et al.*, "Relationship between diesel fuel spray vapor penetration/dispersion and local fuel mixture fraction," *SAE Int. J. Engines*, vol. 4, no. 1, pp. 764–799, 2011.

[69] R. Payri, F. J. Salvador, J. Manin, and A. Viera, "Diesel ignition delay and lift-off length through different methodologies using a multi-hole injector," *Appl.*

*Energy*, vol. 162, pp. 541–550, 2016.

[70] T. Aizawa, M. F. E. Bin Abdullah, A. Inoue, Y. Ishidzuka, N. Taki, and H. Kosaka, "Aromatic additive effects on soot formation in a fischer-tropsch diesel (FTD) spray flame via laser spectroscopy," *Eight Int. Conf. Model. Diagnostics Adv. Engine Syst. COMODIA 2012, Fukuoka, Japan, July 23-26*, no. EE1-3, pp. 275–280, 2012.

[71] "Engine Combustion Network | Diesel Spray Combustion." [Online]. Available: https://ecn.sandia.gov/diesel-spray-combustion/. [Accessed: 12-Apr-2019].

[72] M. Bardi *et al.*, "Engine Combustion Network: Comparison of Spray Development, Vaporization, and Combustion in Different Combustion Vessels," *At. Sprays*, vol. 22, no. 10, pp. 807–842, 2013.

[73] T. Aizawa, T. Harada, K. Kondo, T. Adachi, B. Zhou, and J. Kusaka, "Thermocouple temperature measurements in diesel spray flame for validation of in-flame soot formation dynamics," *Int. J. Engine Res.*, vol. 18, no. 5–6, pp. 453–466, 2016.

[74] S. Akiyama, Y. Toyama, S. Saruwatari, T. Shimada, Y. Noguchi, and T. Aizawa, "TAIZAC -TAndem Injectors Zapping ACtivation- towards thermal efficiency improvement of diesel engine," *Trans. Soc. Automot. Eng. Japan*, vol. 50, no. 2, pp. 279–284, 2019.

[75] S. Saruwatari *et al.*, "Design and Development of Rate Shaping Injectors towards Reduction of Late Combustion in Diesel Spray Flame," in *JSAE Kanto Branch Symposium, Tokyo, Japan, March 8*, 2017, pp. 1–3.

[76] T. Aizawa *et al.*, "TAIZAC -TAndem Injectors Zapping ACtivation- for thermal efficiency improvement of diesel engine," *SAE Tech. Pap.*, vol. 2019-01–21, 2019.

[77] M. F. E. Abdullah *et al.*, "Optical diagnostics of inversed-delta rate shaping diesel spray flame towards reduction of late combustion," *SAE Tech. Pap.*, no. 2018-01–1793, pp. 1–13, 2018.

[78] N. Kurimoto, S. Park, S. Moon, Y. Gao, J. Wang, and Y. Nishijima, "Effect of the number and position of nozzle holes on in- and near-nozzle dynamic characteristics of diesel injection," *Fuel*, vol. 150, pp. 112–122, 2015.

[79] W. Huang, S. Moon, and K. Ohsawa, "Near-nozzle dynamics of diesel spray under varied needle lifts and its prediction using analytical model," *Fuel*, vol. 180, pp. 292–300, 2016.

[80] R. Payri, F. J. Salvador, J. Gimeno, and L. D. Zapata, "Diesel nozzle geometry

influence on spray liquid-phase fuel penetration in evaporative conditions," *Fuel*, vol. 87, no. 7, pp. 1165–1176, 2008.

[81] J. M. Desantes, R. Payri, F. J. Salvador, and J. Gimeno, "Measurements of Spray Momentum for the Study of Cavitation in Diesel Injection Nozzles," *SAE Tech. Pap. Ser.*, no. 2003-01–0703, 2003.

[82] R. Payri, J. M. García, F. J. Salvador, and J. Gimeno, "Using spray momentum flux measurements to understand the influence of diesel nozzle geometry on spray characteristics," *Fuel*, vol. 84, no. 5, pp. 551–561, 2005.

[83] L. Postrioti, F. Mariani, and M. Battistoni, "Experimental and numerical momentum flux evaluation of high pressure Diesel spray," *Fuel*, vol. 98, pp. 149–163, 2012.

[84] T. Kenichi, T. Naoki, and I. Masato, "Using the Diesel Spray Momentum Measurement to Analyze the Wall Impinging Spray Behavior," in *I25th ILASS Symposium, Toyama, Japan, December 19-20*, 2016.

[85] B. W. Knox, "End-of-Injection Effects on Diesel Spray Combustion (Doctoral Dissertation)," 2016.

[86] H. Ge *et al.*, "A comparison of computational fluid dynamics predicted initial liquid penetration using rate of injection profiles generated using two different measurement techniques," *Int. J. Engine Res.*, vol. 20, no. 2, pp. 226–235, 2019.

[87] K. Kondo, M. Kuribayashi, K. Sakai, and T. Aizawa, "High-speed ultraviolet chemiluminescence imaging of late combustion in diesel spray flame," *Int. J. Engine Res.*, vol. 18, no. 1–2, pp. 93–104, 2017.

[88] L. M. Pickett and D. L. Siebers, "Soot in diesel fuel jets: Effects of ambient temperature, ambient density, and injection pressure," *Combust. Flame*, vol. 138, no. 1–2, pp. 114–135, 2004.

[89] J. Manin, M. Bardi, and L. M. Pickett, "Evaluation of the liquid length via diffused back-illumination imaging in vaporizing diesel sprays," in *The Proceedings of the International symposium on diagnostics and modeling of combustion in internal combustion engines*, 2012, pp. 665–673.

[90] M. Fareez, S. Akiyama, T. Kinoshita, and T. Aizawa, "Effects of inversed-delta injection rate shaping on diesel spray flame liquid length , lift-off length and soot onset," *Fuel*, vol. 258, no. 116170, 2019.

[91] U. Azimov, N. Kawahara, E. Tomita, and K. Tsuboi, "Evaluation of the flame lift-off length in diesel spray combustion based on flame extinction," *J. Therm. Sci. Technol.*, vol. 5, no. 2, pp. 238–251, 2010.

[92] J. V. Pastor, J. Javier López, J. M. García, and J. M. Pastor, "A 1D model for

the description of mixing-controlled inert diesel sprays," *Fuel*, vol. 87, no. 13–14, pp. 2871–2885, 2008.

[93] J. M. Desantes, J. V. Pastor, J. M. García-Oliver, and J. M. Pastor, "A 1D model for the description of mixing-controlled reacting diesel sprays," *Combust. Flame*, vol. 156, no. 1, pp. 234–249, 2009.

[94] W. E. Eagle, M. P. B. Musculus, L.-M. C. Malbec, and G. Bruneaux, "Measuring transient entrainment rates of a confined vaporizing diesel jet," in *ILASS Americas, 26th Annual Conference on Liquid Atomization and Spray Systems, Portland, Oregon, USA, May*, 2014.

[95] Y. Maruyama *et al.*, "Effects of inversed-delta injection using TAIZAC injector on Diesel engine performance," in *30th Internal Combustion Engine Sysposium, Hiroshima, Japan, December 10-12*, 2019.

[96] J. M. Desantes, J. V. Pastor, J. M. García-Oliver, and F. J. Briceño, "An experimental analysis on the evolution of the transient tip penetration in reacting Diesel sprays," *Combust. Flame*, vol. 161, no. 8, pp. 2137–2150, 2014.

[97] H. Johari and R. Paduano, "Dilution and mixing in an unsteady jet," *Exp. Fluids*, vol. 23, no. 4, pp. 272–280, 1997.

[98] M. F. E. Abdullah, Y. Toyama, S. Saruwatari, S. Akiyama, T. Shimada, and T. Aizawa, "Spray Tip Penetration of Inversed-delta Injection Rate Shaping in Non-Vapourising Condition," *Int. J. Automot. Mech. Eng.*, vol. 16, no. 3, pp. 7048–7060, 2019.

[99] H. Hiroyasu and M. Arai, "Structures of Fuel Sprays in Diesel Engines," *SAE Tech. Pap. Ser.*, no. 900475, 1990.

[100] M. Fareez, E. Bin, S. Akiyama, T. Kinoshita, and T. Shimada, "Investigation of inversed-delta injection rate shaping diesel spray flame structure and combustion characteristics towards thermal efficiency improvement," *Appl. Therm. Eng.*, vol. 160, no. 113986, 2019.

[101] M. Lauer, M. Zellhuber, T. Sattelmayer, and C. J. Aul, "Determination of the Heat Release Distribution in Turbulent Flames by a Model Based Correction of OH∗ Chemiluminescence," *J. Eng. Gas Turbines Power*, vol. 133, no. 12, p. 121501, 2011.

[102] P. H. Paul and H. N. Najm, "Planar laser-induced fluorescence imaging of flame heat release rate," *Symp. Combust.*, vol. 27, no. 1, pp. 43–50, 1998.

[103] H. N. Najm, P. H. Paul, C. J. Mueller, and P. S. Wyckoff, "On the Adequacy of Certain Experimental Observables as Measurements of Flame Burning Rate," *Combust. Flame*, vol. 113, no. 3, pp. 312–332, 2002.

[104] S. Singh, M. P. B. Musculus, and R. D. Reitz, "Mixing and flame structures inferred from OH-PLIF for conventional and low-temperature diesel engine combustion," *Combust. Flame*, vol. 156, pp. 1898–1908, 2009.

[105] S. Singh and M. P. B. Musculus, "Numerical Modeling and Analysis of Entrainment in Turbulent Jets After the End of Injection," *J. Fluids Eng.*, vol. 132, no. 8, p. 81203, 2010.

[106] S. L. Kokjohn and R. D. Reitz, "Investigation of the Roles of Flame Propagation, Turbulent Mixing, and Volumetric Heat Release in Conventional and Low Temperature Diesel Combustion," *J. Eng. Gas Turbines Power*, vol. 133, pp. 1–10, 2011.

[107] L. M. Pickett, D. L. Siebers, and C. A. Idicheria, "Relationship between ignition processes and the lift-off length of diesel fuel jets," *SAE Tech. Pap. Ser.*, no. 2005-01–3843, pp. 1–18, 2005.

[108] X. Wang, O. A. Kuti, W. Zhang, K. Nishida, and Z. Huang, "Effect of injection pressure on spray flame characteristics and combustion of biodiesel fuel injected by common rail injection system," *Combust. Sci. Technol.*, vol. 182, no. 10, pp. 1369–1390, 2010.

[109] X. Wang, Z. Huang, O. A. Kuti, W. Zhang, and K. Nishida, "An experimental investigation on spray, ignition and combustion characteristics of biodiesels," *Proc. Combust. Inst.*, vol. 33, no. 2, pp. 2071–2077, 2011.

[110] D. Jarrahbashi, S. Kim, B. W. Knox, and C. L. Genzale, "Computational analysis of end-of-injection transients and combustion recession," *Int. J. Engine Res.*, vol. 18, no. 10, pp. 1088–1110, 2017.

[111] Y. Nishikawa, K. Uematsu, Y. Maruyama, S. Saruwatari, T. Shimada, and T. Aizawa, "Effects of fuel pressure modulation among/during multi injection pulses on diesel engine performance using TAIZAC injector," in *29th Internal Combustion Engine Sysposium, Kyoto, Japan, November 26-28*, 2018.

[112] B. Hu, M. P. B. Musculus, and J. C. Oefelein, "The influence of large-scale structures on entrainment in a decelerating transient turbulent jet revealed by large eddy simulation The influence of large-scale structures on entrainment in a decelerating transient turbulent jet revealed by large eddy simu," *Phys. Fluids*, vol. 24, no. 45106, pp. 1–17, 2012.

[113] H. Kawanabe, J. Komae, and T. Ishiyama, "Analysis of flow and heat transfer during the impingement of a diesel spray on a wall using large eddy simulation," *Int. J. Engine Res.*, vol. 20, no. 7, 2018.

[114] T. Hori, K. Fujiwara, M. Tsubokura, K. Kuwahara, E. Matsumura, and J.

Senda, “Three-dimensional simulation of heat transfer in dieselspray flame impinging on flat wall using skeletal mechanism of n-tridecane,” in *The Ninth International Conference on Modeling and Diagnostics for Advanved Engine Systems COMODIA 2017, Okayama, Japan, July 25-28*, 2017.

[115] Y. Harada *et al.*, “Wall heat transfer of unsteady near-wall flow in internal combustion engines,” *Int. J. Engine Res.*, vol. 20, no. 7, pp. 817–833, 2019.

[116] K. Dejima, O. Nakabeppu, Y. Nakamura, T. Tsuchiya, and K. Nagasaka, “Three-point MEMS heat flux sensor for turbulent heat transfer measurement in internal combustion engines,” *Int. J. Engine Res.*, vol. 20, no. 7, pp. 696–705, 2018.

[117] T. Tatsumi, S. Maeda, M. Nakata, Y. , Kobashi, E. Matsumura, and J. Senda, “A Study on the Wall Heat Loss from Diesel Spray Flame (Fourth Report),” *Trans. Soc. Automot. Eng. Japan*, vol. 49, no. 2, pp. 144–149, 2018.

[118] T. Kinoshita, S. Akiyama, K. Shinohara, Y. Miyagawa, and T. Aizawa, “Infrared high-speed imaging of radiation from combustion chamber wall impinged diesel spray flame,” in *30th Internal Combustion Engine Sysposium, Hiroshima, Japan, December 10-12*, 2019.

[119] T. Yamaguchi, K. Kondo, H. Nishigai, S. Takano, and T. Aizawa, “Direct Sampling, TEM Analysis and Optical Measurement of Soot Particles at Different Axial Locations in a Transient Spray Flame,” *SAE Int. J. Fuels Lubr.*, vol. 5, no. 1, pp. 316–328, 2012.

[120] H. Nishigai, K. Kondo, T. Yamaguchi, and T. Aizawa, “Morphology of JIS#2 and Fischer-Tropsch Diesel (FTD) soot in spray flames via transmission electron microscopy (TEM),” in *The Eight International Conference on Modeling and Diagnostics for Advanced Engine System COMODIA 2012, Fukuoka, Japan, July 23-26*, 2012, pp. 464–469.

# APPENDICES

## Investigation of Air Entrainment in Inversed-delta and Rectangle Injection Based on One-dimensional 1D Simulation

Previously, it was reported that the inversed-delta injection exhibits longer time for liquid fuel vaporization, slower combustion recession event and lower rate of soot oxidation compare to those of the rectangle injection, particularly after the end of injection EOI period. It is assumed that these observations are due to the weaker and slower air entrainment waves due to the lower inversed-delta EOI injection pressure. To examine the air entrainment characteristics in the inversed-delta and rectangle injection, simple 1D simulation as adopted previously was applied and the results are displayed in Figure A1. Note that the amount of air entrainment is better expressed with respect to the injected fuel amount as shown by the axially mean equivalence ratio, and with respect to the ratio of the air entrainment amount in a steady jet case, refer to the top row. Middle row shows the spray cross-sectioned equivalence ratio distributions, and the bottom row shows the injection velocity at the nozzle orifice which indicates the injection rate shaping as well as the corresponded spray tip penetration. The timing at 0.86 ms and 1.90 ms ASI was selected to represent those spray characteristics during the injection and after the injection period.

Similar to our expectations, air entrainment per fuel injected amount is promoted in the inversed-delta injection during the injection period as can be observed by local peak at the spray downstream region compare to that of the rectangle injection (i.e. flat horizontal line at unity value implies similar air entrainment amount as in the steady jet condition). However, after the injection period was ended, the air entrainment is highly promoted in the rectangle injection approaching the factor of three, while weaker and narrower region of air entrainment can be observed for the inversed-delta injection. It can be concluded that, although the air entrainment is progressively promoted in the inversed-delta injection during the injection period, its EOI entrainment waves magnitude is much weaker than that of the rectangle injection, which could serve as a plausible mechanism for the lower soot oxidation rate and longer combustion duration. It is interesting to note that this simple 1D model is able to predict the trends of thinner spray tip rich mixture distribution and smaller spray tip penetration in the inversed-delta injection compare to those of the rectangle injection rather accurately.

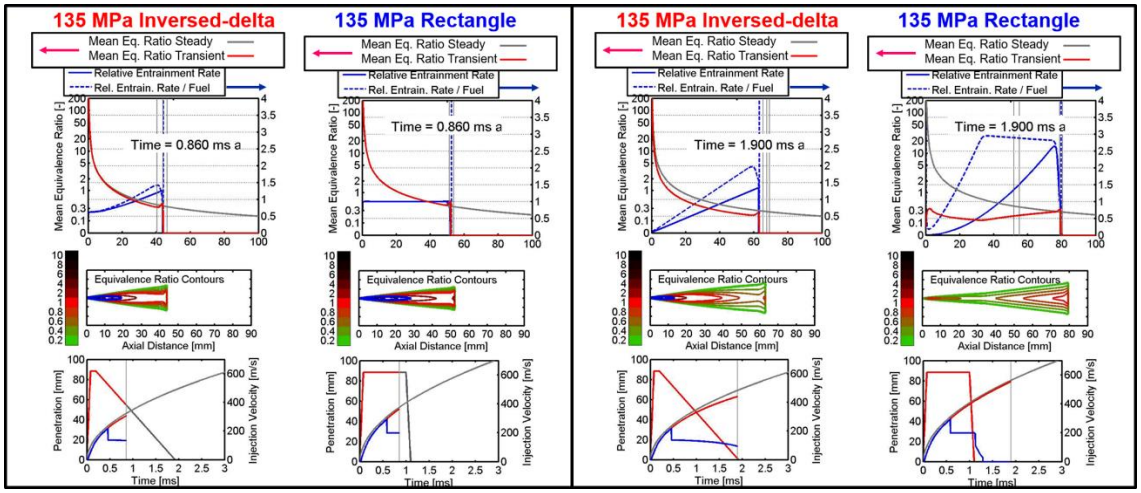


**Figure A1 Comparison of the mean equivalence ratio and air entrainment compare to that of steady jet (top), cross-sectional spray equivalence ratio (middle) as well as injected fuel velocity at the nozzle orifice/injection rate and spray tip penetration (bottom) calculated from one-dimensional simulation for 135 MPa inversed-delta (left) and rectangle injection (right) at 0.86 ms and 1.90 ms timing ASI.**

## Development of Highly Flexible TAIZAC Injector

Thanks to the inner-volume reduction feature through injector body cut-off of the TAIZAC injector, injection pressure could be reduced considerably during injection period. However, its rate shaping flexibility is limited to inversed-delta injection at fixed ramp-down rate. As mentioned in the previous sections, inversed-delta injection rate shaping strategy successfully improve the Diesel engine thermal efficiency, but its impact on combustion duration reduction is somewhat limited as well as slight increase of smoke emissions. Thus, it is necessary to develop a highly flexible injection rate shaping system to achieve the full potential of injection rate shaping approach in improving the thermal efficiency and emissions level.

As continuity to the present TAIZAC injector development, a new type of injection rate shaping device is developed in-house by assembling three production injectors: two of the injectors are directly connected similar to the previous version of TAIZAC injector, and an additional injector is branched between the upper and lower injector, enabling rapid hydraulic pressure spill by a reverse flow into a low-pressure second common rail mechanism. Figure A2 shows the schematic diagram of the discharge-assisted 3-injector TAIZAC injector and variations of injection rate shaping realized at the left and right side, respectively. The cutting-edge DENSO G4P injector (ultra-fast response at microsecond order and can be operated in 270 MPa fuel pressure) is

used as the upper and lower injector, and DENSO 3rd generation solenoid injector G3S operated at 70 MPa is used as the discharge injector. Despite the lower injector body is not being cutted-off, adequate rate of injection rate shaping is successfully achieved by this newly developed TAIZAC injector.

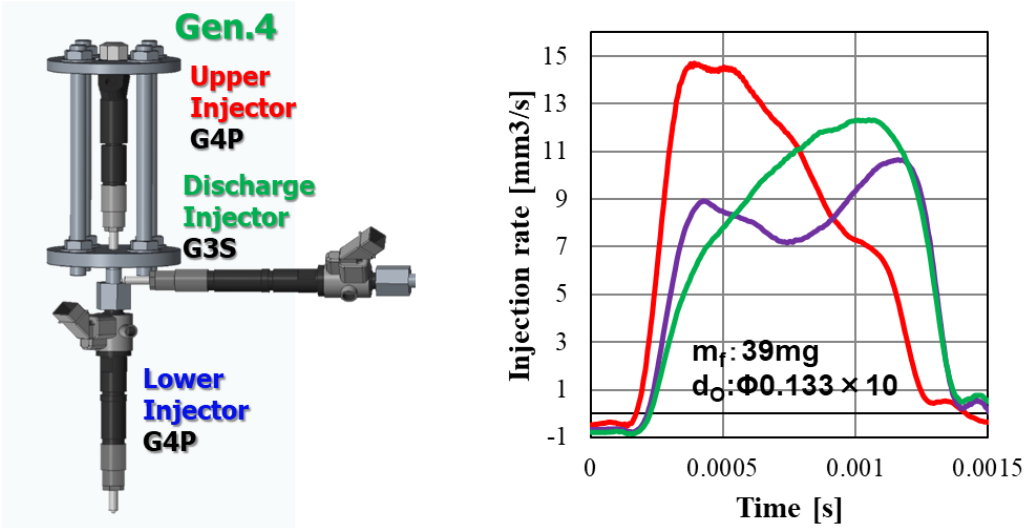


**Figure A2 Schematic diagram of discharge -assisted 3-injector TAIZAC injector (left) and variations of injection rate shaping realized (right).**

Figure A3 shows the engine test results for the inversed-delta and rectangle injection injected with the new TAIZAC injector, where left, middle and right chart indicates the injection pressure/rate, heat balance and degree of constant volume, respectively. Since the lower injector utilize G4P injector, the rectangle injection here can be referred interchange with the G4P injector itself. It is interestingly observed that the inversed-delta injection increases the thermal efficiency by 1.5% even compare to that of G4P injector. The cooling loss is significantly reduced by 2.2%, and surprisingly faster combustion duration is achieved by the inversed-delta injection despite of elongated injection period compare to that of the rectangle injection, suggesting that there are plenty room for improvements for the injection rate shaping approach in achieving higher thermal efficiency.

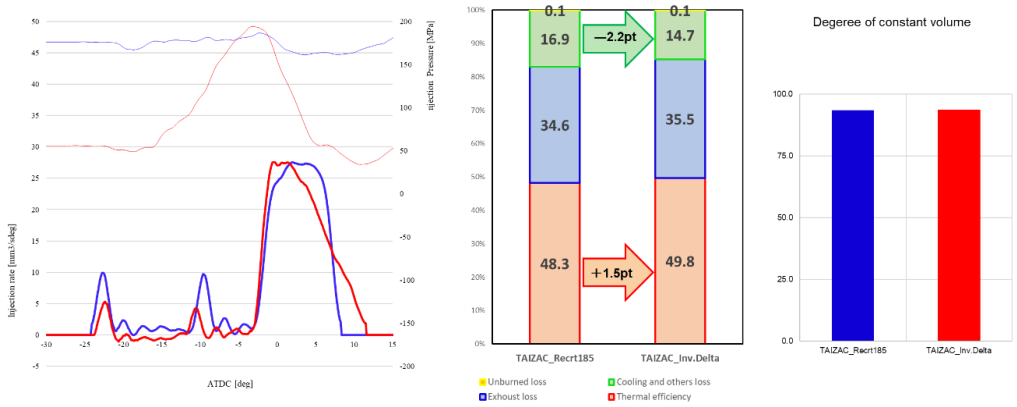


**Figure A3 Injection pressure and rate shaping (left), heat balance (middle) and degree of constant volume (right) of inversed-delta and rectangle injection with discharge-assisted 3-injector TAIZAC injector.**

## Examination of Diesel Spray Flame Structure with Ultra-high Spatial and Temporal Resolution Imaging Diagnostics

Previously, it was assumed that the smaller spray tip penetration in the inversed-delta injection reduced the reacting zone area, thus elongates the combustion duration from simple geometry point of view. However, the unstable fuel supply in the inversed-delta injection is expected to promotes a higher amount of large-scale turbulence that might affects not only the reacting area, but also likely promotes the local heat release rate. The investigation on influences of the inversed-delta injection on its overall spray structure, particularly on the large-scale turbulence is examined with the DBI optical setup shown previously in Figure 33, but with superior ultra-high temporal and spatial resolution state-of-the-art high-speed camera NAC ACS-1, capable to acquire high-speed images at 50,000 fps with 896 x 1280 pixel resolutions. Figure A4 shows the inversed-delta (top row) and rectangle (bottom row) injection rate at the left side and the examples images at 3.54 ms in non-vaporizing conditions at the right side. As observed several times before, the spray tip penetration in the inversed-delta injection is evidently smaller than the rectangle injection one and their near field spray cone angle seems to be similar. However, it is interesting to note that spray width swollen in the inversed-delta injection case particularly from the midstream region (i.e. beyond 50 mm), while the spray width of the rectangle injection appears to be narrower. The inversed-delta injection swollen width is likely caused by insufficient momentum supply of the following spray to push the fuel parcel ahead further, leading to quick spray cone collapse due to large-scale turbulence growth.

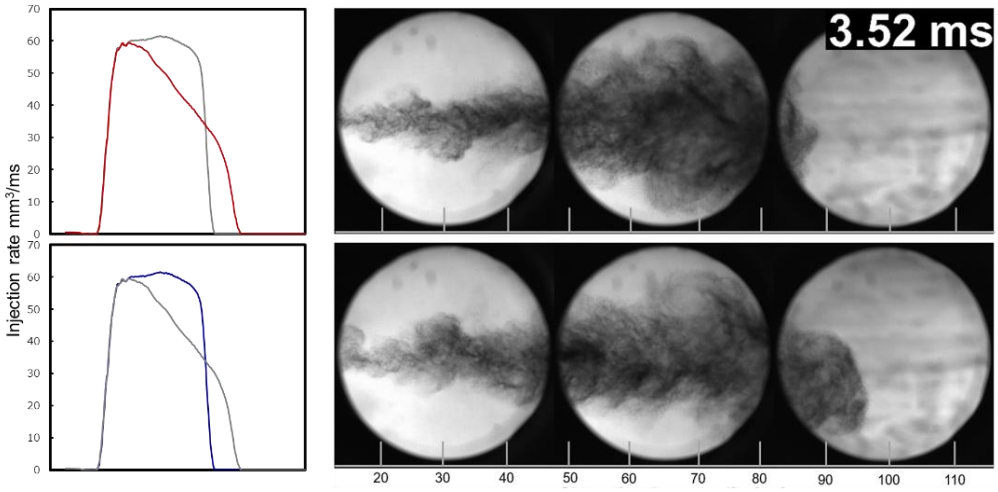


**Figure A4 Example images of non-vaporizing Diesel spray of inversed-delta (top) and rectangle (bottom) acquired at ultra-high speed at 50,000 fps and fine resolution at 896 x 3840 pixel. Ambient conditions: $\rho_g$=23.8 kg/m³, $P_a$=1.6 MPa, $T_a$=373 K and 100% $CO_2$. Injection conditions: φ0.12 mm orifice and $m_f$=5.0 mg.**

To grasps the overall idea regarding this observation, the spray width temporal and spatial distributions is presented in the contour map as shown in Figure A5. The horizontal and vertical axis represents the timing after the start of injection and the axial distance from the nozzle tip, respectively. The false color contour indicates the spray width at a particular time and location. The referral image at 2.50 ms and spray width distributions for the inversed-delta injection and the rectangle injection are displayed at the left and right side, respectively. Note that the spray tip penetration for each injection profile matched-well with the outer layer of the contour map and the map value was ensembled-averaged from 3 injections. It can be observed that the spray width in the inversed-delta injection is larger than that of the rectangle injection as indicates by wider orange-yellowish color at approximately the midstream region, and the spray width seems to keep its shape longer. Meanwhile, the spray width seems to become smaller as soon as the injection event was ended in the rectangle injection, implying that higher large-scale turbulence could be existed in the inversed-delta injection case. Although not displayed here, despite of smaller spray tip penetration, the estimated spray volume for the inversed-delta injection is only slightly smaller by approximately 5% compare to that of the rectangle injection, suggesting the spray average equivalence ratio should be similar. In near future, effects of these large-scale turbulences growth on local heat release rate promotion will be examined from the optical diagnostics approach.

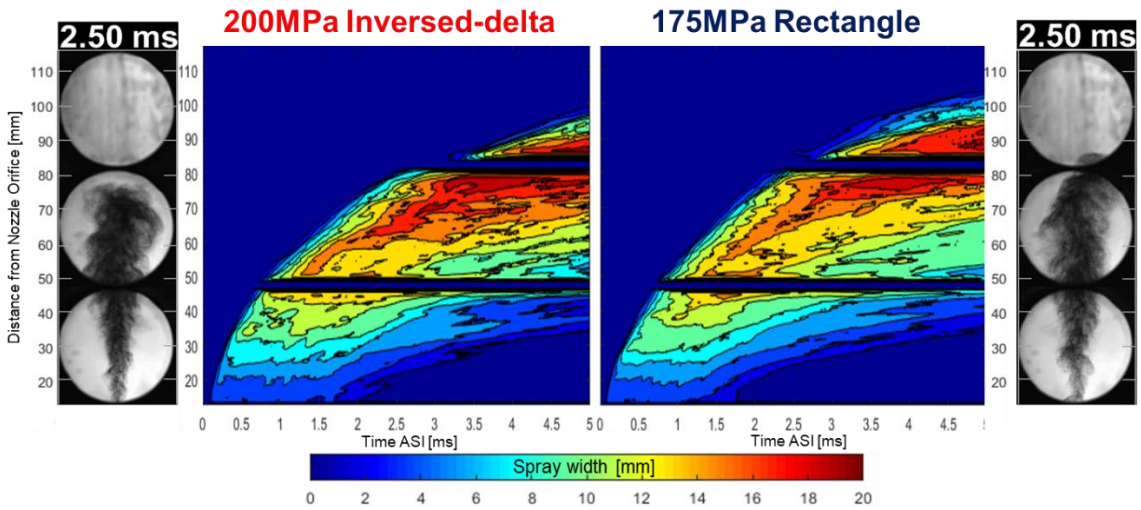


Figure A5 Temporal and spatial spray width distributions (contour map) with spray image example of inversed-delta (left) and rectangle (right) injection. Ambient conditions: $\rho_g$=23.8 kg/m$^3$, $P_a$=1.6 MPa, $T_a$=373 K and 100% $CO_2$. Injection conditions: φ0.12 mm orifice and $m_f$=5.0 mg.